



**JIMMA UNIVERSITY**  
**JIMMA INSTITUTE OF TECHNOLOGY**  
**SCHOOL OF POSTGRADUATE STUDIES**  
**FACULTY OF MATERIALS SCIENCE AND ENGINEERING**  
**CONJUGATED POLYMER-PEROVSKITE NANOCOMPOSITES**  
**FOR OPTOELECTRONICS**

**PH.D. DISSERTATION**

**BY: GETACHEW WELYAB TSONI (PH.D.,CANDIDATE)**

**JUNE, 2024**

**JIMMA, ETHIOPIA**



**JIMMA UNIVERSITY**

**JIMMA INSTITUTE OF TECHNOLOGY  
SCHOOL OF POSTGRADUATE STUDIES**

**FACULTY OF MATERIALS SCIENCE AND ENGINEERING  
CONJUGATED POLYMER-PEROVSKITE NANOCOMPOSITES**

**FOR OPTOELECTRONICS**

**BY: GETACHEW WELYAB TSONI (PH.D.,CANDIDATE)**

**PRINCIPAL ADVISOR: JUNG YONG KIM (PH.D.,PROF.)**

**CO-ADVISOR: MULUALEM ABEBE (PH.D.,ASSOC.PROF.)**

**DHAKSHNAMOORTHY MANI (PH.D., ASST.PROF.)**

**A PH.D. DISSERTATION SUBMITTED TO THE SCHOOL OF  
POSTGRADUATE STUDIES OF JIMMA UNIVERSITY FOR THE  
PARTIAL FULFILLMENT OF THE REQUIREMENTS FOR THE DEGREE  
OF DOCTOR OF PHILOSOPHY (PH.D.) IN MATERIALS SCIENCE AND  
ENGINEERING**

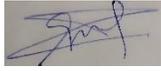
**JUNE, 2024**

**JIMMA, ETHIOPIA**

## DECLARATION

I, the undersigned, declare this Ph. D. dissertation, entitled "**CONJUGATED POLYMER-PEROVSKITE NANOCOMPOSITES FOR OPTOELECTRONICS** " is my own work and has not been submitted for the award of any academic degree or similar qualification at any other institution or university. Furthermore, I confirm that all the sources I have used or quoted have been appropriately indicated and acknowledged.

Name: **Getachew Welyab Tsoni**

Signature: 

Date: 14-06-24

JIMMA UNIVERSITY

SCHOOL OF POSTGRADUATE STUDIES

FACULTY OF MATERIALS SCIENCE AND ENGINEERING

**APPROVAL OF DISSERTATION FOR DEFENSE**

We hereby certify that we have supervised, read, and evaluated this dissertation titled **“CONJUGATED POLYMER-PEROVSKITE NANOCOMPOSITES FOR OPTOELECTRONICS”** by **Getachew Welyab Tsoni**. It was prepared under the supervision of **Jung Yong Kim (Ph.D.,Professor), Muluaem Abebe (Ph.D., Assoc.Prof.) and Dhakshnamoorthy Mani (Ph.D.,Asst.Prof.)**. We recommend submission of the dissertation for the oral defense.

**Prof. JUNG YONG KIM (PHD)**  
Director For Advanced Materials  
Science and Engineering Center  
of Excellence  
Principal Advisor



Signature

14-06-24

Date

Co-Advisor

Signature

Date

Co-Advisor

Signature

Date

Department Head

Signature

Date

JIMMA UNIVERSITY

SCHOOL OF POSTGRADUATE STUDIES

FACULTY OF MATERIALS SCIENCE AND ENGINEERING

**BOARD FOR THE DISSERTATION EXAMINERS' APPROVAL SHEET**

We, the undersigned, members of the Board of Examiners of the Viva Voce/oral defense by **Getachew Welyab Tsoni** have read and evaluated his/her dissertation entitled “**CONJUGATED POLYMER-PEROVSKITE NANOCOMPOSITES FOR OPTOELECTRONICS**” and examined the candidate. This is, therefore, to certify that the doctoral dissertation has been accepted in the fulfilment of the requirement of the doctoral degree in materials science and engineering.

\_\_\_\_\_ 14-06-24

Chair Person

Signature

Date

Prof. Fekadu Gashaw Hone



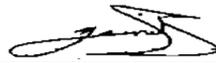
14-06-24

External Examiner

Signature

Date

Nebiyu Gemechu (PhD)



14-06-24

Internal Examiner

Signature

Date

**Prof. JUNG YONG KIM (PHD)**  
Director For Advanced Materials  
Science and Engineering Center  
of Excellence  
Principal Advisor



Signature

14-06-24

Date

## **Acknowledgements**

Without the assistance and support of the people I was fortunate enough to have along for the PhD trip, the results reported in this dissertation would not have been achievable. First, I want to thank my advisor, Prof. Dr., Jung Young Kim, for his guidance and generous support over these years. I am greatly inspired by his enthusiasm, knowledge, and thoughts regarding innovation and research. I am grateful for your assistance in finishing this dissertation.

Next, I would like to thank Dr. Muluaem Abebe, for giving up your time to mentor, supply materials and overall offer good opportunity to handle my works. I would also want to thank Dhakshnamoorthy Mani, for his advice and offer the chance to carry out laboratory work. On the other hands , I would like to thank Maji Werda, and West Omo zone adminstartions and Mizan Tepi university for their supports to conduct my PhD. project. Moroever , I would like to thank lab technical at school chemical and energy materials (Mahatma Gandhi university,India) for their supports and collaborations. In additional to that I would like to thank, shool of materials science and engineering staffs for their help through charactetrizations and any other concerns.

Further, I would like to convey my appreciation to our amazing group members both past and current. I feel extremely fortunate to have your help and advices. Specially, I want to thank my friend Dula Adugna for encourage and motivate me to handle my works. Finally,I would like to thank all my families for their every support, love, and understanding. Thank you!

## List of Abbreviations

ABX<sub>3</sub>-General chemical structure of perovskite materials, where A and B are cations and X is halide anions

ASE-Amplification simulation emission

Br-Bromine

Cl-Chlorine

Cs-Cesium

CsPbBr<sub>3</sub>-Cesium Lead Bromide

CsPbCl<sub>3</sub>-Cesium Lead Chloride

CsPbI<sub>3</sub>-Cesium Lead Iodide

DNCs-Double layer nanocrystals

DMF- *N,N*-dimethylformamide

ETL-Electron transporting layer

EML-Emissive layer

EQE-External quantum efficiency

FAPbBr-Formamidinium lead bromide

FE-SEM- Field emission scanning electron microscopy

FRET-Förster resonance energy transfer

FET- Field effect transistor

FTIR-Fourier transform infrared spectroscopy

FWHM-Full width of half maximum

F8BT- Poly(9,9-dioctylfluorene-*alt*-benzothiadiazole)

GCE-Glassy carbon electrode

HI- Hot injection

HRTEM- High resolution transmission electron microscopy

I-Iodine

LED –Light-Emitting Diode

LHP-Lead Halide Perovskite

MAPbBr-Methylammonium Lead Bromide

MEH-PPV-Poly[2-methoxy5-(2'-ethyl-hexyloxy)-1-4-phenylene vinylene

MDMO-PPV-Poly[2-methoxy-5-(3',7'-dimethyloctyloxy)-1-4-phenylenevinylene]

MHP-Metal halide perovskite

NCs –Nanocrystals

NWs- Nanowires

OA-Oleic acid

OAm -Oleylamine

OLED-Organic light emitting diode

OHP-Organometal halide perovskite

OO-Olive oil

OSTE -off-stoichiometry thiol-ene

Pb-Lead

PCE-Power conversion efficiency

PEG- Polyethylene glycol

PeLED-Perovskite light emitting diode

PEO-polyethylene oxide

PDMS- Polydimethylsiloxane

PFO-Poly (9,9-dioctylfluorene)

PLEDs-Polymer light emitting diodes

PLQY-Photoluminescence quantum yield

PMMA-Polymethylmethacrylate

PMMA-Polymethylmethacrylate

PVDF- polyvinylidene difluoride

PVP-Polyvinyl Pyrrolidone

PS-Polystyrene

QDs-Quantum dots

QLEDs-Quantum dot light emitting diode

RT-Room Temperature

SEM-Scanning electron microscopy

SR-Supersaturated recrystallization

TCSPC- Time Correlated Single Photon Counting

XRD - X-ray diffraction

XPS-X-ray photoelectron spectroscopy

2D-Two dimension

3D-Three dimension

## Table of Contents

Acknowledgements.....	i
List of Abbreviations .....	ii
Table of Contents.....	v
List of Figures .....	viii
List of Tables .....	xii
Executive Summary.....	xiii
Chapter One .....	1
1. Introduction .....	1
1.1. Background.....	1
1.2. Statement of the Problems .....	9
1.3 . General Objective .....	10
1.3.1. The Specific Objectives.....	10
1.4. Significance of the Study.....	10
1.5. Research Questions.....	10
1.6. The Conceptual Frameworks .....	11
1.7. Dissertation Organization .....	12
Chapter Two.....	13
2. Review Literatures .....	13
2.1. Overview.....	13
2.2. Effects of Ligands on All-inorganic Cesium Lead Halide Perovskite NCs.....	16
2.3. Flory-Huggins Theory .....	16
2.4. Polymer-Perovskite Based Composites .....	17
Chapter Three.....	23
3. Materials and Methods .....	23
3.1. Materials .....	23
3.2. Synthesis Methods .....	23

3.2.1. Hot-Injection Method .....	24
3.2.2. Ligand-assisted Reprecipitation Method .....	24
3.3. Characterization Techniques.....	24
3.3.1. X-Ray Diffraction.....	24
3.3.2. Scanning Electron Microscope .....	25
3.3.3. High Resolution Transmission Electron Microscope .....	25
3.3.4. Ultra Violet Visible Spectroscopy .....	26
3.3.5. Photoluminescence Spectroscopy.....	26
3.3.6. Time Correlated Single Photon Counting .....	26
3.3.7. Fourier Transform Infrared Spectroscopy .....	27
3.3.8. Contact Angle Measurement .....	27
3.3.9. Electrochemical Impedance Spectroscopy .....	27
Chapter Four .....	28
4. All-Inorganic CsPbBr <sub>3</sub> Perovskite Nanocrystals Synthesized with Olive Oil and Oleylamine at Room Temperature.....	28
4.1. Introduction.....	28
4.2. Materials and Methods.....	30
4.2.1. Chemicals .....	30
4.2.2. Synthesis of CsPbBr <sub>3</sub> Nanocrystals.....	30
4.2.3. Characterization.....	31
4.2.4. Computational Methods .....	32
4.3. Results and Discussion .....	32
4. 4. Conclusions.....	43
Chapter Five.....	45
5. Conjugated Polymer–Perovskite Quantum Dot (MDMO-PPV:CsPbBr <sub>3</sub> ) Nanocomposites: Miscibility, Nano-Structures and Properties .....	45
5.1. Introduction.....	45
5.2. Materials and Methods.....	47

5.2.1. Chemicals .....	47
5.2.2. Synthesis of CsPbBr <sub>3</sub> Quantum Dots .....	48
5.2.3. Preparation of MDMO-PPV–CsPbBr <sub>3</sub> QD Composites .....	48
5.2.4. Characterizations .....	48
5.3. Results and Discussion .....	49
5.4. Conclusions.....	67
Chapter Six.....	69
6. Facile Synthesis and Characterization of Polymer-Mixed Halide Perovskite Composites.....	69
6.1. Introduction.....	69
6.2. Materials and Methods.....	71
6.2.1. Chemicals .....	71
6.2.2. Synthesis of CsPb(Br <sub>1-x</sub> Cl <sub>x</sub> ) <sub>3</sub> (X= 0.33, 0.50).....	71
6.2.3. Preparation of MDMO-PPV :CsPb(Br <sub>1-x</sub> Cl <sub>x</sub> ) <sub>3</sub> (X= 0.33, 0.50) Composites .....	71
6.2.4. Characterizations .....	72
6.3. Results and Discussion .....	72
6.4. Conclusions.....	76
Chapter Seven .....	77
7. Summary and Recommendations .....	77
7.1. Summary.....	77
7.2. Recommendations.....	78
References.....	79
Appendix.....	108

## List of Figures

<b>Figure 1.1</b> Typical ABX <sub>3</sub> perovskite crystal structure .....	4
<b>Figure 1.2</b> (A) Defect tolerance in LHP NCs.(B) The diagram comparing electronic structures that are defect-intolerance (conventional semiconductors) and defect tolerance for perovskite.....	5
<b>Figure 1.3.</b> Band gap energy level diagram.....	6
<b>Figure 1.4.</b> Chemical Structure of Polymers (A) PPV B) MEH-PPV C) MDMO-PPV D) m PFO E) PFOpen F) PF G) F8BT H) P3HT I) PVK J)PMMA K) PVP.....	8
<b>Figure 1.5.</b> Conceptual Frame works .....	11
<b>Figure 2.1.</b> Map of ( $t, \mu$ ) for 138 perovskite compounds considered in our work. Red dots mean $\Delta HD > 0$ (predicted to be stable), and black dots mean $\Delta HD < 0$ (predicted to be unstable).....	14
<b>Figure 2.2.</b> The CsPbX <sub>3</sub> (X = Cl, Br, I) NCs have narrow FWHM and bright emission, with composition-tunable bandgap energies covering the whole visible spectral region.....	15
<b>Figure 2.3.</b> Energy diagram of CsPbBr <sub>x</sub> Cl <sub>3-x</sub> /MEH-PPV.....	19
<b>Figure 4.1.</b> Polyhedral of CsPbBr <sub>3</sub> unit cell: (a) orthorhombic,(b) tetragonal, and (c)cubic structure .....	32
<b>Figure 4.2.</b> The electronic structures of CsPbBr <sub>3</sub> unit cells displaying polymorphism: (a) Orthorhombic, (b) tetragonal, and (c) cubic phase. Here, the bandgap energy ( $E_g$ ) of each <i>unit cell</i> is 2.31eV for orthorhombic, 2.37 eV for tetragonal, and 2.40 eV for cubic phase, respectively.....	33
<b>Figure 4.3.</b> Chemical structures of (a) olive oil: glycerol fractions, ~98%, (b) oleylamine, and (c) DMF and toluene.....	34
<b>Figure 4.4.</b> (a) The free energy change ( $\Delta G$ ) in the nucleation and growth process as a function of $r$ (a radius of a spherical nucleus by assumption). Here, $\Delta G^*$ is the critical free	

energy barrier at the critical radius ( $r^*$ ), where a unit cell is formed. (b) Schematic explanation of supersaturated recrystallization (SR) of CsPbBr<sub>3</sub> in the antisolvent toluene.....36

**Figure 4.5.** Vials containing a CsPbBr<sub>3</sub> colloidal dispersion depending on surface ligands: (a) oleic acid and oleylamine – a normal photo, (c) oleic acid and oleylamine – under 365 nm UV light, (c) olive oil and oleylamine – a normal photo, and (d) olive oil and oleylamine – under 365 nm UV light. Hence, CsPbBr<sub>3</sub> nanocrystals can serve as a green-light emitter.....37

**Figure 4.6.** XRD patterns of CsPbBr<sub>3</sub> nanocrystal drop-cast thin film depending on the ligand species: (a) oleic acid and oleylamine and (b) olive oil and oleylamine. (c) Joint Committee on Powder Diffraction Standards (JCPDS) (PDF#96-153-0682) and (d) JCPDS (PDF#96-153-3063).....39

**Figure 4.7.** HR-TEM images of CsPbBr<sub>3</sub> nanocrystals (nano cubic) when the ligand was oleic acid & oleylamine (a and b) and olive oil & oleylamine (c and d).....40

**Figure 4.8.** (a) UV-Vis absorbance spectra of the CsPbBr<sub>3</sub> nanocrystal dispersion depending on the ligand species. Here,  $\lambda = 530$  nm corresponds to  $E_g \approx 2.34$  eV (oleic acid & oleylamine) and  $\lambda = 533$  nm corresponds to  $E_g \approx 2.33$  eV (olive oil & oleylamine). (b) PL spectra of CsPbBr<sub>3</sub> nanocrystal depending on the ligand species. (c) optical bandgap of CsPbBr<sub>3</sub> nanocrystals by Tauc plot depending on the ligand species .....42

**Figure 4.9.** (a) PL spectra decay of CsPbBr<sub>3</sub> nanocrystals depending on the ligand species. (b) FT-IR spectra of CsPbBr<sub>3</sub> nanocrystals depending on the ligand species.....43

**Figure 5.1.** Structures of organic molecules and inorganic crystal: (a) MDMO-PPV; (b) 3×3×3 Supercell of CsPbBr<sub>3</sub>; (c) oleic acid and oleylamine; and (d) toluene.....50

**Figure 5.2.** Water contact angle measurement on the spin-coated MDMO-PPV film. Here, the force balance among surface energies could be explained by Young’s equation,  
 $\gamma_{lv} \cos \theta_c = \gamma_{sv} - \gamma_{sl}$  .....51

**Figure 5.3.** (a) Phase diagrams of the binary MDMO-PPV–toluene system as a function of molecular weight of MDMO-PPV. (b) The plot of the critical temperature vs. the number average molecular weight of MDMO-PPV. (c) Phase diagrams of the binary MDMO-PPV–oleic acid (black solid line) and MDMO-PPV–oleylamine (red solid line) system. (d) Phase diagrams of the binary oleic acid–toluene (black solid line) and oleylamine-toluene (red solid line) systems.....56

**Figure 5.4.** XRD patterns of drop-cast films on the glass substrate: (a) MDMO-PPV; (b) CsPbBr<sub>3</sub> QD nanocrystals; (c) MDMO-PPV: CsPbBr<sub>3</sub> = 90:10; (d) MDMO-PPV: CsPbBr<sub>3</sub> = 80:20; (e) MDMO-PPV: CsPbBr<sub>3</sub> = 70:30; and (f) MDMO-PPV: CsPbBr<sub>3</sub> = 60:40, and MDMO-PPV:CsPbBr<sub>3</sub> = 50:50.....58

**Figure 5.5.** XRD patterns of drop-cast films as a function of time: (a) MDMO-PPV: CsPbBr<sub>3</sub> = 0:50; (b) CsPbBr<sub>3</sub> QD nanocrystals; and (c) amorphous MDMO-PPV. Here, ‘0 hr’ indicates the *as-prepared* sample.....60

**Figure 5.6.** TEM image of the drop cast CsPbBr<sub>3</sub> nanocrystals on the copper grid: (a) scale bar = 50 nm, (b) scale bar = 20 nm and (c) scale bar = 5 nm. (d) SAED patterns of the drop cast CsPbBr<sub>3</sub> nanocrystals.....61

**Figure 5.7.** SEM images of the drop-cast films: (a) MDMO-PPV; (b) MDMO-PPV:CsPbBr<sub>3</sub>= 80:20; and (c) MDMO-PPV:CsPbBr<sub>3</sub>= 50:50.....62

**Figure 5.8.** FT-IR spectra at ATR mode: (a) MDMO-PPV; (b) CsPbBr<sub>3</sub> nanocrystals; (c) MDMO-PPV:CsPbBr<sub>3</sub>= 80:20; and (d) MDMO-PPV:CsPbBr<sub>3</sub>= 50:50.....63

**Figure 5.9.** Absorption and emission spectra of the spin-coated films.....65

**Figure 5.10.** (a) Schematic energy diagram and (b) PL emission through the FRET between CsPbBr<sub>3</sub> and MDMO-PPV.....66

<b>Figure 5.11.</b> Electrochemical impedance spectroscopy (EIS) data of the pure MDMO-PPV and MDMO-PPV: CsPbBr <sub>3</sub> = 50:50 wt.% composition.....	67
<b>Figure 6.1.</b> X-ray diffraction patterns for CsPb ( Br <sub>1-x</sub> Cl <sub>x</sub> ) <sub>3</sub> /MDMO-PPV composites as well as its pure component (i.e., polymer and perovskite). Note that MDMO-PPV is an amorphous polymer displaying an amorphous halo at $2\theta \approx 25^\circ$ (see the black solid line).....	73
<b>Figure 6.2.</b> UV-Vis absorption spectra the CsPb ( Br <sub>1-x</sub> Cl <sub>x</sub> ) <sub>3</sub> /MDMO-PPV composites as well as its pure component (polymer and perovskite).....	73
<b>Figure 6.3.</b> Determination of optical bandgap of samples $(ah\nu)^2$ vs. Energy.....	74
<b>Figure 6.4.</b> PL spectra of CsPb(Br <sub>1-x</sub> Cl <sub>x</sub> ) <sub>3</sub> /MDMO-PPV composites as well as its pure component (polymer and perovskite).....	75
<b>Figure 6.5.</b> FTIR spectra of CsPb(Br <sub>1-x</sub> Cl <sub>x</sub> ) <sub>3</sub> /MDMO-PPV composites as well as its pure component (polymer and perovskite).....	75

## List of Tables

<b>Table 4.1.</b> Gutmann’s solvent donor number ( $D_N$ ), solubility parameter ( $\delta$ ), dielectric constant( $\epsilon$ ), molar mass, density, boiling point (b.p.) and chemical structures of solvents.....	37
<b>Table 4.2.</b> Crystallite size ( $t$ ) of CsPbBr <sub>3</sub> at the (200) crystallographic plane. Here, $\beta$ denotes a full width at half maximum (FWHM).....	39
<b>Table 5.1.</b> Solubility parameter of solvent, polymer, and ligands (oleic acid and oleylamine).....	53
<b>Table 5.2.</b> Solubility-parameter component group contributions (Hoftyzer-Van Krevelen method for oleic acid and oleylamine.....	53
<b>Table 5.3.</b> Flory-Huggins interaction parameter for the binary system. Here, the components 1, 2, 3, and 4 correspond to toluene, MDMO-PPV ( $M_n = 10,000 \text{ g}\cdot\text{mol}^{-1}$ ), oleic acid, and oleylamine, respectively.....	54
<b>Table 5.4.</b> Crystallite size ( $t$ ) of CsPbBr <sub>3</sub> nanocrystals at the (200) crystallographic plane as a function of the composition of the MDMO-PPV:CsPbBr <sub>3</sub> composites. Here, MDMO-PPV has $M_n$ of $120,000 \text{ g}\cdot\text{mol}^{-1}$ .....	59
<b>Table 6.1.</b> Crystallite size ( $D$ ) of CsPb(Br <sub>1-x</sub> Cl <sub>x</sub> ) <sub>3</sub> and its composite. Here, $\beta$ denotes a full width at half maximum (FWHM) at angle $\theta$ .....	72

## Executive Summary

Metal halide perovskite semiconductors are a new material class that has shown great promise for a range of optoelectronic device applications. Due to their emission wavelength tunability throughout the visible spectrum and EQE of over 20%, they have shown to be very promising materials for light-emitting diodes. Nevertheless, further work must be done to enhance their properties for practical uses. Several approaches, including as ligand modification and polymer mixing, are developed to address these problems and demonstrate improvements in the characteristics and performance of devices. Thus, conjugated polymer-perovskite  $\text{CsPbX}_3$  (x=halide, their combinations) nanocrystal (NCs) composites is the main focus of our work. The synthesis of perovskite NCs was carried out at room temperature utilizing a type of ligand assisted reprecipitation method called supersaturation recrystallization. Then, a solution mix approach was then used to prepare the composites of conjugated polymer with perovskite nanocrystals. Initially, we look into how ligands affect the characteristics of all-inorganic halide perovskite  $\text{CsPbBr}_3$  that is produced by supersaturated recrystallization (SR) methods at room temperature. Here, the structural and optical characteristics of  $\text{CsPbBr}_3$  produced using ligand systems (oleic acid/oleylamine versus olive oil/oleylamine) were investigated. In this case, the optical band gap value is 2.3 eV and cube-shaped nanocrystal with crystallite size of 40-42 nm achieved during the utilization of two ligand species combinations. In contrast, a longer decay life time, i.e., 3.228 ns was seen in the ligand combination of olive oil and oleylamine as compared to oleic acid and oleylamine which is 1.167 ns. Secondly, separate preparations were made for the conjugated polymer and the  $\text{CsPbBr}_3$  solution. Subsequently, two precursor solutions were combined utilizing a solution blend approach, which included varying sample ratios and was characterized by a number of techniques. Nanostructure and characteristics in the conjugated polymer-perovskite nanocomposite were investigated. Using Flory Huggins' theory, the miscibility of polymers with solvents, ligands, and perovskites was predicted. As the amount of perovskite  $\text{CsPbBr}_3$  NCs in the MDMO-PPV polymer matrix increases, it is evident in the crystallite size shift, which ranges ~33 to 52 nm. According to scanning electron microscope images display that  $\text{CsPbBr}_3$  QDs can be highly aggregated at MDMO-PPV: $\text{CsPbBr}_3$  = 50:50 composition. Additionally, there is an improvement in emission PL, with more than or equivalent to 30 Wt% of  $\text{CsPbBr}_3$  NCs observed. Furthermore, it was

observed that the conjugated polymer and perovskite nanocrystal overlapped in terms of both PL emission donor CsPbBr<sub>3</sub> and acceptor MDMO-PPV absorption, indicating a potential energy transfer between the two materials. Here, the charge transfer-resistance is decreased in the 50:50 of MDMO-PPV/CsPbBr<sub>3</sub> composite, showing that the composite has better charge transport properties than the pristine MDMO-PPV.

Finally, simple synthesized of mixed halide perovskite was conducted by SR methods at room temperature. Then, mixed halide perovskite was doped into conjugated polymer was carried out. The composite of CsPb(Br<sub>1-x</sub>Cl<sub>x</sub>)<sub>3</sub> doped into MDMO-PPV shows an improvement in crystallite size as the concentration of mixed halide perovskite increases with chlorine content rise compared to pristine polymer. Similarly, the PL emission shows enhancement as content of chlorine rise in the composites. In conclusion, our research indicates that the pure perovskite CsPbBr<sub>3</sub> generated utilizing the recommended ligand combination and the polymer-perovskite nanocomposite exhibits improved properties. Therefore, the finding was suggested that in the future this technique holds promising for use electrochemical and optoelectronic applications.

**Keywords:** Perovskite nanocrystal; Conjugated Polymer; Ligands; supersaturated-Recrystallization; Nano-composites; optoelectronic devices

# Chapter One

## 1. Introduction

### 1.1. Background

Solid-state photonic devices, such as lasers and light-emitting diodes (LEDs), are essential to modern display and lighting technology. In addition to common lighting and display applications, they may address urgent problems including energy conservation and greenhouse gas emissions[1]. The world population is growing at a rapid rate, which raises the demand for electrical energy and causes a drop of nonrenewable energy sources, such as fossil fuels. Furthermore, using fossil fuels as a source of energy pollutes the environment, harming both human health and the ecosystems. In order to produce optoelectronic devices with affordable materials and improved performance, researchers therefore conducted extensive study to replace those energy sources with sustainable and appropriate for environment and humans[2]. Here, the light source plays a key role in human daily activities, which are indispensable with lighting development technology that began since utilization fire. Nowadays, with this reasons researchers concentrated on the development suitable light source for light and display technology in order to meet the desire customers over the world [3]. More than 50 years have passed since the first visible spectrum LED demonstration using gallium arsenide phosphide[4]. There are now several light-emitting materials have been demonstrated through the advancement of materials science. This has led to the evolution of numerous LEDs such as Inorganic semiconductor LEDs, Organic LEDs (OLEDs), Polymer LEDs (PLEDs), Quantum-dot LEDs (QLEDs), and more recently Perovskite LEDs (PeLEDs)[2,5]. Since LED explore its potential for the creation of modern display and lighting technology.

At the moment, LEDs made of traditional semiconductor materials, such as OLEDs and QLEDs are gradually becoming commercially available while also facing certain challenges[6]. Even though OLEDs has exceptional advantages such as low power consumption, fast response, affordable costs, suitability for the solution process, flexibility for large-scale production and their outstanding compatibility with flexible substrates due to that it entered to the conventional display and lighting market [7–11]. OLED displays used

vacuum-based thermal evaporation for fabrication which renders them inappropriate cost-effective large-area processing, and their wider full width at half maximum (FWHMs, > 50 nm) also restrict the attainable color gamut [6]. In the majority of PLEDs, electron injection is more challenging than hole injection due to the high energy barrier and low electron mobility in conjugated polymers. Moreover, cumbersome preparation, low performance and lifetime makes them commercially not viable as matured Si-based devices [12]. In the field of PLEDs, these are the main obstacles [13,14].

As an alternative, QLED displays based on II-VI and III-V group QDs have been developed, providing better color purity, narrow emission line width, high photoluminescence quantum yield (PLQY), superior photo stability, and easier solution-processed for device manufacturing [15,16]. Compared to CdSe QDs, Cd-free III-V QDs such as InP, exhibits lower quantum efficiency and wider emission line widths, and face difficulties with high-temperature synthesis that is complex and costly raw precursor materials. However, CdSe-based QDs, which represent the heavy element (Cd) in the II-VI QDs system, are unable to obey the European Restriction of Hazardous Substances regulation [6,17,18]. Besides, QDs exhibits color purity  $\approx 120\%$  and FWHM (25–40 nm), and high stability so CdSe-based quasi two-dimensional II-VI colloidal nanoplatelets, also known as quantum wells, are very promising for Rec. 2020 displays. However, their limited surface defect tolerance and poor quantum efficiency stability have made it difficult for them to be used in practical LED applications, and achieving high efficiency and high luminance at the same time remains a challenge [6,18,19].

In the past decade, the emerging class of metal halide perovskite semiconducting materials are highly progressing in their development as compared to traditional materials owing outstanding optical and electrical properties [20–25]. The perovskite material has general chemical formula written as  $ABX_3$ , where A and B are cations and X is halides. Here, A represents a monovalent cation [methylammonium ( $MA^+$ ), formamidinium ( $FA^+$ ), or cesium ( $Cs^+$ ), Rubidium,  $Rb^+$ ], where as B indicates a divalent metal cation (Lead,  $Pb^{2+}$ , Tin,  $Sn^{2+}$ ), and X represents a halogen anion [chlorine ion ( $Cl^-$ ), bromine ion ( $Br^-$ ), iodine ion ( $I^-$ )] or mixed (Br/Cl) [26] as shown in Figure 1.1.

Their unique optoelectronic properties that makes them a promising candidate for optoelectronic applications such as solar cells, light-emitting diodes, lasers, and photo detectors. Because of these significant scientific community has focused more on all-inorganic perovskite materials than organic-inorganic perovskite. They differ from metal chalcogenides and QDs due to their narrow FWHM, high color purity, tunable band gap, high light absorption efficiency, low carrier recombination rate, high defect tolerance, high PLQY, and high synthetic feasibility. These characteristics make the fault-tolerant structure desirable for usage in a range of optoelectronic applications [27,28].

Furthermore, due to improved chemical and thermal stability as well as their optical properties makes researchers showing more interest based on all-inorganic perovskite semiconducting materials. Because of these benefits, optoelectronics, electronics, and photonic technologies have seen fast improvement [25,28]. There are different forms of CsPbX<sub>3</sub> perovskite, including two-dimensional nanoplates, one-dimensional nanowires (NWs), and zero-dimensional quantum dots, have been prepared with adjustable composition and shape [27]. The Hot-injection (HI)[29] and ligand-assisted re-precipitation (LARP) [30] are two common methods used to produce perovskite nanocrystals (NCs). However, there are several unavoidable disadvantages to the hot-injection approach, including longer reagent mixing times, practicality issues with reaction control times, and reproductive difficulties. These factors limit the synthesis of NCs. Comparatively speaking, the LARP approach is straightforward, inexpensive, and has accurate reaction temperature and duration as well as a high production yield of stable PeNC at RT; nevertheless, HI requires high temperatures, inert gases, and chemical instability throughout the synthesis process[25,28,31]. The reaction precursors are usually dissolved using a good solvent in the LARP method. The precursors then become oversaturated and precipitate as perovskite nanocrystals upon mixing with a poor solvent[32].

Organic carboxylic acids and amines are common surfactants utilized in the synthesis of traditional colloidal quantum dots. These substances can efficiently solvate the inorganic precursors, alter the kinetic pathways to form anisotropically grown nanostructures, and stabilize the final colloidal nanostructure. The acid-base ligand system is critical to the majority of the synthetic procedures used to create all-inorganic perovskite NC. Under these

circumstances, the mix of ligands are use to adjust the shape and change crystal phase of CsPbX<sub>3</sub> NCs may also be controlled, which increases their stability[33].

On other hand, replacement of Pb<sup>2+</sup> by metal ions such Cu<sup>+</sup>,Ag<sup>+</sup>,Ge<sup>+</sup>,Sn<sup>2+</sup>,Bi<sup>3+</sup>,In<sup>3+</sup>,and Sb<sup>3+</sup> makes that optoelectronic properties optimized. However, lead free materials exhibit low performance as compared to lead based perovskite materials. Besides that, the poor stability of perovskite are still challenging[34].

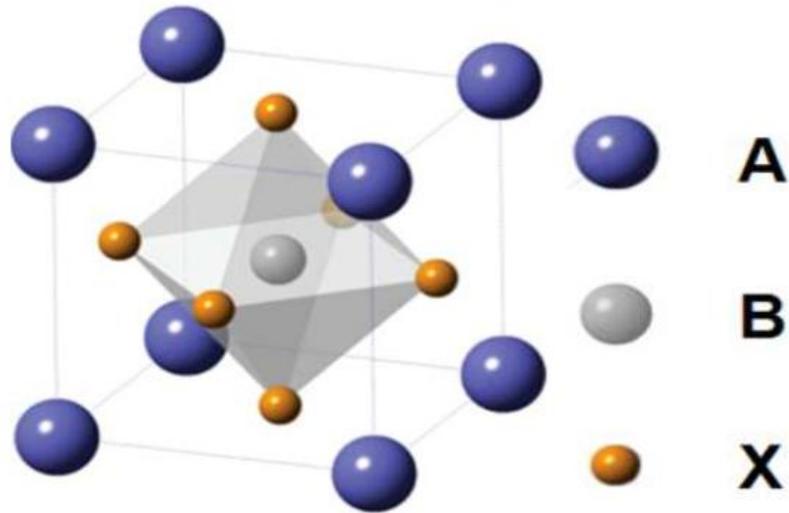


Figure 1.1. Typical ABX<sub>3</sub> perovskite crystal structure [25].

The Goldschmidt tolerance factor (t-factor) and octahedral factor ( $\mu$ ) can be used to predict the stability of the perovskite ABX<sub>3</sub> crystal structure [35]. The effect of the defects on the electronic structure of conventional semiconductors and lead halide perovskite nanocrystal (LHPNCs) makes them to form trap states as a result of band gap formations, as shown in Figure 1.2 , which reduces the radiative recombination of the active materials[18].

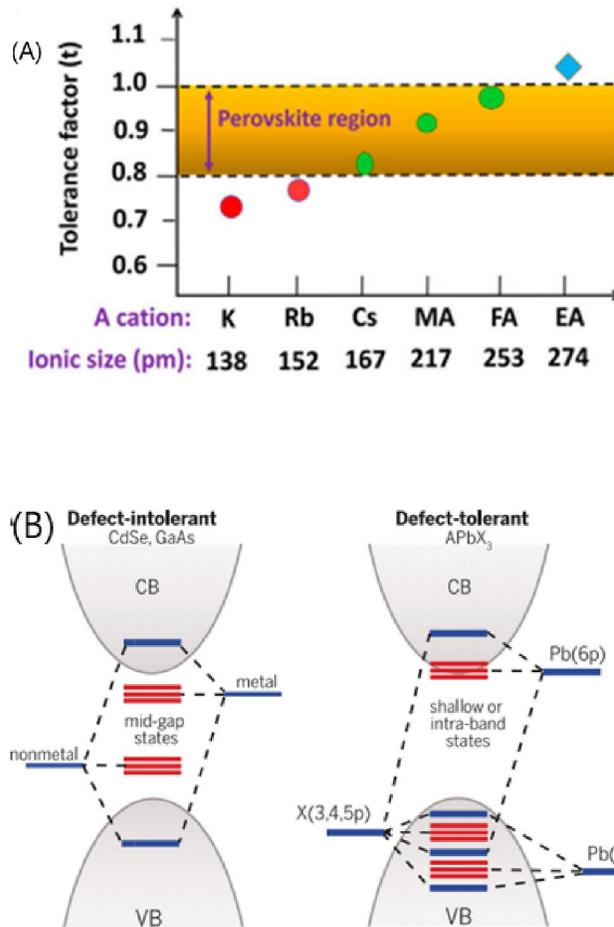


Figure 1.2. (A) Defect tolerance in LHP NCs[5]. (B) The diagram comparing electronic structures that are defect-intolerant (conventional semiconductors) and defect tolerance for perovskite[18].

Even while organic-inorganic perovskite  $\text{CH}_3\text{NH}_3\text{PbI}_3$  ( $\text{MAPbI}_3$ ) and  $\text{CH}_3\text{NH}_3\text{PbBr}_3$  ( $\text{MAPbBr}_3$ ) were used as photosensitizing materials in dye-sensitized solar cells for the first time. The research community was not familiar with  $\text{CsPbX}_3$  NCs until 2009. Since 2012 evolution breakthrough, materials have been employed as sensitizing materials in dye-sensitized solar cells due to their intriguing charge carrying properties[36,37]. But there is stability issue with organic-inorganic hybrid perovskite which limits its applications[38]. The superior thermal and chemical stability, excellent morphology control during synthesis, high monodispersity, and crystallinity of all inorganic perovskite  $\text{CsPbX}_3$ NCs over organic-inorganic hybrid attracted the attention of optoelectronic device researchers [39]. A new generation of intriguing candidates for high-quality lighting and displays has emerged

recently with the successful synthesis and study of all-inorganic perovskite nanocrystals for diverse color emissions. This is because of their emission spectrum and finely-tunable light emitting properties[39–41].

As it is known that all-inorganic perovskite QD-based light-emitting devices has limitations in terms of brightness, stability, and performances and required improvements[42]. Furthermore, Perovskite material's stability problems are serious concerns when exposed to moisture, oxygen, thermal stress, and light[43]. Furthermore, the low solubility of all inorganic perovskite materials poses significant challenges for their development, resulting in low film quality and poor interfacial electrical properties[37]. Consequently, the stability and properties of the perovskite QDs based active layer of optoelectronic devices can be improved by using one of the two approaches : conduct a surface modification on perovskite or prepare a perovskite/polymer composite [44]. In this scenario, organic conjugated materials including polymers and oligomers are gaining a lot of attention as promising materials with special photo physical properties to robust optical and optoelectronic device materials such as perovskite quantum dots (PQDs)[45].

In general , the performance of the device which was determined by its components. Thus, device engineering is very essential for the improvement of perovskite properties and enhancement of device performance[46]. Therefore, the energy level diagram is shown in Figure 1.3.

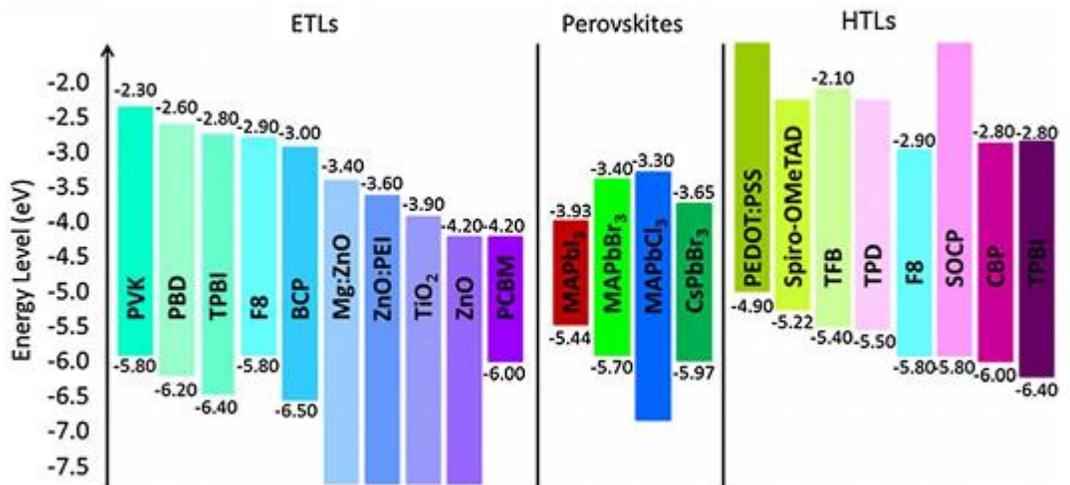


Figure 1.3. Band gap energy level diagram[47–49].

Furthermore, the strategy that makes to achieve good performance at each device interface through energy level alignment is the one that offers superior charge injection and a strong barrier against the opposing charge carrier[50,51].

Therefore, in order to stabilize and improve the properties , polymers as well as silica are best promising candidates [33]. The development of nanocomposites based on polymers and inorganic semiconductor materials including perovskite materials makes improvements in the properties and performance of devices as compared to pristine[12,52–58].

Thus, chemical structure of various polymer as demonstrated as presented in the Figure 1.4, which used for making composites to improve the properties inorganic quantum dots and perovskite materials. Polymers such polymer as polymethylmethacrylate (PMMA), polyvinylidene fluoride (PVDF), Polydimethylsiloxane (PDMS), polyethylene oxide (PEO), polyethylene glycol (PEG), Poly(vinylpyrrolidone) (PVP) , polystyrene (PS), and off-stoichiometry thiol-ene (OSTE) has been exploited as the protectors and significant impact on perovskite's optical and structural characteristics, which makes perovskite-polymer composite is promising candidate for optoelectronic applications [59–64].

Furthermore, the properties of composites are depends on the host polymer, type of solvent, blending ratio, and blend miscibility. The interaction between the polymer and solvent is quantified by the Flory-Huggins parameter in a modified Gibbs free energy equation. For solvents with higher solubility parameters, the values of  $\chi$  decrease; for solvents with lower solubility parameters, the values of  $\chi$  increase as increasing solvent volume fraction [65–67].

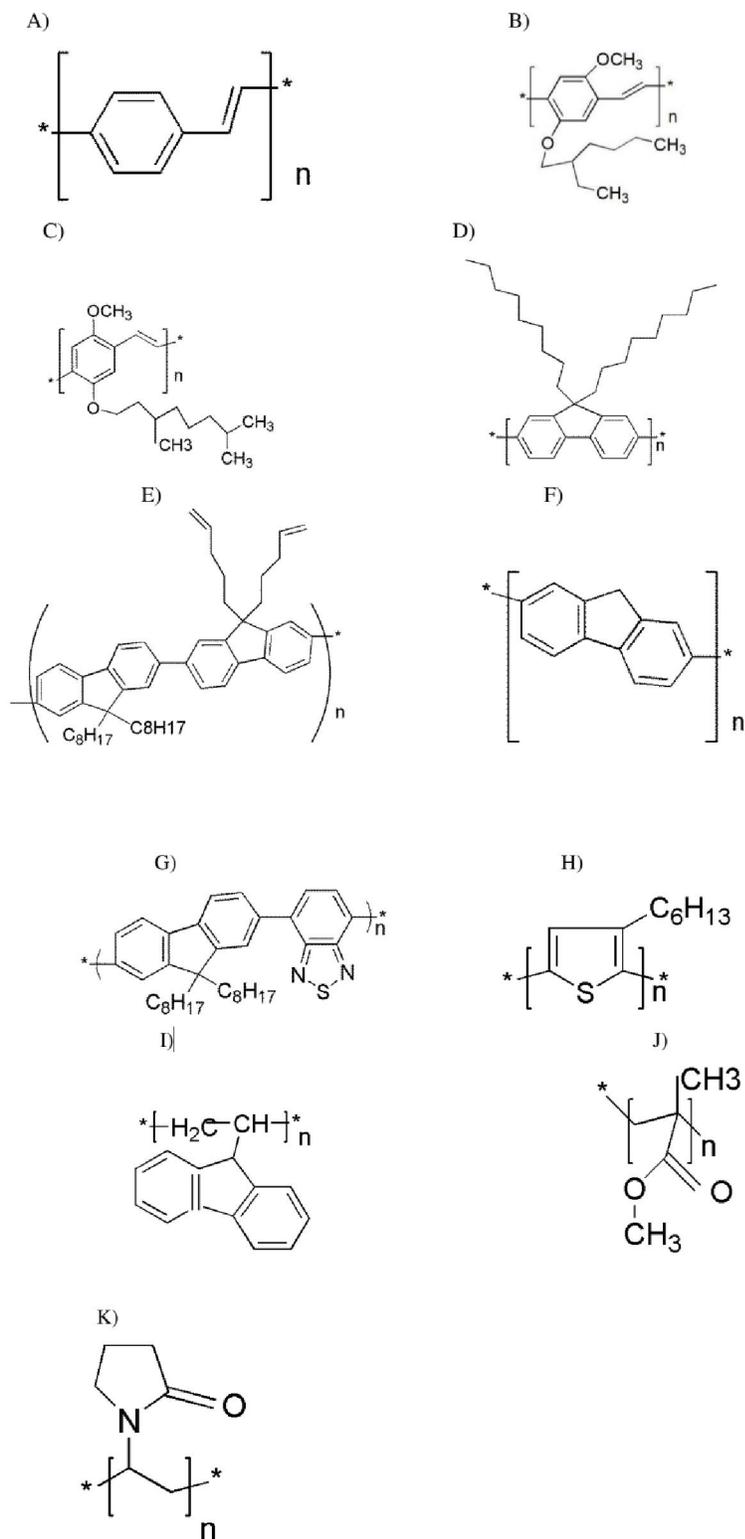


Figure 1.4. Chemical Structure of Polymers (A) PPV B) MEH-PPV C) MDMO-PPV D) PFO E) PFOpen F) PF G) F8BT H) P3HT I) PVK J) PMMA K) PVP.

Furthermore, after combination of conjugated polymers with different materials including perovskite reveals interesting of morphology, structural and optical properties, and enhanced performance of devices[68–73]. Therefore, conjugated polymer/perovskite nanocomposites are potentially very interesting active materials for broadly tunable LEDs, carefully choosing the active materials and blend content, it is possible to generate almost any required specific color, including white [74].

## **1.2. Statement of the Problems**

To fulfill the world's energy needs in the future year, there is a great deal of interest in and research being done in the subject of optoelectronics devices. Scholars are currently interested in metal halide perovskite because of its superior properties, which include its inexpensive cost of materials, narrow FWHM, and ability to be processed in solutions. The external quantum efficiency (EQE) of CsPbX<sub>3</sub> NCs increased quickly and reached over 20% from the time of the initial study of CsPbX<sub>3</sub> NCs-based LEDs until recent date [9,75]. Furthermore, compared to QLEDs and OLEDs, perovskite-based light-emitting diodes are rapidly growing [22,76,77].

For lighting and display applications, PeLEDs have significant potential because to their many advantages, including low cost, high PLQY, band gap adjustable, high defect tolerance, and ambipolar charge transfer [78]. Improvements in the properties, stability, and functionality of perovskite-based devices are still required for practical commercialization. Thus, appropriate encapsulation, ligands, polymer coating and mixing, inorganic doping, and their combination have been developed and shown to improve the characteristics and photo stability of perovskite, thereby resolving these issues [79]. Polymers with excellent features, such as being lightweight, environmentally friendly, flexible, easily processed, and able to form films, show promise for improving the device's performance and properties when combined with others. Our study suggests that olive oil is a multiligand species that is environmentally friendly, making it a better option than oleic acid, a popular carboxylic.

Therefore, the main task of this work are as follows: i) to investigate the impact of ligands on the optical and structural characteristics of all-inorganic perovskite CsPbBr<sub>3</sub> NCs

prepared by supersaturated recrystallization method at RT, which doesn't require inert gas and high temperature. Next, synthesize and characterized polymer-perovskite composite the characteristics relative to their pristine.

### **1.3 . General Objective**

The main focus of this dissertation is to synthesize and characterize conjugated polymer-perovskite NCs nano composite for optoelectronics.

#### **1.3.1. The Specific Objectives**

- To investigate optical and structural properties of room temperature synthesized all-inorganic CsPbBr<sub>3</sub> perovskite nanocrystal with olive oil and oleylamine.
- To study conjugated polymer-perovskite nanocomposites miscibility, structural, and optical properties.
- To synthesis and characterize of polymer-mixed halide perovskite composites

### **1.4. Significance of the Study**

This work focus on easily processable, eco-friend and cost effective approach for synthesis all inorganic perovskite CsPbBr<sub>3</sub> NCs and conjugated polymer/perovskite nanocomposite emissive nanolayer for optoelectronic device applications. The outputs envisaged are:

- ✓ It provides good insight to the researchers about the cost-effective approach and eco-friend approach which is explored in this paper.
- ✓ This gives a direction for stakeholder and researchers engaged in the field of emerging perovskite materials based optoelectronic devices which indicates that there are opportunity to solve issue related to perovskites and applied for practical. Here not only consider it efficiency but also by considering the desires of energy sectors compared to other materials.

### **1.5. Research Questions**

In this project , we have to explore the following questions;

- How does the various capping ligands influence the properties of modified perovskite the properties of cesium lead halide perovskite NCs?

- What is the impacts were investigated on the structure and propertie composites when incorporated on perovskite NCs into conjugated polymer?
- What is the relationship between commonly used ligand carboxylic acid (oleic acid) and olive oil?

## 1.6. The Conceptual Frameworks

This parts of the dissertation reveals that overall synthesis , and characterization of cesium lead halide/mixed halide nanocrystals, conjugated polymer MDMO-PPV, and their composites. Accordingly , Figure 1.5 illustrates that the conceptual frameworks of this dissertation.

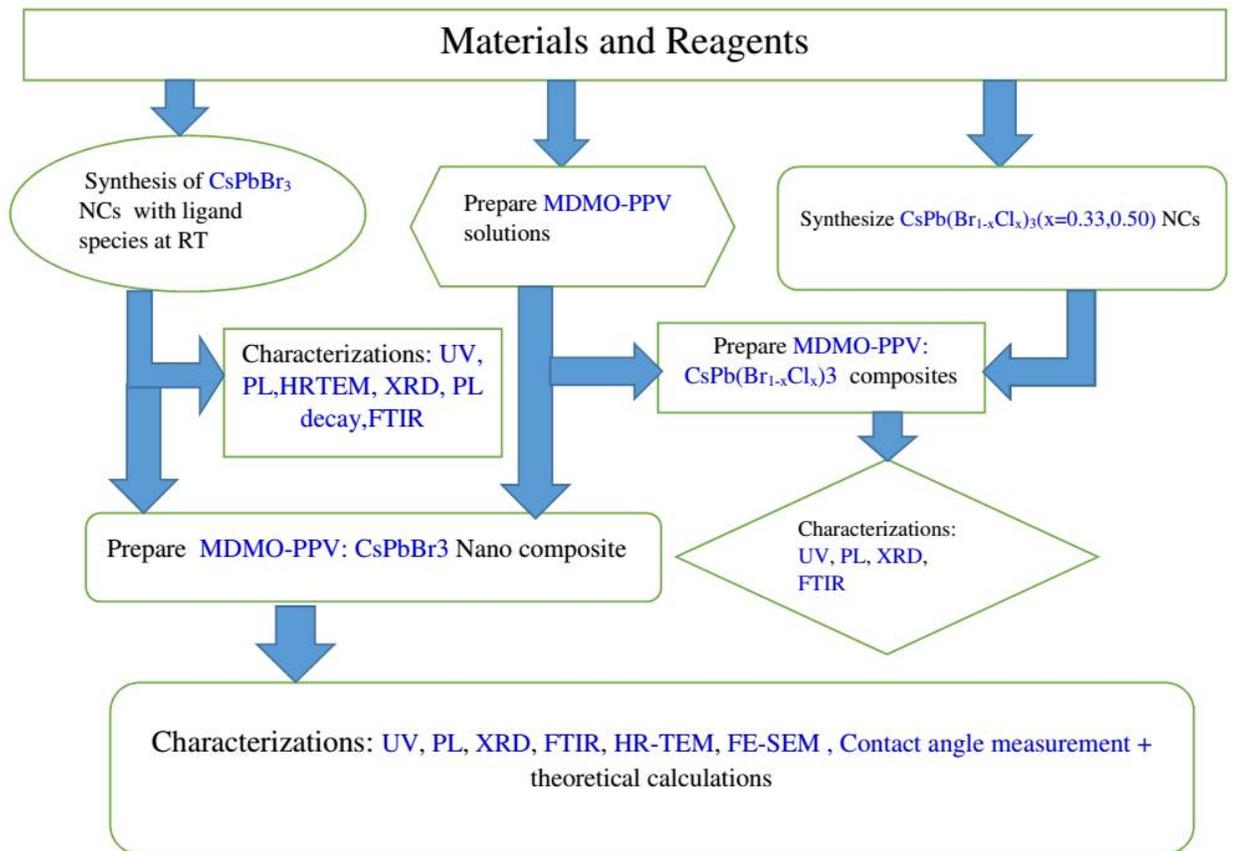


Figure 1.5. The Conceptual Frameworks

## 1.7. Dissertation Organization

The aim of this work is to prepare conjugated polymer-perovskite nanocomposite and explore the properties of conjugated polymer-perovskite nanocomposite for optoelectronic device application; in particular focus on pure cesium lead bromide and cesium-based mixed halides (Br/Cl NCs) which are essential for optoelectronic application including light-emitting diode. The conjugated polymer-perovskite (MDMO-PPV: CsPbBr<sub>3</sub> or CsPb(Br<sub>1-x</sub>/Cl<sub>x</sub>)<sub>3</sub>) Nanocomposite. It can be organized as follows:

Chapter 1. The introduction outlines the background, problem statements, research questions, objectives, and significance of the research in brief.

Chapter 2. Brief overview about the fundamental knowledge of perovskite, effects of ligands on all-inorganic lead halide perovskite, mathematical theories, and polymer-perovskite composites properties, and recent progresses.

Chapter 3. Describe the methods such as synthesis and characterization, and mention materials (chemicals and reagents) which utilized in this dissertation

Chapter 4. Investigate the optical and structural characteristics of the all-inorganic cesium lead bromide perovskite nanocrystals synthesized with olive oil and oleylamine at room temperature.

Chapter 5. Study the miscibility, nano-structure, and optical properties of conjugated polymer-perovskite nanocomposite

Chapter 6. Synthesis and Characterize the of polymer- mixed halide perovskite composites

In the last chapter, we included summary and recommendations which highlight for applications and future study.

## Chapter Two

### 2. Review Literatures

#### 2.1. Overview

Perovskites are materials with chemical formula of  $ABX_3$ , where A is an organic or inorganic cation, B is metal cation, and X is halide ions or oxides, which was discovered in 1839 by Russian mineralogist. Due to their remarkable qualities, such as cost-effectiveness and solution processability, these materials have drawn interest from the scientific community in the field of optoelectronic applications. The temperature affects the structure of perovskite. Accordingly, at room temperature (RT), the structure takes on the form of an orthorhombic or tetragonal phase, but at high temperatures, it transforms into a more stable cubic phase. It has been observed that the stability of perovskite structures depends on both the octahedral factor ( $\mu$ ) and the tolerance factor. While it is believed that  $CsPbBr_3$  NCs are in the cubic phase, some studies reveal that they have locally ordered subdomains where  $PbX_6$  is orthorhombic tilting to form a local two-dimensional (2D/3D) twin grain boundary; these twin boundaries are then rearranged in response to temperature changes, causing the orthorhombic and cubic phases to transform [25]. As it was reported first time by Goldschmit factor predicts the structure and stability of perovskite materials, as shown in Figure 2.1 [80]. Mathematically, structural tolerance-factor can be expressed as;  $t\sqrt{2}(R_B+R_X)=R_A+R_X$ , and  $\mu \cdot R_X=R_B$ , where  $R_A$ ,  $R_B$ , and  $R_X$  are ionic radius for cations, B metal ion and X is halide anions [35,47]. The crystal structure is most stable when  $t = 1$ , and deviations from unity are likely to result in deformation. Typically, the formation of the cubic halide perovskite crystal occurs when  $0.9 < t < 1$  and  $0.44 \leq \mu \leq 0.90$ . When t factor can range between 0.7 and 0.9 due to a large B ion or a small A ion, producing orthorhombic, rhombohedral, or tetragonal structures [47,81]. By the end of 1990, Mitzi et al. produced and characterized lead-free perovskite, such as cesium tin halides and cesium germanium chloride. Field-effect transistors were created using cesium tin halide in the same year [82]. Around the same time, Era and his colleagues used a layered perovskite chemical called bis (phenethylammonium) tetraiodo plumbate  $[(C_6H_5C_2H_4NH_3)_2PbI_4, PAPI]$  as an emissive layer to study the first electroluminescence perovskite at liquid-nitrogen temperature [83].

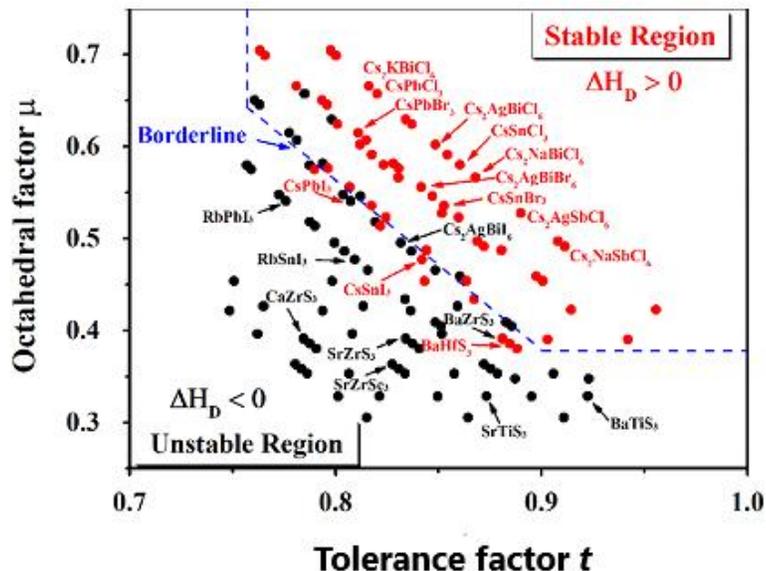


**Figure 2.1** Map of  $(t, \mu)$  for 138 perovskite compounds considered in our work. Red dots mean  $\Delta H_D > 0$  (predicted to be stable), and black dots mean  $\Delta H_D < 0$  (predicted to be unstable) [84].

Various studies were conducted organic-inorganic perovskite based solar cells in order to replace dye molecules [58,85]. Nevertheless, lead halide perovskite has not been researched up to this point. In 2014, it was reported that PeLEDs made using 3D lead halide perovskite at room temperature EL had an EQE of approximately 0.1%, with green luminescence of approximately  $364 \text{ Cdm}^{-2}$  and infrared EQE of approximately 0.76% [58]. This low device efficiency was due to the poor morphology, low PLQY of perovskite film [85]. The inorganic perovskite  $\text{CsPbX}_3$  NCs ( $X = \text{halide ions}$ ) have become a promising class of light-emitting materials in the last ten years because of their composition-dependent, tunable band gaps ranging from the violet to the near-infrared [86] and narrow FWHM (Figure 2.2).

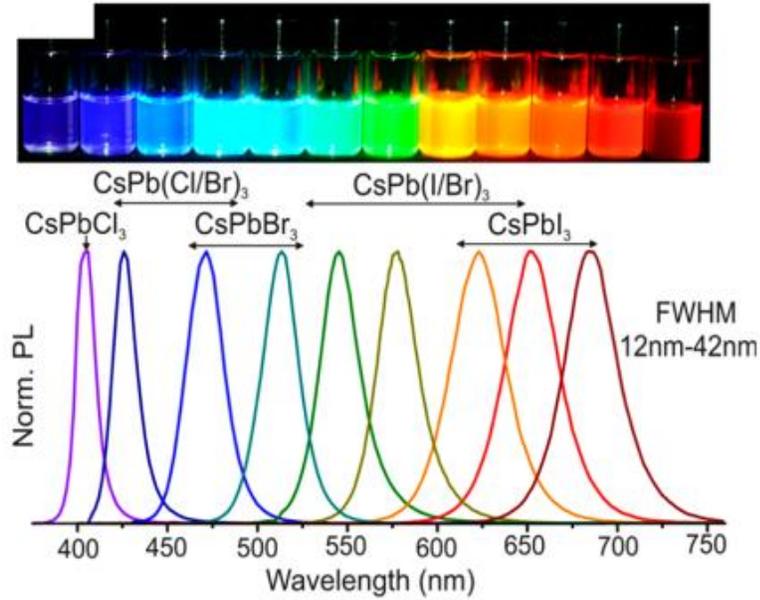


**Figure 2.2** The  $\text{CsPbX}_3$  ( $X = \text{Cl}, \text{Br}, \text{I}$ ) NCs have narrow FWHM and bright emission, with composition-tunable bandgap energies covering the whole visible spectral region [40].

All-inorganic  $\text{CsPbX}_3$  perovskite NCs synthesized by solution-phase chemistry approach and exhibits excellent thermal stability and high PLQY reach 90%. Because of they owing unique properties,  $\text{CsPbX}_3$  NCs are most attractive for electroluminescence (EL) application [87]. Song et al first time investigated green LED-based on  $\text{CsPbBr}_3$  QD and found maximum external quantum efficiency of 0.12% [38]. Furthermore, the PLQYs of  $\text{CsPbBr}_3$  and cesium lead iodide ( $\text{CsPbI}_3$ ) NCs can reach over 90% in the green and red spectral ranges, respectively, and exhibit high-efficiency light-emitting diodes [86]. With this, it was reported that the performance of green light-emitting of  $\text{CsPbBr}_3$  has maximum luminance, maximum current efficiency ( $\text{CE}_{\text{max}}$ ), maximum power conversion efficiency ( $\text{PCE}_{\text{max}}$ ), and maximum external quantum efficiency ( $\text{EQE}_{\text{max}}$ ) of  $496,320 \text{ Cdm}^{-2}$ ,  $37 \text{ CdA}^{-1}$ ,  $331 \text{ mW}^{-1}$ , and 9.3%, respectively with operating voltage 2.5 at  $10^3$ , 2.9 at  $10^4$  [88]. Additionally in 2017, it was reported that, with an operating voltage of 4.1 at  $10^3$ , the perovskite quantum dot light-emitting performance had maximum luminance,  $\text{CE}_{\text{max}}$ ,  $\text{PCE}_{\text{max}}$ , and  $\text{EQE}_{\text{max}}$  of  $1660 \text{ Cdm}^{-2}$ ,  $26.2 \text{ CdA}^{-1}$ ,  $31.7 \text{ lmW}^{-1}$ , and 8.73%, respectively [89].

## 2.2. Effects of Ligands on All-inorganic Cesium Lead Halide Perovskite NCs

Perovskite NCs are PL efficient materials because the defect states in metal halide perovskite's band structure are essentially "defect tolerant" and are likely to locate in the valence or conduction bands. Knowing the chemistry and physics underlying the defect states as well as the surface chemistry of NCs, of which halide vacancy is the most common defect in these materials, is essential [90,91]. Ligands are molecules that significantly affect a material's performance, optical characteristics, and structural characteristics. Notably, amine and carboxylic acid are often employed ligands in the synthesis of perovskite nanocrystal [92–94]. It is widely known that ligands, which are also necessary for the production of NC, protect the NC surface, restrict inter-particle aggregation, and modify both the chemical and physical properties of the resulting NC [90,91]. Because carboxylic acids and amines, namely oleic acid (OA) and oleylamine (OAm), are effective ligands for ensuring the control of NC size and shape during the synthesis stage, they also help with the ability to dissolve of metal halide precursors. Moreover, a specific quantity of ligands must be incorporated in order to control the shape, stability, and optical characteristics of metal halide perovskite nanocrystal. However, they continue to deteriorate, though, which lowers their performance for use in display and lighting technology [92–96].

Therefore, selecting suitable ligands is crucial to producing high-performing perovskite for use in lights and displays. In order to maximize the charge transfer property and minimize surface defects of colloidal semiconductors and perovskite nanocrystal (NCs), several researchers investigated numerous substitute ligands for the widely used ligands such oleic acids, and oleylamine [91,97,98]. The selection of suitable ligands is a major factor in improving the surface chemistry, stability, and optical properties of optoelectronic devices, thereby improving their overall performance.

## 2.3. Flory-Huggins Theory

Group contribution methods are commonly used to predict polymer solubility characteristics that are measured experimentally, as they are only available for a restricted set of polymers. According to Hildebrand, whose method is based on the idea that "like dissolves like," the square root of the cohesive energy density (CED) is the total solubility parameter ( $\delta$ ). Thus the solubility parameter ( $\delta$ ) is written as;

$\delta = \sqrt{CED} = \sqrt{\frac{\hat{U}_{vap}}{\hat{V}}}$ ,  $\hat{U}_{vap}$ ,  $\hat{V}$  are molar the molar heat of vaporization, and molar volume, respectively. Moreover, a significant entropic gain predicts the miscibility of two small organic molecules, despite an enthalpic cost resulting from the apparent differences in solubility parameters.

Hansen decomposed the solubility parameter into contributions of dispersion forces ( $\delta_d$ ), polar forces ( $\delta_p$ ), and hydrogen bonding ( $\delta_H$ ) to create a more encompassing picture of the CED[99,100]. When,

$$\Delta G_{mix} = \Delta H_{mix} - T\Delta S_{mix} < 0 \quad (2.1)$$

In which  $\Delta G_{mix}$ ,  $\Delta H_{mix}$ ,  $\Delta S_{mix}$  and T denotes the Gibbs free energy, enthalpy, entropy of mixing, and temperature, respectively. In contrast, the relation for the intermolecular interactions between the anti-solvent and the perovskite should be  $G_{mix} > 0$ , which will enable a wet perovskite film to dry. Thus, when combining long-chain macromolecules,  $\Delta S_{mix} \approx 0$ , and  $\Delta H_{mix} > 0$ , leading to  $\Delta G_{mix} > 0$ . Notably, the stability condition for single phase  $(\frac{\partial^2 \Delta G_{mix}}{\partial \phi_i^2})_{T,P} > 0$ , where  $\phi_i$  is the volume fraction of component i and P is pressure [101–103].

#### 2.4. Polymer-Perovskite Based Composites

The insulating polymer polymethyl methacrylate (PMMA) was combined with all-inorganic CsPbBr<sub>3</sub> perovskite nanocrystals using the solvent toluene in a solution blending technique. This example shows that effective light emission may be obtained utilizing both bulk and CsPbBr<sub>3</sub> perovskite nanoparticle, based on the Amplified Spontaneous Emission (ASE) of the CsPbBr<sub>3</sub> thin disk. Furthermore, the CsPbBr<sub>3</sub>/PMMA thin disk's optical characteristics were effectively preserved as a result of perovskite's inclusion into the polymer, which enhanced the active material's properties [104]. Interestingly, in 2021, Wang and his colleagues reported that CsPbBr<sub>3</sub> QDs embedded into PMMA polymer shows that best green emission with PLQY  $\approx$  82.7%, FWHM  $\approx$  18.6 nm, and life time  $\approx$  32.5ns. In addition to that, CsPbBr<sub>3</sub>/PMMA composite exhibits better stability under ambient condition [105]. In the same year, Yang et al. result illustrates that passivation of CsPbBr<sub>3</sub> QDs with PVDF exhibits

excellent structural stability, suppress phase transformation and enhanced optical performance [106].

Zhang and co-workers investigated maximum luminance increment from 350 to 11 600  $\text{Cdm}^{-2}$  as well as current efficiency 0.26 to 7.19  $\text{CdA}^{-1}$  when a polyvinyl pyrrolidone (PVP) buffer layer inserted between the ZnO electron transport layer (ETL), and  $\text{CsPbBr}_3$  emissive layer (EML). On the other hand, they achieved maximum brightness, EQE, and CE of 91,000  $\text{Cdm}^{-2}$ , 10.43%, and 33.9  $\text{CdA}^{-1}$ , respectively using modified active layer film by incorporating insulating polymer PVP at the interface and  $\text{CH}_3\text{NH}_3\text{Br}$  (MABr) for lattice [39,107].

In 2020, 5% PVP doped  $\text{CsPbBr}_3$  based device with structure of glass/ITO/PEDOT:PSS/ $\text{CsPbBr}_3 + x\%$  PVP/TPBi/LiF/Ag shows better luminance, CE, EQE such as 1734  $\text{Cdm}^{-2}$  (7.0V), 0.438  $\text{CdA}^{-1}$  (4.0V), and 0.139% (4.0 V), respectively. When 1.5 mg of PVP interlayer is present in this scenario, the device shows three times more EQE and CE with an extremely green color, and stronger EL properties than the control PEDOT:PSS/ $\text{CsPbBr}_3 + \%X$  PVP [108]. Thus, this finding indicates that using PVP at the interface can slow down electron injection and balanced the charge injection as compared to PMMA [98,104].

Recent studies have proposed that hybrids with special features such conjugated polymers might enhance the stability and other characteristics of perovskite. In 2015, an efficient charge transfer mechanism is demonstrated at the interface of  $\text{CH}_3\text{NH}_3\text{PbI}_3$  /MEH-PPV, and growing perovskite within a polymer matrix results in a new kind of nano composite. Furthermore, perovskite-polymer composite shows a smooth morphology and fine perovskite dispersion in the polymer matrix makes improvement in the film-forming ability and stability of perovskite-based optoelectronic devices [109]. However, inorganic perovskite such as pure cesium lead chloride  $\text{CsPbCl}_3$  and  $\text{CsPbBr}_3$  exhibits PLQY 1% and 78% respectively. These suggest that there may be a way to balance between luminescence efficiency and emission wavelength due to the adjustable band gap. The first white light emission was investigated by using orange emitting MEH-PPV and blue EL perovskite  $\text{CsPbBr}_x\text{Cl}_{3-x}$  owing device configuration, ITO /NiOx/perovskite-polymer composite/TPBi/LiF/Al as represented in Figure 2.3. The transfer of excitons from the blue nanocrystal to the orange polymer through Förster or Dexter energy transfer mechanisms

was measured in this instance using time-resolved photoluminescence spectroscopy, and white-light emissions were produced by adjusting the ratio between the nanocrystal and the polymers.

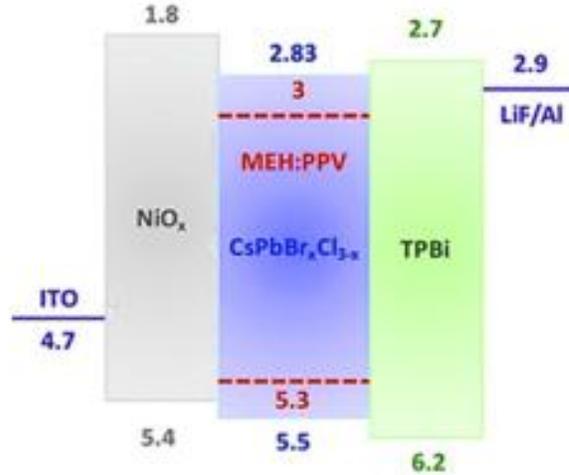


Figure 2.3 Energy Diagram of CsPbBr<sub>x</sub>Cl<sub>3-x</sub>/MEH-PPV [87].

It was observed that PL lifetime was decreased due to exciton energy quenching for perovskite to conjugated polymer [87]. In 2018, it was reported that PL was decreasing when CsPbBr<sub>3</sub>NCs were incorporated into MEH-PPV. The introduction of CsPbBr<sub>3</sub> NCs into the light-emitting conjugated polymer improved the stability and process ability of their hybrid [110]. In comparison to reference PeLEDs without a PFO buffer layer, the device's performance is improved when conjugated polymer PFO is incorporated between the hole injecting layer and active layer (CH<sub>3</sub>NH<sub>3</sub>PbBr<sub>3</sub>). This is evident in the luminous intensity, CE<sub>max</sub>, and EQE<sub>max</sub> with corresponding values 8,139 Cdm<sup>-2</sup> to 30,150 Cdm<sup>-2</sup>, 7.20 CdA<sup>-1</sup> to 10.05 CdA<sup>-1</sup>, and 1.73% to 2.44%, respectively.

Furthermore, passivates the shallow trap to ensure increasing hole injection and increases the coverage of perovskite film. Addition of a high concentration of conjugated polymer between the hole injection layer and active layer attributes, which suppresses the EL reduction from exciton dissociation and quenching through charge recombination and/or non-radiative energy transfer at the interface. The reduction of EL was due to the thicker size of the conjugated polymer that causes trap exciton at the interface leads decreasing in hole injection [111]. The composite was produced by Qaid S et al. when CsPbBr<sub>3</sub> QDs were

added to conjugated polymer PFO. This result exhibits better thin film morphology, adjusted thin-film optical characteristics, and promoted non-radiative energy transfer from PFO to CsPbBr<sub>3</sub> QDs [44]. The maximum peak at 385 nm sharply dropped without shifting when different amounts of PQDs were added to the binary conjugated polymer blend PFO/MEH-PPV, while the peak absorbance of the shoulder at 294 nm slightly increased. On the other hands, the addition of perovskite quantum dots as a third component into the binary polymer was vital to facilitate triplet Forster resonance energy transfer(FRET) as well as tuning the FRET parameters [112]. In 2018, it was presented that full-color tunability approach through binary hybrid blends between conjugated polymer (PFO) and perovskite NCs due to their easily form solution, good film-forming property of polymer, and good emission of blend film [74].

According to a report, increasing the amount of perovskite QDs in MEH-PPV/PFO caused the grain size to grow, the lattice and dislocation to decrease, the Urbach tail to reduce, the steepness parameter to increase, and the non-radiative energy transfer process to be enhanced. The use such a kind of hybrid as an emissive layer in optoelectronic devices improving the performance of the device [112]. Therefore,the composites shows distinctive unique optoelectronic and mechanical properties, namely their solubility, flexibility, and electroluminescence which makes them beneficial to use as active layer material in optoelectronic devices [113].Furthermore,combining perovskite with polymers proved to be a simple solution, as polymers benefit perovskite in a variety of ways, including easier system fabrication, improved mechanical performance, and improved luminescent properties [114].

Despite of that, incorporation of perovskite NCs into conjugated polymers improves the structural and optical properties of nanocomposites as compared to pristine. Thus, utilizing the mixture abundant polymer and perovskite NCs makes materials to have new opportunity for improvement of properties and performance of optoelectronic devices [44]. In addition, the composite of conjugated polymer with perovskite nanocrystals exhibits improvement of the stability of perovskite QDs and properties makes them used an active layer for optoelectronic applications.

The physical and optoelectronic properties of inorganic NCs depend on their geometric morphology. As it was known that oleic acid (OA) and oleylamine (OAm) are used as ligand reagents to synthesize CsPbX<sub>3</sub> NCs in common but suffer morphological control [115]. As of right now, adding more reagents allowed CsPbX<sub>3</sub> NCs to have controlled morphologies. Unfortunately, OA is unstable and readily degrades under wet conditions.

On the other hand, hot injection is the most common approach to synthesis CsPbX<sub>3</sub> NCs and achieve good crystallization of the films and achieved high QY. However, it require high temperature and inert gas. Thus, it is essential to have low-cost synthesis and control reaction time for large-scale production [115,116]. Therefore, RT is very important approach met desire such as easily synthesis and large scale production.

When compared to OA, olive oil is a type of widely used edible oil capping ligand that is easier to get from commercial markets and exhibits higher stability in the winter. Furthermore, using olive oil as a ligand reagent results in the synthsize of high-quality NCs with many NC morphologies [116]. As far as currently available research, there are just a few investigations on conjugated polymer-perovskite composite PFO/MEH-PPV/CsPbBr<sub>3</sub> QDs [117] , MEH-PPV/ CsPbBr<sub>3</sub>NCs [110],and PFO/ CsPbBr<sub>3</sub> [44] were reported about optical and structural properties. In these conditions, the perovskite nanocrystal was synthesized using precursor surfactant oleic acid or a mixture of OA and OAm but not with olive oil. Also, the most common light-emitting polymer, poly[2-methoxy-5-(3',7'-dimethyl octyl oxy) 1-4-phenylenevinylene (MDMO-PPV), is comparable to MEH-PPV and is utilized in the majority of plastic electronic devices. As per authors knowledge no study were conducted specifically MDMO-PPV - inorganic perovskite composite for optoelectronic applications. This polymer matrix has high crystallinity, processability, and film-forming ability [118–120]. Therefore, this study focused on the properties of a conjugated polymer MDMO-PPV:CsPbX<sub>3</sub> (X= Br and mixed halides Br/Cl) nanocomposite.

Furthermore, still the require efficiency is low for organic-inorganic perovskite so that recently researchers relies on all inorganic perovskite materials based optoelectronic devices which has relatively better chemical stability and high photoluminescence. However, all inorganic perovskite materials does not met the required properties and performance of devices having different problems such as stability due oxygen and moisture and other issues. As result different strategies are used to enhance those limitations and improve the performance of devices based on the all inorganic perovskite such encapsulation, composite with polymers /conjugated polymer and others. Thus , this study was mainly facous on the ligands effects on all inorganic Cesium lead bromide perovskite Ncs and MDMO-PPV-CsPbBr<sub>3</sub> nanocomposites were investigated when various amount of CsPbBr<sub>3</sub> incorporated. The CsPbBr<sub>3</sub> Ncs was synthesized using one of the typical ligand assisted methods called supersaturated recrystalizaion under room temperature, whihch is inexpensive and simple for preparation and scablity of productions.

## Chapter Three

### 3. Materials and Methods

This section contains the relevant experimental strategies and procedures applied in the experiments in this dissertation. Additionally mentioned were the reagents and chemicals utilized in this experiment. Here, the phase behaviors of conjugated polymer blends are described by FH lattice theory, for which the interaction parameter is estimated from contact angle measurement leading to solubility parameter. Other topics covered in this section include the measurement of contact angles, which comprises the determination of the wetting ability of surfaces on film samples of conjugated polymers and analysis of contact angles was conducted. Furthermore, materials such as polymers, perovskites, ligands, and solvent lists are mentioned; experimental methods and techniques for optical, structural, electrochemical, and morphological characterizations were described.

#### 3.1. Materials

Lead bromide ( $\text{PbBr}_2$ , 99%, Delhi, AR chemicals, India), cesium bromide ( $\text{CsBr}$ , 99.9%, Sigma-Aldrich), lead chloride ( $\text{PbCl}_2$ , 99.0%, Delhi India), oleic acid (98%, Sigma-Aldrich, Darmstadt, Germany), oleylamine (70%, Sigma-Aldrich), Olive oil (OO, Nice), acetone ( $\geq 99.5\%$ , Sigma-Aldrich), hexane ( $\geq 97.5\%$ , Sigma-Aldrich), isopropanol ( $\geq 99.5\%$ , Delhi, India), Distil water, toluene ( $\geq 99.5\%$ , AR chemicals, Delhi, India), *N,N*-dimethylformamide (DMF, 99.5%, AR chemicals, Delhi, India), ethyl acetate (99%, AR chemicals, Delhi, India), poly[2-methoxy-5-(3',7'-dimethyloctyloxy)-1-4-phenylene vinylene] (MDMO-PPV,  $= 120,000 \text{ g}\cdot\text{mol}^{-1}$ ) were used in this study. The chemicals were used as received without further purification

#### 3.2. Synthesis Methods

There are many different techniques applied for synthesis and characterization. Some of the techniques used for synthesis of perovskite NCs such as Hot-Injection method, Ligand-assisted Reprecipitation (LARP) method, Polar solvent controlled ionization method, and others. The commonly used methods for the synthesis perovskite NCS are hot-injections and Room temperature. In this study Ligand-assisted Reprecipitation (LARP) method at

room temperature for synthesis of perovskite NC rather hot-injection methods which requires inert gasses, and high temperature.

### **3.2.1. Hot-Injection Method**

The hot-injection(HI) synthesis process, which involves injecting precursors into a supersaturated solution at elevated temperatures, is among the most convenient techniques for producing PNCs. When synthesized using the HI method, the temperature at which the cation or anion precursor is injected, the reaction time, the concentration of the precursors, and the ratio of surfactants to precursors are the key parameters that allow control over the size, size-distribution, and shape of colloidal NCs. The HI technique, for all its benefits, is nevertheless expensive and challenging to create on a big scale since it needs inert gasses and a high temperature [23,29,40].

### **3.2.2. Ligand-assisted Reprecipitation Method**

Ligand-assisted Reprecipitation (LARP) technique is simple to use, quick to recycle, inexpensive, low temperature, and suitable for large-scale manufacturing outdoors [32,121]. Because RT uses ambient temperature rather than an inert environment, it is therefore this method better for synthesizing high-quality film as compared to HI. Compared to HI, LARP is widely used to synthesis perovskite NCs at RT [23]. Supersaturated recrystallization, a kind of LARP technique, was used in this work because it is an easy, affordable, and large-scale production without the need for inert gas or high temperatures.

## **3.3. Characterization Techniques**

The morphology, topography, crystallographic information, compositions, structural, and optical properties of prepared samples could be characterized by some techniques of Spectroscopy and microscopy [122–124]. Those techniques are explained as follows;

### **3.3.1. X-Ray Diffraction**

X-ray diffraction (XRD) technique is the most common technique used for determining the crystal structure of materials based on the diffraction light. In this scenario, amorphous materials are not organized in periodic array so they do not scatter light coherently. Elastic scattering is the mechanism by which electrons that have occupied specific energy levels around an atom must re-emit the energy of another with equal energy value as the first one

since the energy absorbed is insufficient to liberate the electron. The scattered x-rays may constructively interfere at particular x-ray incidence angles; this phenomenon is known as diffraction, and it causes an intensity peak to appear in the XRD diffractogram. The device XRD is called an X-ray diffractometer [122,123]. Here X-ray diffraction XRD (Rigaku mini flex-300/600 diffractometer, Tokyo, Japan,  $\text{CuK}\alpha$ ,  $\lambda = 1.5406 \text{ \AA}$  at 40 kV and 15 mA) has been used in this work to determine the crystalline structure of the  $\text{CsPbBr}_3$  perovskite NCs,  $\text{CsPb}(\text{Br}_{1-x}\text{Cl}_x)_3$ , MDMO-PPV, MDMO: $\text{CsPbBr}_3$  composite and also MDMO: $\text{CsPb}(\text{Br}_{1-x}\text{Cl}_x)_3$  Composite.

### **3.3.2. Scanning Electron Microscope**

The most popular kind of electron microscopy is the scanning electron microscope (SEM). It uses a method similar to scanning on focused microscopes, but with high resolution and much greater depth of field, to investigate microscopic structure by scanning the surface materials .

A concentrated electron beam that traverses a specimen's surface produces a SEM images [123]. It measures morphology (particle size and shape), content (elements and compounds), topography (topography map, surface attributes), and crystallographic information (atom arrangement) [122,123]. In this work, Field–Emission Scanning Electron Microscope (FE-SEM) (FE-SEM, MAIA3 XMH, TESCAN BRONO SRO, Kohoutovice, Czech Republic) was applied to investigate the morphology and structural properties of samples.

### **3.3.3. High Resolution Transmission Electron Microscope**

It is an invaluable tool for the characterization of nanostructures, providing a range of different imaging modes with the ability to provide information structure at the ultimate sensitivity. It offers all the data from a traditional TEM in addition to information on the crystal structure of individual particles. Additionally, determine the materials' crystallinity. In this study High resolution transmission electron microscope (HRETM)( Model: JEOL, JEM-2100) with an operating voltage of 200 kV) with high resolution has be used to examine the morphology and structural characteristics of  $\text{CsPbBr}_3$ , MDMO-PPV and their composites [122,123].

### **3.3.4. Ultra Violet Visible Spectroscopy**

The optical characteristics of a material, such as its band gap, can be detailed using absorption spectroscopy. Ultra Violet Visible (UV-Vis) spectroscopy examines the absorption spectroscopy in range ultraviolet to Visible. This technique uses electromagnetic radiation in the UV visible range to interact with a material. The law of Lambert Beer is the cornerstone of UV-Vis [123–125].

UV-visible spectrophotometer (SHIMADZU UV-2600, Kyoto, Japan) was employed to determine the absorption spectra of samples. The baseline for this experiment was created using a quartz cuvette that contained just solvent for solution samples. A blank glass substrate was utilized as the baseline before the sample was added to the spectrometer for the film measurements.

### **3.3.5. Photoluminescence Spectroscopy**

The Photoluminescence (PL) spectroscopy (SHIMADZU RF-6000, Kyoto, Japan) was used to provide the information about a material's emission properties. PL spectroscopy is crucial as the NCs created in this work were used in optoelectronic domains. A species releases light PL when some photons have been absorbed. PL spectroscopy is essentially a contactless, non-destructive technique for examining any species' electrical structure. In this approach, the sample is stimulated with a specific wavelength of light. In the event of a radiative process, the electron eventually returns to ground level and releases light [123,125].

There are two monochromators in the system. The excitation monochromator selects the excitation wavelength, and the emission monochromator scans the emission in order to measure the PL. Typically, both monochromators are perpendicular to one another to reduce light scattering [125].

### **3.3.6. Time Correlated Single Photon Counting**

Time Correlated Single Photon Counting (TCSPC) (Model: Fluorolog 3 TCSPC, Horiba, USA) used to investigate the PL decay time of samples. TCSPC is a widely utilized instrument which used to investigate the excited state dynamics of semiconductor materials. Using TCSPC, photon arrival timings are gathered in time-resolved photoluminescence spectroscopies. A pulsed excitation source must be used because of the nature of this approach, which is time-resolved. The spontaneous nature of light emission from the excited

state means that the only feasible conclusions are estimates of the likelihood that a single molecule will produce a photon within a certain time frame. For a single photoluminescent molecule, the number of molecules within the excited state generally corresponds to the emission intensity of the molecule [126].

### **3.3.7. Fourier Transform Infrared Spectroscopy**

Fourier Transform Infrared (FTIR) is a technique apply to identify functional groups in chemical compounds. One can perform FTIR spectroscopy in the 4000-400  $\text{cm}^{-1}$  range. There are two uses for this FTIR analysis. One is that samples in the solid, liquid, or gas phase can be used by the transmittance approach, which produces high signal-to-noise ratios [123,127]. Here, samples' FT-IR spectra (PerkinElmer Spectrum Two FT-IR Spectrometer )were recorded at a resolution of 4  $\text{cm}^{-1}$  by the use of attenuated total reflection (ATR) sampling. Specifically, the surface composition and functional groups of the produced perovskite NCs, polymers, and polymer-perovskite NCs composites were examined in this dissertation.

### **3.3.8. Contact Angle Measurement**

The contact angle analyser(Phoenix 300+/LCA10, SEO Co. Ltd., Korea) was used to measure water contact angle. Here, measuring contact angles is made easy by finding the angle of a liquid drop with a solid surface at its base. With properly prepared solid surfaces, contact angles are reasonably easy to measure, therefore this approach of calculating the solid-vapor as well as the solid-liquid interfacial [128].

### **3.3.9. Electrochemical Impedance Spectroscopy**

Electrochemical characterizations can be used to determine how the materials behave electrochemically under different electrochemical circumstances. One method of calculating impedance is to apply a small-amplitude sinusoidal voltage to the electrode being studied. This produces a current, the amplitude and phase angle of which are measured in relation to the applied sinusoidal voltage. In this study, Electrochemical Impedance Spectroscopy (EIS) ( Bio-Logic, SAS, France) analysis was conducted in the frequency range of 10 mHz to 100 KHz [129]. According to the EIS measurement, changes in applied bias voltage cause a shift in the charge transfer resistance, which alters carrier extraction.

## Chapter Four

### 4. All-Inorganic CsPbBr<sub>3</sub> Perovskite Nanocrystals Synthesized with Olive Oil and Oleylamine at Room Temperature

#### 4.1. Introduction

Halide perovskites (HPs) have the general chemical structure of ABX<sub>3</sub>, where A [methylammonium (MA) CH<sub>3</sub>NH<sub>3</sub><sup>+</sup>, formamidinium (FA) CH(NH<sub>2</sub>)<sub>2</sub><sup>+</sup>, methylhydrazinium CH<sub>3</sub>(NH<sub>2</sub>)<sub>2</sub><sup>+</sup>, aziridinium (CH<sub>2</sub>)<sub>2</sub>NH<sub>2</sub><sup>+</sup> and cesium Cs<sup>+</sup>] and B (lead Pb<sup>2+</sup>, tin Sn<sup>2+</sup>, and germanium Ge<sup>2+</sup>) are cations and X is anions (chlorine Cl<sup>-</sup>, bromine Br<sup>-</sup>, and iodine I<sup>-</sup>) [36,130–135]. When these HPs serve as a semiconducting layer for the electronic and optoelectronic devices, they share some common properties such as defect tolerance, large absorption coefficient, high dielectric constant, low exciton binding energy, long charge carrier diffusion length, high charge mobility, and tunable bandgap [136–141]. Hence, the state-of-the-art devices show the power conversion efficiency of ~26% for photovoltaic (PV) cells, and more than 20% quantum efficiency for light-emitting diodes (LEDs) [132,142–145]. Furthermore, based on the aforementioned excellence properties, HPs have been applied to lasers, photodetectors, x-ray/γ-ray detectors, medical imaging devices, biosensors, photocatalysis, and luminescence solar concentrators [146–153]. However, the organic-inorganic hybrid HPs have an intrinsic problem in thermal stability originating from the organic cations such as MA and FA in the perovskite structure [154,155]. For example, MABr decomposes at around 250–350 °C [155]. Hence, to overcome this thermal instability, all-inorganic HPs such as CsPbX<sub>3</sub> (X= Cl, Br, and I) have been employed for perovskite electronics [28,155–161].

However, it is notable that the all-inorganic Cs-based perovskites with wide bandgap ( $E_g > 1.65$  eV) [162,163] also have some stability problems. First, Goldschmidt tolerance factor ( $t$ ) is  $(r_A + r_X) / \{\sqrt{2} \cdot (r_B + r_X)\}$ , in which  $r_A$ ,  $r_B$ , and  $r_X$  are the radius of cation A, cation B and anion X, respectively [21]. In the case of CsPbCl<sub>3</sub>, CsPbBr<sub>3</sub> and CsPbI<sub>3</sub>, each tolerance factor is 0.87, 0.816 and 0.805, respectively [164,165]. Considering that the cubic phase could be stable in the range of  $0.813 \leq t \leq 1.107$  [21], CsPbI<sub>3</sub> is structurally unstable among cesium

lead halides. Second, the Cs-based perovskites undergo a multiple polymorph transition such as orthorhombic, tetragonal and cubic depending on temperature and composition[166].

To be thermodynamically stable high-symmetry cubic phase, the perovskite should stay at the temperature more than 47°C for CsPbCl<sub>3</sub>, 130°C for CsPbBr<sub>3</sub> and 300 °C for CsPbI<sub>3</sub>, indicating that CsPbI<sub>3</sub> is the most challenging compound in spite of its promising energy bandgap ~ 1.73 eV [167–170]. Note that CsPbCl<sub>3</sub> and CsPbBr<sub>3</sub> have each bandgap of ~3.03 eV and ~2.25 eV, respectively[171]. Furthermore, it is notable that CsPbI<sub>3</sub> undergoes a phase transition from black  $\gamma$ -phase to yellow  $\delta$ -phase (i.e., non-perovskite with  $E_g \sim 2.82$  eV) resulting in an undesirable compound for perovskite electronics [172]. Third, according to Li and coworkers, the thermal stability of Cs-based perovskites are in the sequence of CsPbCl<sub>3</sub> > CsPbBr<sub>3</sub> > CsPbI<sub>3</sub>, because its structural change was observed at 500°C for CsPbCl<sub>3</sub>, 400 °C for CsPbBr<sub>3</sub> and 200°C for CsPbI<sub>3</sub>, respectively, based on *in-situ* x-ray diffraction experiments as a function of temperature in ambient conditions [173,174]. Hence, we notice that CsPbCl<sub>3</sub> and CsPbBr<sub>3</sub> are superior to CsPbI<sub>3</sub> from the stability point of view. In this work, we may focus on green-emitting CsPbBr<sub>3</sub> perovskite semiconductor [175,176].

In 1958, Møller reported the structure and photoconductivity of CsPbX<sub>3</sub> crystals (X= Cl, Br, and I) [156]. Then after more than five decades, in 2015, Kovalenko and coworker invented a *hot-injection* (HI) method for synthesizing CsPbX<sub>3</sub> (X= halide or its mixture) colloidal quantum dot materials with oleic acid (OA) and oleylamine (OAm) surface ligands [40]. Then after one year, Zeng and coworker invented another method called *supersaturated recrystallization* (SR) for synthesizing CsPbX<sub>3</sub> nanocrystals (NCs) with OA and OAm at room temperature [177]. In 2019, Shi and coworker tried to replace OA with an edible ‘olive oil (OO)’ using the HI method[116]. Then recently, Jing and coworker tried to replace OA with another ligand called 4,4'-Azobis(4-cyanovalericacid) (CA) at room temperature because OA and OAm can be detached easily from the surface of CsPbX<sub>3</sub> [178]. On the other hand, in 2022, Ray and coworkers proposed a new technique to synthesize CsPbX<sub>3</sub> (X=I/Br) by modifying ligand chemistry using olive oil [179].

For fabricating a relatively more stable cubic phase of CsPbX<sub>3</sub>, there are three methods: (1) nanoscale crystals with high surface energies (instead of high temperature), (2) surface ligands, and (3) composition engineering [40,116,177–179].

These methods are commonly utilized for synthesizing CsPbX<sub>3</sub> QDs. Hence, the colloidal CsPbX<sub>3</sub> NCs have several strong advantages compared to its bulk counterparts. First, based on quantum size and confinement effect, the energy bandgap of QD materials is easily tunable resulting in the full-color spectrum coverage. Second, the NC-ligand complexes can afford versatile solution processability via a colloidal structure. Third, the perovskite NCs can enhance their optical properties, resulting in a high photoluminescence quantum yield (PLQY) and a narrow full-width at half-maximum (FWHM) for color purity, which is desirable for lighting and display applications [168,177].

In this study, we tried to replace OA with OO to synthesize CsPbBr<sub>3</sub> NCs at room temperature for which we adopted the SR method. To the best of authors' knowledge, in the past, the OO ligand was tested only by the HI method [116] although OO is promising as a surface ligand for the mass-production process in future. Hence, in this work, we employed this OO ligand for synthesis of CsPbBr<sub>3</sub> NCs at room temperature. Note that SR is a type of ligand-assisted reprecipitation (LARP) technique, affording a simple, low cost, and a large production capability in ambient condition. Furthermore, basically, SR is an antisolvent-mediated solution process, resulting in the nucleation and growth of perovskite NCs. Hence, the classical LaMer model [180,181] and solvent engineering (SE) [182,183] should be very important for addressing the SR mechanism in the synthesis of CsPbBr<sub>3</sub> NCs at room temperature.

## 4.2. Materials and Methods

### 4.2.1. Chemicals

Lead bromide (PbBr<sub>2</sub>, 99.0%, AR chemicals), cesium bromide (CsBr, 99.9%, Sigma-Aldrich), oleic acid (OA, 98%, Sigma-Aldrich), oleylamine (OAm, technical grade 70%, Aldrich chemicals), olive oil (OO, Nice), hexane ( $\geq 97.5\%$ , Sigma-Aldrich), *N,N*-dimethylformamide (DMF, 99.5%, AR), and toluene (Aladdin,  $\geq 99.5\%$ , AR) were used in this experiments. All chemicals were used without further purification.

### 4.2.2. Synthesis of CsPbBr<sub>3</sub> Nanocrystals

In the SR method [177], the perovskite precursors and ligands, CsBr (0.2mmol, 43mg), PbBr<sub>2</sub> (0.2mmol, 73 mg), OA or OO (0.5 mL) and 0.25 mL of oleylamine, were dissolved

into 5 mL of a polar DMF solvent and stirred using magnetic stirrers at RT for two hours. Then, 1 mL of the perovskite precursor solution was titrated into 10 mL of a nonpolar toluene antisolvent and stirred for 60 sec. Then the CsPbBr<sub>3</sub> NC dispersion exhibited a green-light emission under 365 nm UV illuminations, confirming that the reaction was successful through the SR method. Then this colloidal dispersion was transferred to a centrifuge tube for centrifugations, and it was centrifuged at 8000 rpm for 10 min. The supernatant was discarded and the resulting precipitate was re-dispersed in the nonpolar hexane. Then the final CsPbBr<sub>3</sub> compound was dried under vacuum oven at 60°C for overnight. Now the CsPbBr<sub>3</sub> samples were kept for further characterization at RT.

#### 4.2.3. Characterization

The structural properties of CsPbBr<sub>3</sub> (OA & OAm) and CsPbBr<sub>3</sub> (OO & OAm) were determined by the X-ray diffraction (XRD) measurements measured using the Rigaku mini flex-300/600 diffractometer (Tokyo, Japan). The irradiation used CuK $\alpha$ ,  $\lambda = 1.5406 \text{ \AA}$  at 40 kV and 15 mA for the XRD analysis. The CsPbBr<sub>3</sub> NC's size and shape were determined by using the high-resolution transmission electron microscopy (HR-TEM) (Model: JEOL, JEM-2100) with an operating voltage of 200 kV. The optical absorption was characterized by using the Ultraviolet-visible (UV-vis) absorption spectroscopy (SHIMADZU UV-2600, Kyoto, Japan) whereas the photoluminescence (PL) spectra were measured using a spectrophotometer (SHIMADZU RF-6000, Kyoto, Japan) at the excitation wavelength of 375 nm. The Fourier-Transform infrared spectroscopy (FT-IR) analysis was performed by using PerkinElmer Spectrum Two FT-IR Spectrometer. For this purpose, the attenuated total reflection (ATR) was employed as a sampling technique to record the FT-IR spectra of the drop-cast CsPbBr<sub>3</sub> thin film in the range 4000-400cm<sup>-1</sup> with resolution of 4 cm<sup>-1</sup>. Here, for the drop-cast thin film, the glass substrate was washed in detergent soap, followed by ultrasonication using distilled water, acetone, and isopropanol, respectively, for 15 min per each process. Then the cleaned substrate was dried at 80°C for 1 hour in vacuum oven and subsequently cooled down at room temperature. The prepared sample solution (10 mg perovskite precursors in 1 mL of toluene) was drop cast on the clean glass substrate and dried in ambient condition. The PL decay curves were recorded by using a time-correlated single photon counting (TCSPC) (Model: Fluorolog 3 TCSPC, Horiba, USA).

#### 4.2.4. Computational Methods

The electronic band structures of the CsPbBr<sub>3</sub> unit cell were calculated using the Cambridge Serial Total Energy Package (CASTEP) software with the density functional theory. The Perdew-Burke-Ernzerhof (PBE) parametrization of the General Gradient Approximation (GGA) was used to describe the exchange correlation functional. The unit cell in the Brillouin zone was applied to evaluate the electronic band structures.

Energy of  $5 \times 10^{-5}$  eV/atom, maximum force of 0.01 eV/Å, maximum displacement of  $5 \times 10^{-4}$  Å and maximum stress of 0.02 GPa were used for all geometry optimization.

#### 4.3. Results and Discussion

Figure 4.1a shows the orthorhombic structure (space group, *Pbnm*) of CsPbBr<sub>3</sub> crystal. However, when temperature increased, CsPbBr<sub>3</sub> undergoes a phase transition from orthorhombic to tetragonal (*P4/mbm*) at 88°C and from tetragonal to cubic (*Pm $\bar{3}$ m*) at 130°C through a tiny rearrangement of the unit cell atoms [184,185]. On the other hand, in the case of NCs, the unit cell structure could be affected not only by crystal size/shape but also by the Pb<sup>2+</sup>/ligand ratio [161]. For example, the cubic phase was observed at RT if the crystal size is in nanoscale, indicating the metastable state of NCs. In the case of the electronic structures of CsPbBr<sub>3</sub> unit, the information could be found in the Figure (4.2), displaying that the bandgap ( $E_g$ ) is reduced with from 2.40 eV (cubic) to 2.31 eV (orthorhombic) via 2.37 eV (tetragonal).

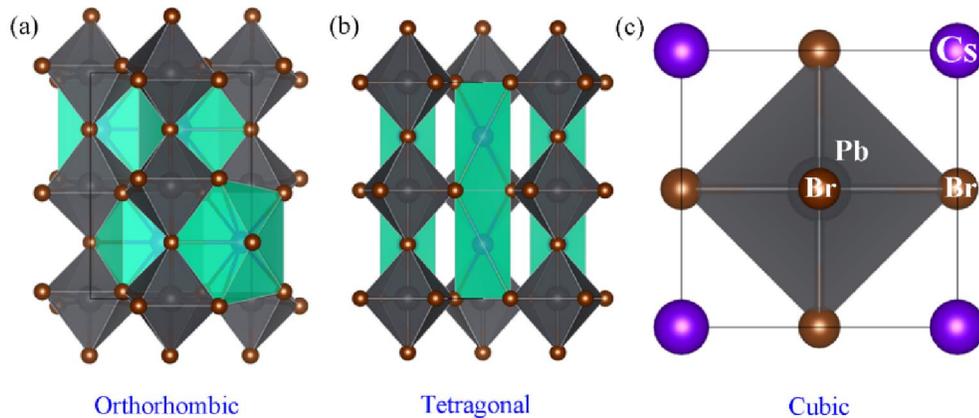


**Figure 4.1.** Polyhedral of CsPbBr<sub>3</sub> unit cell: (a) orthorhombic, (b) tetragonal, and (c) cubic structure

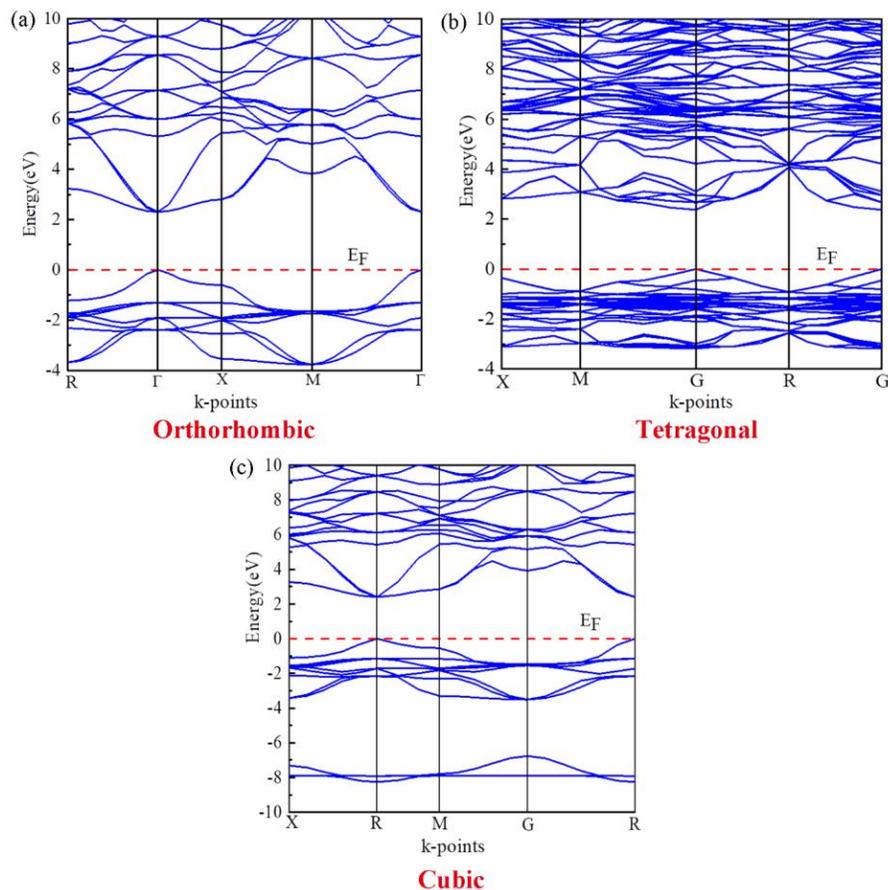
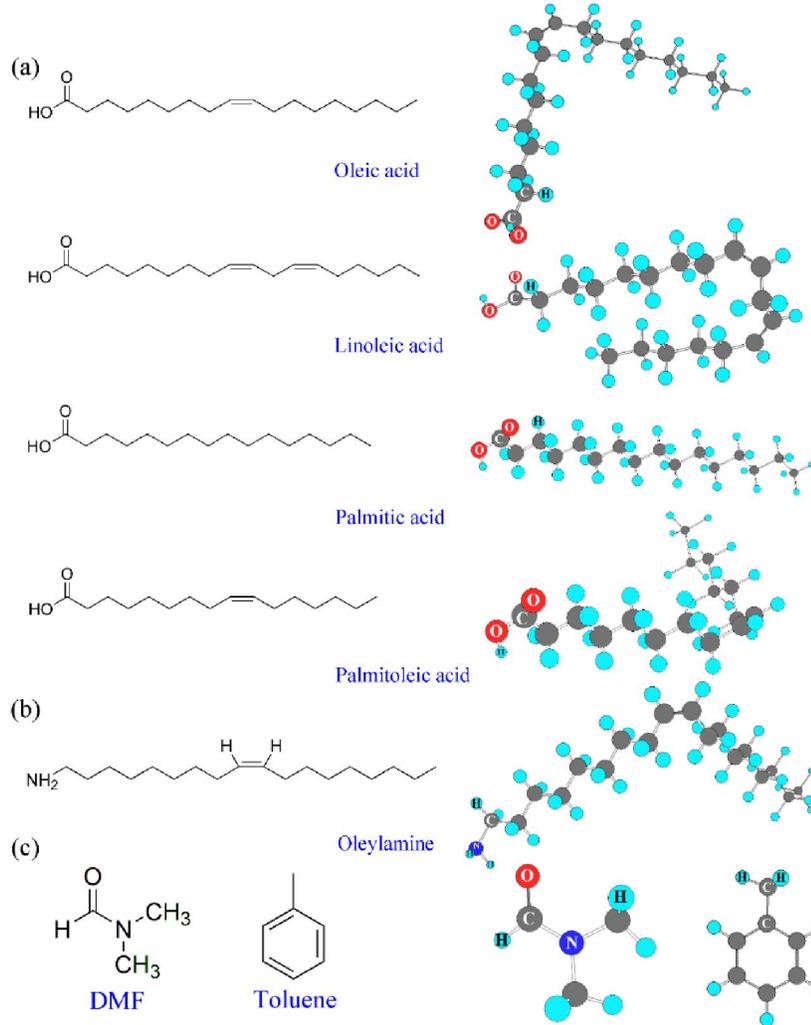


Figure 4.2. The electronic structures of CsPbBr<sub>3</sub> unit cells displaying polymorphism: (a) Orthorhombic, (b) tetragonal, and (c) cubic phase. Here, the bandgap energy ( $E_g$ ) of each *unit cell* is 2.31 eV for orthorhombic, 2.37 eV for tetragonal, and 2.40 eV for cubic phase, respectively.

Figure 4.3 shows the chemical structure of (a) OO, (b) OAm and (c) DMF and toluene, among which both organic OO and OAm surface ligands were employed as a mixed ligand for the synthesis of CsPbBr<sub>3</sub> at RT using a saturation recrystallization (SR) process [177]. As shown in Fig.4.3a, the OO's glycerol fractions (~98% of total OO) are composed of oleic acid, linoleic acid, palmitic acid, and palmitoleic acid but it also contains small amounts of non-glycerol fraction (~1-2% of the total OO by weight) such as biophenols and triterpenic acids[186]. Here because of the conformational freedom (e.g., a chain folding) of C-C single bond rotation, the high carbon ligand may undergo a chain folding in a typical solvent medium, DMF. Importantly, it is noteworthy that the compositional engineering (or mixing

strategy) has been commonly used for perovskite electronics for enhancing stability, e.g., cation mixtures ( $\text{MA}^+/\text{FA}^+$ ), metal ion mixtures ( $\text{Pb}^{2+}/\text{Sn}^{2+}$  or  $\text{Ge}^{2+}/\text{Sn}^{2+}$ ), halogen mixtures ( $\text{Cl}^-/\text{Br}^-/\text{I}^-$ ), perovskite mixtures (2D/3D), etc., which resulting in the enhancement of stability of materials and devices [186–190]. In the same vein, when we use the edible OO as a surface ligand, it might be useful in stability with a guaranteed benefit of eco-friendliness, which is a desirable characteristic for a mass-production process in future.



**Figure 4.3.** Chemical structures of (a) olive oil: glycerol fractions, ~98%, (b) oleylamine, and (c) DMF and toluene

Figure 4.4 shows the free energy change ( $\Delta G$ ) as a function of the radius ( $r$ ) when the nucleus is assumed to be a spherical according to the LaMer model, a classical nucleation theory [180,181].

Here, the free energy change ( $\Delta G_{hom}$ ) for homogenous and that ( $\Delta G_{het}$ ) for heterogeneous nucleation could be defined as follows,

$$\Delta G_{hom} = -\frac{4}{3}\pi r^3 \Delta G_v + 4\pi r^2 \gamma_{SL} \quad (4.1)$$

$$\Delta G_{het} = \left\{ -\frac{4}{3}\pi r^3 \Delta G_v + 4\pi r^2 \gamma_{SL} \right\} \cdot \frac{(2 + \cos \theta)(1 - \cos \theta)^2}{4} \quad (4.2)$$

where  $\Delta G_v$  is the free energy change associated with the formation of a small volume of solid whereas  $\gamma_{SL}$  is the solid/liquid interfacial free energy. Furthermore,  $\Delta G_{het} = \Delta G_{hom} \cdot S(\theta)$ , where  $S(\theta) = (2 + \cos \theta)(1 - \cos \theta)^2 / 4$  is a shape factor at a wetting angle  $\theta$ . According to the LaMer model [181], when a solution is supersaturated by undercooling, a nucleus could be formed. If this nucleus is larger than the critical size ( $r^*$ ), the spontaneous growth is available because  $\Delta G$  is decreasing as shown in Fig. 4.3a (see the blue solid line). In the case of the SR process, a supersaturated condition is directly available when the perovskite precursor solution (a colloidal dispersion containing bromide plumbate,  $\text{PbBr}_n^{2-n}$  with  $n=2-6$ ) is dropped into the antisolvent medium, e.g., toluene with Gutmann's number ( $D_N$ ),  $\sim 0.1$  kcal/mol (i.e., Lewis basicity) (see Table 1 for details) [191]. Here, it is noteworthy that a nonpolar toluene with solubility parameter,  $\delta = 8.9$  (cal/cm<sup>3</sup>)<sup>1/2</sup> is antisolvent for the bromide plumbate but it is still miscible with the polar DMF solvent ( $\delta = 12.1$  (cal/cm<sup>3</sup>)<sup>1/2</sup>) [192], indicating that the perovskite precursor ions ( $\text{Cs}^+$ ,  $\text{Pb}^{2+}$ ,  $\text{Br}^-$ ) will be directly exposed to the antisolvent toluene molecules, resulting in the nucleation and growth of perovskite NCs as explained through the critical point ( $r^* - \Delta G^*$ ) in the LaMer model. However, it is notable that in the case of SR process, the supersaturation has reached simply by adding the precursor solution into the antisolvent (not by undercooling like in the LaMer model).

Interestingly, the SR process is similar to the well-known *Solvent Engineering* (SE) (i.e., one-step antisolvent method) in the sense that the wet precursor solution is directly exposed to the antisolvent molecules [182,183].

However, the difference is that the SE method is processed during the spin-coating step by dispensing the antisolvent on the top of a wet precursor solution. Furthermore, SE allows the

formation of intermediate phase when a polar solvent DMSO is employed, whereas SR may not allow it because the colloidal dispersion may undergo a direct crystallization (at least without a co-solvent such as DMSO). Importantly, the SR process corresponds to the heterogeneous nucleation and growth of CsPbBr<sub>3</sub> perovskite because the nanoscale crystallization has processed through the surface of haloplumbate dispersed in the DMF medium. Recall that the perovskite precursor solution is a typical colloidal dispersion [193], i.e., haloplumbate is dispersed in a solvent medium, herein DMF with  $D_N = 26.6$  kcal/mol. In the case of Br<sup>-</sup>, its  $D_N$  is 33.7 kcal/mol [194], indicating that Pb<sup>2+</sup> (Lewis acid) may have a stronger coordination bonding with Br<sup>-</sup> ions (Lewis base) than DMF to form the acid-base adducts in spite that DMF is a good solvent for the perovskite precursor materials. See Figure 4.4 in SM for the vials containing CsPbBr<sub>3</sub> NCs in the supersaturated solution/dispersion.

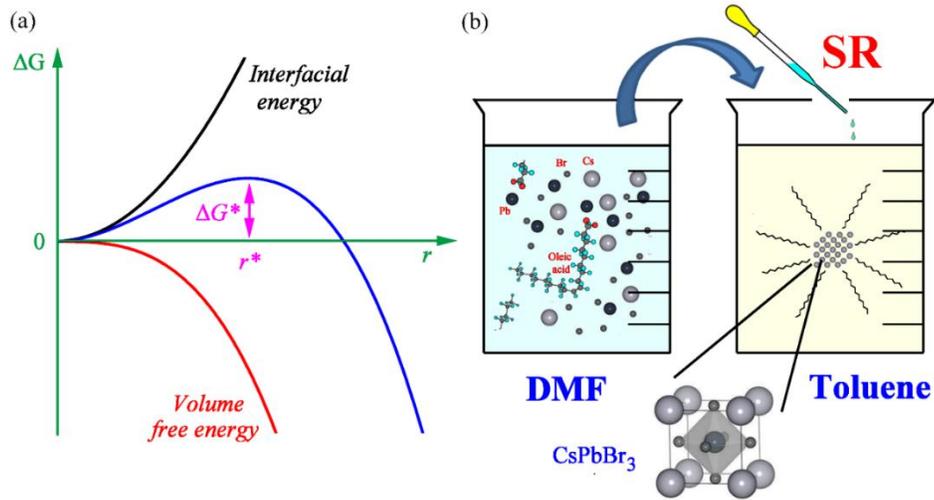


**Figure 4.4** (a) The free energy change ( $\Delta G$ ) in the nucleation and growth process as a function of  $r$  (a radius of a spherical nucleus by assumption). Here,  $\Delta G^*$  is the critical free energy barrier at the critical radius ( $r^*$ ), where a unit cell is formed. (b) Schematic explanation of supersaturated recrystallization (SR) of CsPbBr<sub>3</sub> in the antisolvent toluene.

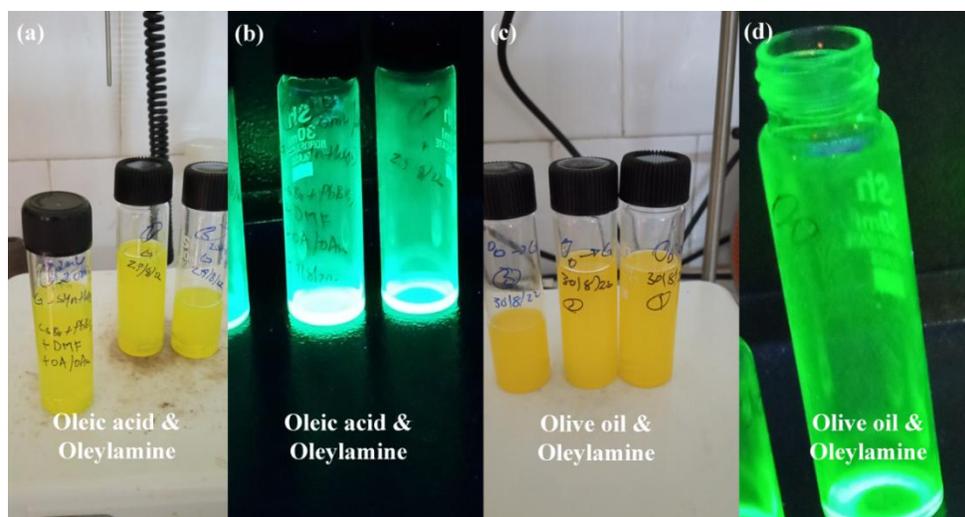


Figure 4.5. Vials containing a CsPbBr<sub>3</sub> colloidal dispersion depending on surface ligands: (a) oleic acid and oleylamine – a normal photo, (b) oleic acid and oleylamine – under 365 nm UV light, (c) olive oil and oleylamine – a normal photo, and (d) olive oil and oleylamine – under 365 nm UV light. Hence, CsPbBr<sub>3</sub> nanocrystals can serve as a green-light emitter.

**Table 4.1.** Gutmann’s solvent donor number ( $D_N$ ), solubility parameter ( $\delta$ ), dielectric constant ( $\epsilon$ ), molar mass, density, boiling point (b.p.) and chemical structures of solvents.

Solvent	$D_N$ (kcal/mol)	$\delta^1$ (cal/cm <sup>3</sup> ) <sup>1/2</sup>	$\epsilon$	Molar mass (g/mol)	Density (g/cm <sup>3</sup> )	b.p. (°C)	Chemical Structure
DMF	26.6	12.1	36.1	70.095	0.948	153	C <sub>3</sub> H <sub>7</sub> NO
Toluene	0.1	8.9	2.38	92.140	0.867	111	C <sub>6</sub> H <sub>5</sub> CH <sub>3</sub>

<sup>1</sup> In MKS unit, the  $\delta$  value is 24.8 MPa<sup>1/2</sup> for DMF and 18.2 MPa<sup>1/2</sup> for toluene, respectively.

Figures 4.6a and b show the experimental XRD patterns for the drop-cast CsPbBr<sub>3</sub> thin film on the glass substrate depending on the surface ligand species: (a) OA & OAm and (b) OO & OAm, whereas Figures 4.6c and d shows the XRD patterns for (c) cubic and (d) orthorhombic based on *Joint Committee on Powder Diffraction Standards* (JCPDS). As shown in Figures 4a-c, the location of XRD peaks such as (100), (110) and (200) are more corresponding to that of cubic (JCPDS: PDF#96-153-0682: space group  $Pm\bar{3}m$ ) instead of orthorhombic in spite that it was synthesized at RT [157,179,195,196].

Note that the lattice constant is 5.6050 Å based on the above JCPDS data, which was confirmed by the  $d$ -spacing of  $\sim 5.478$  or 5.418 Å =  $\lambda/(2 \cdot \sin\theta)$  at  $\theta = 8.08^\circ$  (OA) or  $8.17^\circ$  (OO),

respectively, when the x-ray wavelength ( $\lambda$ ) is 1.5406 Å. Probability, the CsPbBr<sub>3</sub> NC may prefer to exist in cubic phase due to its high surface energy and capping ligand effects. Furthermore, all the drop-cast CsPbBr<sub>3</sub> nanocrystalline thin films on the glass substrate display two intense peaks at  $2\theta= 16^\circ$  and  $32^\circ$ , corresponding to (100) and (200) crystallographic planes, indicating that there is orientational order to the [100] direction. However, when the OO & OAm ligands were incorporated as a ligand system for CsPbBr<sub>3</sub>, the additional (110) peak is clearly observed, indicating that the mixed ligand system by OO's glycerol fraction makes the orientational order be reduced, resulting in a partial amorphous halo [see the base-line shape centered around (110) peak]. However, when we estimated the crystallite size (D) by Scherrer equation (eqn.4.3), it was ranged of ~40-42 nm for all the samples (Table4. 2).

$$D = \frac{0.9 \cdot \lambda}{\beta \cdot \cos \theta} \quad (4.3)$$

where  $\lambda$  (= 0.154 nm) is the x-ray wavelength and  $\beta$  is the full width at half maximum (FWHM) at the angle  $\theta$ .

This single crystal's estimated crystallite size is a direct measurement of its nanoscale particle size, which is interesting in this case and will be covered in more detail in the section that follows.

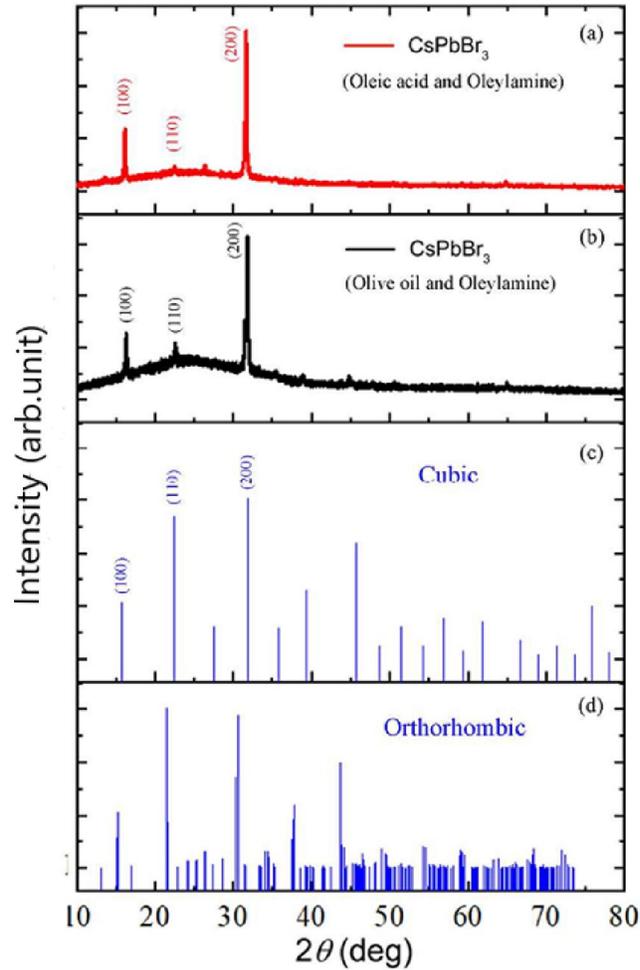
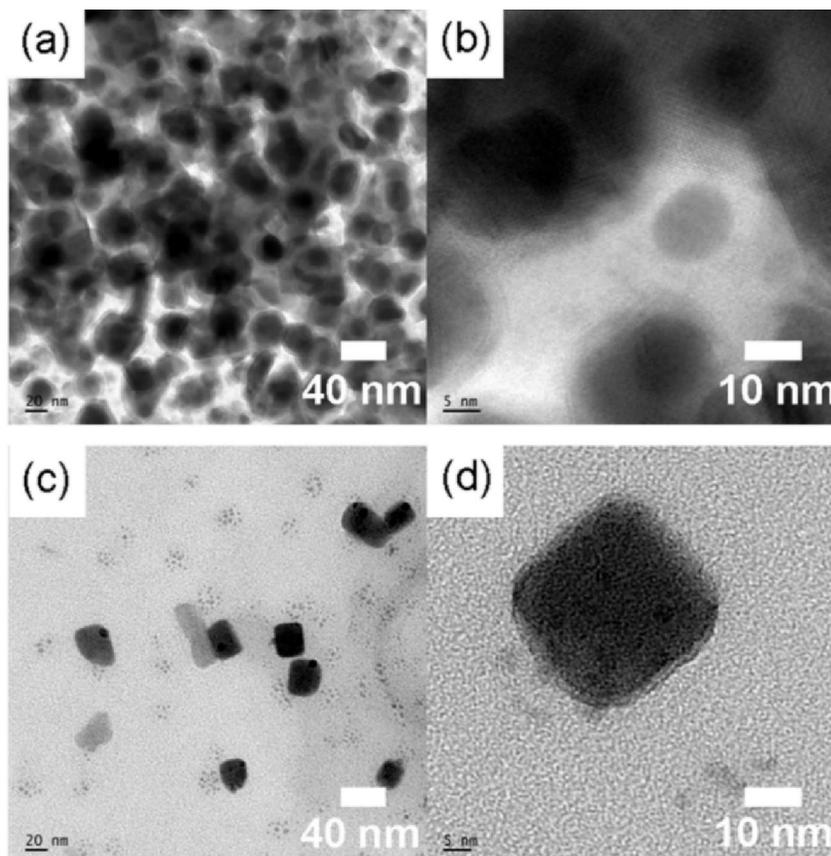


**Figure 4.6.** XRD patterns of CsPbBr<sub>3</sub> nanocrystal drop-cast thin film depending on the ligand species: (a) oleic acid and oleylamine and (b) olive oil and oleylamine. (c) Joint Committee on Powder Diffraction Standards (JCPDS) (PDF#96-153-0682) and (d) JCPDS (PDF#96-153-3063).

**Table 4.2.** Crystallite size ( $D$ ) of CsPbBr<sub>3</sub> at the (200) crystallographic plane. Here,  $\beta$  denotes a full width at half maximum (FWHM).

		CsPbBr <sub>3</sub> Nanocrystals				
	Crystal Planes	$2\theta$ (°)	$\theta$ (°)	$\beta$ (radian)	$D$ (nm)	
Oleic Acid (OA)	(100)	16.15	8.08	0.003323	42	
	(200)	31.65	15.83	0.003641	40	
Olive Oil (OO)	(100)	16.33	8.17	0.003438	41	
	(200)	31.80	15.90	0.003438	42	

Figure 4.7 shows HR-TEM images for CsPbBr<sub>3</sub> depending on the surface ligand system. Figures 4.7a and b are for the case of OA and OAm, whereas Figures 7c and d are for the case of OO and OAm. As shown in Figure 5, the TEM images show roughly a nano cubic, which is in line with the XRD data exhibiting the cubic structure.



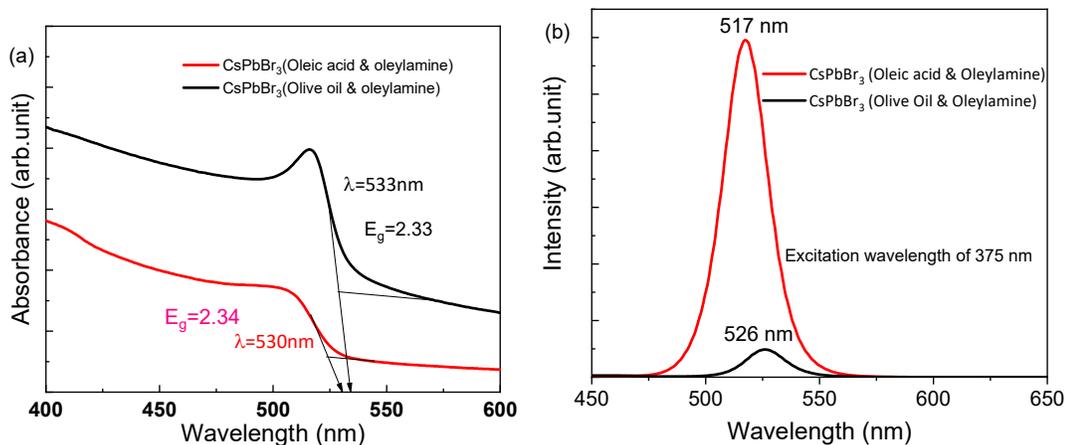
**Figure 4. 7.** HR-TEM images of CsPbBr<sub>3</sub> nanocrystals (nano cubic) when the ligand was oleic acid & oleylamine (a and b) and olive oil & oleylamine (c and d).

Figure 4.8 shows (a) the UV-vis absorption and (b) the PL emission spectra for the two different colloidal dispersions containing CsPbBr<sub>3</sub> NCs depending on the ligand species. Here it is noteworthy that the CsPbBr<sub>3</sub> perovskite is a direct semiconductor. In addition, the synthesized CsPbBr<sub>3</sub> NCs do not display any grain boundary in Fig.4.7, indicating a single crystalline nature in nanoscale although there might be some surface defects. Therefore, the CsPbBr<sub>3</sub> NCs are different from the disordered conjugated polymers showing a localized state. For disordered system, Mott defined a mobility edge between localized and delocalized states [197]. However, in this CsPbBr<sub>3</sub> NC, the sharp absorption edge is expected, affording

the decision of optical bandgap by using a simple tangential slope based on the equation,  $E = hc/\lambda$ , where  $E$  is energy,  $h$  is Planck's constant,  $c$  is the speed of light and  $\lambda$  is the wavelength of light. Therefore, according to the UV-Vis absorption edge (530 nm vs 533 nm) in Fig. 6a, the corresponding optical bandgap ( $E_g$ ) is 2.34 eV = 1240/530 (for OA & OAm) and 2.33 eV = 1240/533 (for OO & OAm), respectively. See Eqn. 4.4 for the conversion factor, 1240, between the energy (bandgap) and the wavelength (absorption edge).

$$\lambda [nm] = \frac{hc}{E} = \frac{(6.62607 \times 10^{-34} J \cdot s) \times (3 \times 10^8 m/s) (10^{-9} nm/m)}{E_g (eV) \times (1.60218 \times 10^{-19} J/eV)} = 1240 \frac{1}{E [eV]} \quad (4.4)$$

The result indicates that the nanoparticle size might be slightly larger in CsPbBr<sub>3</sub> synthesized with OO & OAm. This result is in line with the estimated crystallite size trend according to the sharpest peak at the (200) crystallographic plane in Fig.4.6a and Table 4.2. On the other hand, the PL spectra exhibit the PL peak at 517 nm for CsPbBr<sub>3</sub> with oleic acid & oleylamine and at 526 nm for CsPbBr<sub>3</sub> with OO & OAm. Here, the shift of PL peak from 517 nm to 526 nm (i.e., a red shift) indicates that the effective crystal size (or aggregation) of CsPbBr<sub>3</sub> NCs is slightly larger in the colloidal dispersion state when OO & OAm were employed as the surface ligands although the apparent size (Table 4.2) is similar in the solid-state in both ligand systems. Furthermore, it is believed that the surface state of NCs is different depending on the NC-ligand complexations. Hence, when OO & OAm were complexed with CsPbBr<sub>3</sub> NCs, there might be more surface defects, resulting in more non-radiative recombination, i.e., smaller PL intensity in Fig. 8b. Furthermore, FWHM is 21 nm for the former, but 19 nm for the latter. According to our finding, the narrow emission spectra were obtained below 25 nm, which falls in the required range of 12-42 nm [40] for the optoelectronic applications such as lighting and display technology.



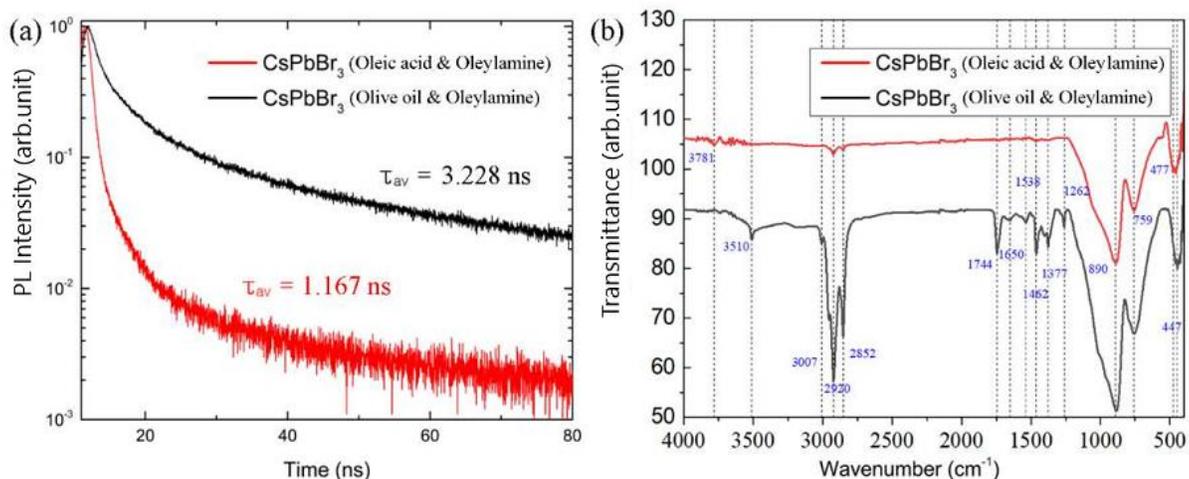
**Figure 4.8.** (a) UV-Vis absorbance spectra of the CsPbBr<sub>3</sub> nanocrystal dispersion depending on the ligand species. Here,  $\lambda = 530$  nm corresponds to  $E_g \approx 2.34$  eV (oleic acid & oleylamine) and  $\lambda = 533$  nm corresponds to  $E_g \approx 2.33$  eV (olive oil & oleylamine). (b) PL spectra of CsPbBr<sub>3</sub> nanocrystals depending on the ligand species. (c) optical bandgap of CsPbBr<sub>3</sub> nanocrystals by Tauc plot depending on the ligand species.

Figure 4.9a shows PL decay curve for the colloidal CsPbBr<sub>3</sub> NC dispersion as a function of ligand species. The average life time of electron-hole pairs (Wannier-Mott excitons) is 1.167 ns for CsPbBr<sub>3</sub> with OA & OAm whereas it is 3.228 ns for CsPbBr<sub>3</sub> with OO & OAm, indicating that a slightly larger CsPbBr<sub>3</sub> with OO & OAm displays a longer life time of excitons.

Figure 4.9b shows the FT-IR spectra for the drop-cast CsPbBr<sub>3</sub> nanocrystalline thin film. First of all, the IR spectrum for CsPbBr<sub>3</sub> with OA & OAm is relatively simpler than that for CsPbBr<sub>3</sub> with OO & OAm. Second, the FT-IR spectrum for OO & OAm shows a high absorption at 3020-2850 cm<sup>-1</sup> whereas the corresponding spectrum for OA & OAm is very weak at those wavenumbers, which correspond to the symmetric and asymmetric C-H stretching modes [116,178]. The functional groups of other organic components can be attributed to the absorption peaks at 3781 cm<sup>-1</sup> [178], and 3510 cm<sup>-1</sup> [116], which originates from the N-H<sub>2</sub> characteristic absorption of CsPbBr<sub>3</sub> prepared with the OO surface ligand. The IR peaks at around 1800-1600 cm<sup>-1</sup> are related to carbonyl (C=O) mode of stretching vibration which can be shift to lower wavenumber due to any perturbation. The shift of wavenumber may be ascribed to the presence of hydrogen bonding. The peaks at 1538 cm<sup>-1</sup>

and  $1462\text{ cm}^{-1}$  are related to C-CH<sub>3</sub>, associated with asymmetric bending, whereas those at  $1377\text{ cm}^{-1}$  and  $1262\text{ cm}^{-1}$  correspond to C-CH<sub>3</sub> symmetric bending (umbrella mode) vibration, C-N stretching vibration, respectively.

Absorption peaks ranged in  $1000\text{-}500\text{ cm}^{-1}$  indicate that the existence of aromatic bending vibrations [198], which might originate from OO components, trapped toluene (C<sub>6</sub>H<sub>5</sub>CH<sub>3</sub>) and/or aromatic impurities in samples. The peak at  $477\text{-}447\text{ cm}^{-1}$  is associated with N-H vibration (amines) [199].



**Figure 4.9.** (a) PL spectra decay of CsPbBr<sub>3</sub> nanocrystals depending on the ligand species. (b) FT-IR spectra of CsPbBr<sub>3</sub> nanocrystals depending on the ligand species.

#### 4. 4. Conclusions

In this work, we demonstrated the usefulness of olive oil and oleylamine as the surface ligand system (vs. the typical oleic acid and oleylamine mixtures) for the synthesis of CsPbBr<sub>3</sub> nanocrystals at room temperature. For this purpose, the supersaturated recrystallization process was employed, enabling a direct synthesis of perovskite nanocrystals. First, according to XRD, the crystallite size is  $\sim 40\text{-}42\text{ nm}$  in both conditions (oleic acid & oleylamine vs. olive oil & oleylamine) whereas the latter system allows a less orientational order than the former by showing a partial amorphous halo.

The TEM images confirmed that the CsPbBr<sub>3</sub> nanocrystals have a cuboid shape in line with XRD data exhibiting a cubic phase. The UV-Vis absorption data exhibited that the optical bandgap of CsPbBr<sub>3</sub> is about 2.3 eV in both ligand systems. The PL emission spectra indicated that FWHM is about 19 nm (olive oil & oleylamine) vs. 21 nm (oleic acid & oleylamine), which falls into the desirable FWHM values, i.e., ~12-42 nm, which is the suggested value for practical applications. Finally, the average PL life time is 3.228 ns for olive oil & oleylamine and 1.167 ns for oleic acid & oleylamine. Future work may include the application of CsPbBr<sub>3</sub> nanocrystals to the biosensors and optoelectronic devices.

## Chapter Five

### 5. Conjugated Polymer–Perovskite Quantum Dot (MDMO-PPV:CsPbBr<sub>3</sub>) Nanocomposites: Miscibility, Nano-Structures and Properties

#### 5.1. Introduction

Since  $\pi$ -bonded macromolecules were discovered in the 1970s, they have served as semiconductor and metallic conductors depending on the doping level for applications in organic electronics and optoelectronics such as light-emitting diodes (LEDs), lasers, electrochemical cells, photovoltaic (PV) cells, photodetectors, field-effect transistors (FETs), and others[200,201]. Currently, organic LED (OLED) has been commercialized and widely utilized in television, notebook monitors, smartphone screens, and wearable watches, to which the fundamental physics of organic semiconductors has tremendously contributed [202].

In this backdrop, in 2009, another unconventional semiconductor called organometallic halide perovskite (e.g., CH<sub>3</sub>NH<sub>3</sub>PbI<sub>3</sub>) has been introduced in the emerging PV technologies[36]. Then, through technical innovation, the quantum efficiency has reached more than 26% in PV cells and 20% in LED, shining a green light for mass production in the near future. However, organic-inorganic hybrid perovskite has drawbacks in stability[142,145]. Hence, to overcome this disadvantage, all-inorganic perovskite such as cesium lead halide have been studied in the field of perovskite electronics. For example, in 2015, Kovalenko and coworkers synthesized CsPbX<sub>3</sub> (X= Cl, Br, and I) quantum dots (QD) for the first time using a hot injection (HI) method[40]. Then in 2016, Zeng and coworkers invented another QD synthesis method at room temperature which is called supersaturated recrystallization (SR) [177]. Here, these QD perovskite materials demonstrated several advantages such as narrow full width at half maximum (FWHM), tunable band gap, high light absorption coefficient, low carrier recombination rate, high defect tolerance, high photoluminescence quantum yield (PLQY), and high synthesis feasibility [40,177]. However, they are vulnerable to moisture, oxygen, thermal stress, and light [42]. Hence, to improve these weak points, the surface of perovskite QD materials has been modified, and/or they were mixed with semiconducting or insulating plastic with better stability[44].

In Polymer Science, the polymer-polymer miscibility is an important topic. This is because by controlling the concentration of constituents in a blend or alloy, the resulting blends can provide a new set of properties that does not exist in a single polymer [203]. Similarly, conjugated polymer-perovskite composites have been explored to find out the new properties by combining these two materials. For example, polymer usually has a better film-forming property whereas perovskite has superior optoelectronic characteristics. In 2015, Masi *et al.* investigated that the polymer-perovskite innovative nanocomposite composed of poly[2-methoxy-5-(2-ethylhexyloxy)-1,4-phenylene vinylene] (MEH-PPV) and  $\text{CH}_3\text{NH}_3\text{PbI}_3$ , resulting in a power conversion efficiency, 3% [109]. Then, in 2017, Yang and coworkers demonstrated for the first time high-brightness white LEDs by blending MEH-PPV and blue-emission  $\text{CsPbBr}_x\text{Cl}_{3-x}$  nanocrystals [87]. In the same year, Aleshin *et al.* studied FET with a channel layer composed of poly[9,9-bis-(2-ethylhexyl)-9H-fluorene-2,7-diyl] (PFO)/ $\text{CsPbI}_3$  composites, resulting in a hole mobility of  $\sim 1.9\text{--}2.4 \times 10^{-1} \text{ cm}^2\text{V}^{-1}\text{sec}^{-1}$  at 300 K [204]. In 2018, Perulli *et al.* demonstrated a full color tunability based on the binary polymer-perovskite composite by combining  $\text{CsPbX}_3$  nanocrystals with poly(9,9-dioctylfluorene-*alt*-benzothiadiazole) (F8BT, yellow emitting) or poly(9,9-di-*n*-octylfluorenyl-2,7-diyl) (PFO, blue emitting) [74]. In 2018, Chikalova-Luzina *et al.* studied the MEH-PPV– $\text{CsPbBr}_3$  composite with enhanced processibility and stability, but observed a decrease in PL compared with MEH-PPV [110].

In 2020, Aleshin and coworkers observed high hole mobility ( $9 \text{ cm}^2\text{V}^{-1}\text{sec}^{-1}$ ) from the MEH-PPV/ $\text{CsPbBr}_3$  composite-based light-emitting FET, which is two-order better than the electron mobility ( $2.7 \times 10^{-2} \text{ cm}^2\text{V}^{-1}\text{sec}^{-1}$ ) in  $\text{CsPbBr}_3$ -based FET [205]. In the same year, Qaid and coworkers demonstrated improved morphology in the PFO– $\text{CsPbBr}_3$  composite exhibiting the non-radiative Förster resonance energy transfers (FRETs) from PFO to  $\text{CsPbBr}_3$  QDs [44]. In the case of Al-Asbahi and coworkers, they expanded it to the ternary PFO– $\text{CsPbBr}_3$ –MEH-PPV system, and observed the dual FRET from PFO to both  $\text{CsPbBr}_3$  QDs and MEH-PPV [117]. Recently, Anni and coworkers have studied the F8BT: $\text{CsPbI}_{1.5}\text{Br}_{1.5}$  system, and emphasized the charge transfer mechanism rather than FRET between F8BT and  $\text{CsPbI}_{1.5}\text{Br}_{1.5}$  [206]. Interestingly, Wu *et al.* also observed charge transfer in the poly[2-methoxy-5-(3',7'-dimethyloctyloxy)-1,4-phenylenevinylene] (MDMO-PPV):  $\text{Cs}_2\text{NaIn}_{0.75}\text{Bi}_{0.25}\text{Cl}_6$  (Mn doped) double perovskite composites [207].

In this study, we investigated the red-light-emitting MDMO-PPV–CsPbBr<sub>3</sub> QD complexed with ligand (oleic acid and oleylamine) composites. Here, MDMO-PPV polymer has its highest occupied molecular orbital (HOMO = -5.4 eV) and lowest unoccupied orbital (LUMO = -3.2 eV) whereas the typical light-emitting MEH-PPV polymer has HOMO = -5.4 eV and LUMO -3.0 eV [208–210]. On the other hand, CsPbBr<sub>3</sub> QD has a valence band maximum (VBM = - 5.6 eV) and conduction band minimum (CBM = -3.3 eV) [211]. Hence, if we employ MDMO-PPV instead of MEH-PPV for the polymer-perovskite (CsPbBr<sub>3</sub>) system, the similar LUMO-CBM (i.e., -3.2 and -3.3 eV) may help FRET instead of charge transfer (quenching through the different electron affinity, reduction potential). Importantly, we analyzed the intermolecular interactions in MDMO-PPV–oleic acid, MDMO-PPV–oleylamine, and MDMO-PPV–toluene based on the original Flory-Huggins theory, a quasi chemical approach, with the group contribution method [212–218], which may provide insight for understanding the miscibility between components including processing solvent. Then we studied the morphological, structural, electrochemical, and optical properties of MDMO-PPV–CsPbBr<sub>3</sub> composite system. Specifically, in this work, we observed that MDMO-PPV–CsPbBr<sub>3</sub> composite displayed lower resistance in the electrochemical cell than the pure MDMO-PPV film, demonstrating the perovskite QD should be useful when used as a component for the MDMO-PPV–based composite.

## 5.2. Materials and Methods

### 5.2.1. Chemicals

Lead bromide (PbBr<sub>2</sub>, 99%, Delhi, AR chemicals, India), cesium bromide (CsBr, 99.9%, Sigma-Aldrich), oleic acid (98%, Sigma-Aldrich, Darmstadt, Germany), oleylamine (70%, Sigma-Aldrich), acetone (≥99.5%, Sigma-Aldrich), hexane (≥97.5%, Sigma-Aldrich), isopropanol (≥99.5%, Delhi, India), toluene (≥99.5%, AR chemicals, Delhi, India), *N,N*-dimethylformamide (DMF, 99.5%, AR chemicals), ethyl acetate (99%, AR chemicals, Delhi, India), poly[2-methoxy-5-(3',7'-dimethyloctyloxy)-1-4-phenylenevinylene](MDMO-PPV,  $M_n = 120,000 \text{ g}\cdot\text{mol}^{-1}$ , polydispersity index = 3.36, Sigma-Aldrich) were purchased and used as received without further purification.

### 5.2.2. Synthesis of CsPbBr<sub>3</sub> Quantum Dots

The synthesis was performed by following the experimental procedure [177,219]. Accordingly, CsBr (0.2 mmol, 43 mg), and PbBr<sub>2</sub> (0.2 mmol, 73 mg), were dissolved in 5 mL DMF. Then 0.5 mL oleic acid and 0.25 mL oleylamine were added into the perovskite precursor solution and vigorously stirred at room temperature for 120 min. Then, 1 mL of this perovskite precursor solution was injected into 10 mL of toluene. After injection of precursor solution, bright yellowish color was immediately observed. Then, the change a color in the solution was examined using the 365 nm ultraviolet (UV) illumination, resulting in green emission. Then the sample was mixed with CsPbBr<sub>3</sub>: ethyl acetate= 1:3 wt. ratios and centrifuged at 8000 rpm for 10 min. The resulting precipitate was re-dispersed in hexane and dried in a vacuum oven overnight at 60°C. Then, the sample was stored in a vial at room temperature.

### 5.2.3. Preparation of MDMO-PPV–CsPbBr<sub>3</sub> QD Composites

The MDMO-PPV in toluene solution (3mg·mL<sup>-1</sup>) was stirred overnight at 50°C. Then, equivalent CsPbBr<sub>3</sub> colloidal dispersion in toluene was mixed with the MDMO-PPV solution with desiring weight ratios, MDMO-PPV: CsPbBr<sub>3</sub>= 90:10, 80:20, 70:30, 60:40, and 50:50. After that, MDMO-PPV–CsPbBr<sub>3</sub> dispersions were further ultrasonicated for 45 min, and then additionally stirred for 1 hour. The resulting dispersion was used to fabricate the composite films (spin-coating at 3000 rpm or drop-casting) at room temperature.

### 5.2.4. Characterizations

Water Contact angles were measured using a contact angle analyzer (Phoenix 300+/LCA10, SEO Co. ltd., Korea), for which 76 µL of water was dropped on top of the spin-coated MDMO-PPV film. X-ray diffraction (XRD) patterns were obtained using the Rigaku mini flex-300/600 diffractometer (Rigaku, Tokyo, Japan). Scanning electron microscope (SEM) images were acquired using the field-emission SEM (FE-SEM, MAIA3 XMH, TESCAN BRONO SRO, Kohoutovice, Czech Republic). Transmission electron microscope (TEM) images as well as the selected area electron diffraction (SAED) patterns were obtained using the high resolution TEM (HR-TEM, Model: JEOL, JEM-2100, Peabody, MA, USA). Fourier transform infrared (FT-IR) spectra were analyzed using the PerkinElmer Spectrum

Two FTIR Spectrometer. Here, the attenuated total reflection (ATR) was employed as a sampling technique to record the FT-IR spectra of the samples in the range 4000–400  $\text{cm}^{-1}$  with a resolution of 4  $\text{cm}^{-1}$ . The electrochemical impedance spectroscopy (EIS) analysis was carried out using the SP-300 potentiostat/ galvanostat with an impedance analyzer (Bio-Logic, SAS, France) in the frequency range of 10 mHz to 100 KHz. For this purpose, glassy carbon electrode (GCE), platinum wire, and Ag/AgCl in 0.1M KCl were used as working electrode (WE), counter electrode (CE), and reference electrode (RE), respectively. The ultraviolet visible (UV–Vis) absorption spectra were recorded by using the UV–Vis/NIR Spectrophotometer (JASCO V-770, Japan). The photoluminescence (PL) emission spectra were obtained by the Cary Eclipse fluorescence spectrophotometer (scan rate 600 nm/min, MY18490002, Agilent Technologies, Malaysia) at an excitation wavelength of 380 nm for CsPbBr<sub>3</sub> and 450 nm for both MDMO-PPV and MDMO-PPV–CsPbBr<sub>3</sub> composites.

### **5.3. Results and Discussion**

Figure 5.1 shows the chemical and crystal structures of materials used in this work. MDMO-PPV (Fig.5.1a) is one of the well-known solution processable semiconducting polymers through alkoxy-side chain functionalization. Here, MDMO-PPV was mixed with the CsPbBr<sub>3</sub> QDs (Fig.5.1b) with the oleic acid and oleylamine ligands (Fig. 1c) using the toluene solvent (Fig.5. 1d).

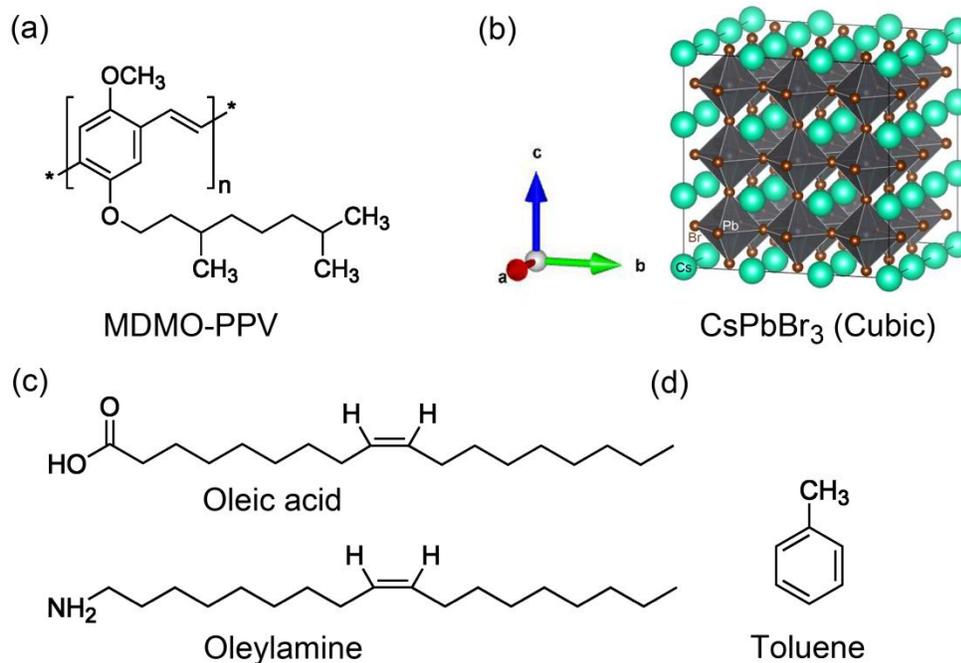


**Figure 5.1.** Structures of organic molecules and inorganic crystal: (a) MDMO-PPV; (b) 3×3×3 Supercell of CsPbBr<sub>3</sub>; (c) oleic acid and oleylamine; and (d) toluene.

The MDMO-PPV and CsPbBr<sub>3</sub> are not molecularly miscible because the latter forms nanoscale domains in the MDMO-PPV matrix. However, considering that CsPbBr<sub>3</sub> is complexed with the oleic acid and oleylamine ligands [220], it is interesting to study the interaction between the ligands and MDMO-PPV because they directly face each other in the resulting composites, e.g., MDMO-PPV/ligands-CsPbBr<sub>3</sub> QD nanocrystals. Hence, we investigate the phase behavior among the components (i.e., MDMO-PPV, oleic acid, oleylamine, and toluene), for which the Flory-Huggins lattice theory [212–214] was employed, providing insight into the interfacial interactions between MDMO-PPV and the surface ligands or solvent. To this end, the polymer-solvent (or oligomer-solvent) interaction parameter ( $\chi_{ij}$ ), as well as the relative molar volume ( $r_i$ ), should be calculated first because these two parameters largely govern the phase behavior of binary polymer (or oligomer) solutions according to the Flory-Huggins theory. Here the former could be estimated through the solubility parameter ( $\delta_i$  [cal<sup>1/2</sup> cm<sup>-3/2</sup>]) through the relationship  $\chi_{ij} = \hat{V}_1 (\delta_i - \delta_j)^2 / RT$  [214]. On the other hand, the latter could be calculated by dividing the molar mass with density. Here the subscript  $i$  or  $j$  indicated a component: when  $i$  or  $j = 1, 2, 3$ , and 4, it

denotes toluene, MDMO-PPV, oleic acid, and oleylamine, respectively. Moreover,  $\hat{V}_1$  is the molar volume of the solvent,  $R$  is the gas constant and  $T$  is temperature. In this study,  $\delta_2$  was estimated from the water contact angle information [214,215,221,222], whereas  $\delta_3$  and  $\delta_4$  were estimated through the group contribution method[217,218]. In the case of  $\delta_1$ , it is available in the literature report because toluene is a common solvent [223].

Figure 5.2 shows the water contact angle ( $\theta_c$ ) data for MDMO-PPV, displaying the average  $\theta_c = 82.8^\circ$ . Then using the Li and Neumann's equation,  $\cos \theta_c = -1 + 2\sqrt{\gamma_{sv}/\gamma_{lv}} \cdot \exp\left[-\bar{\beta}(\gamma_{lv} - \gamma_{sv})^2\right]$  based on Young's equation,  $\gamma_{lv} \cos \theta_c = \gamma_{sv} - \gamma_{sl}$ , we may calculate the  $\delta_2$  of MDMO-PPV from the empirical relation of  $\delta_2 [\text{cal}^{1/2}\text{cm}^{-3/2}] = 1.829058\sqrt{\gamma_{sv}}$  [221,222]. Here,  $\gamma_{lv}$ ,  $\gamma_{sv}$  and  $\gamma_{sl}$  are surface energies for liquid-vapor, solid-vapor, and solid-liquid, respectively, whereas the constant  $\bar{\beta}$  is  $0.000115 \text{ m}^4 \text{ mJ}^{-2}$ , and  $\gamma_{lv} = 72.8 \text{ mJ m}^{-2}$  for water [221]. Resultantly,  $\delta_2$  is estimated to be  $10.5 \text{ cal}^{1/2}\text{cm}^{-3/2}$  (see Table 1) by solving the Li and Neumann's equation using the Newton-Raphson method [214–216].

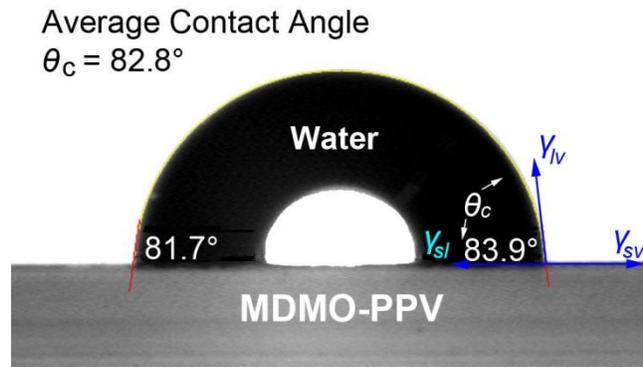


**Figure 5.2.** Water contact angle measurement on the spin-coated MDMO-PPV film. Here, the force balance among surface energies could be explained by Young's equation,  $\gamma_{lv} \cos \theta_c = \gamma_{sv} - \gamma_{sl}$ .

The solubility parameter can be divided into three parts depending on the types of interaction forces, *i.e.*,  $\delta = \sqrt{\delta_d^2 + \delta_p^2 + \delta_h^2}$ , in which  $\delta_d$ ,  $\delta_p$ , and  $\delta_h$  correspond to the contribution from dispersion force, polar force and hydrogen bonding, respectively [192,217]. Importantly, the group contribution method allows us to estimate the solubility parameter based on the structure-property relationship. For example, according to Hoftyzer and Van Krevelen, the solubility parameter components could be obtained using the following equations,  $\delta'_d = \sum \mathbf{F}_{di} / \hat{V}_i$ ,  $\delta'_p = \sqrt{\sum \mathbf{F}_{pi}^2} / \hat{V}_i$ , and  $\delta'_h = \sqrt{\sum \mathbf{E}_{hi}} / \hat{V}_i$ , in which  $\mathbf{F}_{di}$ ,  $\mathbf{F}_{pi}$ , and  $\mathbf{E}_{hi}$  are dispersion force, polar force and hydrogen bond energy, respectively[217,218]. Here it is notable that depending on the convention in theory, when the solubility-parameter symbol is expressed as  $\delta'$ , it has a unit of  $\text{MPa}^{1/2}$  or  $(\text{MJ m}^{-3})^{1/2}$ . Table 1 shows the solubility parameter component for each structural group from the oleic acid and oleylamine ligands. In the case of oleic acid,  $\delta'_d = \sum \mathbf{F}_{di} / \hat{V}_3 = 5130/316 = 16.234$ ,  $\delta'_p = \sqrt{\sum \mathbf{F}_{pi}^2} / \hat{V}_3 = 0$ , and  $\delta'_h = \sqrt{\sum \mathbf{E}_{hi}} / \hat{V}_3 = 0$  when  $\hat{V}_3 = 316 \text{ cm}^3 \text{ mol}^{-1}$ . Hence,  $\delta' = \sqrt{\delta_d'^2 + \delta_p'^2 + \delta_h'^2} = 16.234 \text{ MPa}^{1/2}$  and  $\delta_3 = \delta' / 2.049 \approx 7.9 \text{ cal}^{1/2} \text{ cm}^{-3/2}$ . In the case of oleylamine,  $\delta'_d = \sum \mathbf{F}_{di} / \hat{V}_4 = 5150/329 = 15.653$ ,  $\delta'_p = \sqrt{\sum \mathbf{F}_{pi}^2} / \hat{V}_4 = 0$ , and  $\delta'_h = \sqrt{\sum \mathbf{E}_{hi}} / \hat{V}_4 = \sqrt{8400/329} = 5.052$  when  $\hat{V}_4 = 329 \text{ cm}^3 \text{ mol}^{-1}$ . Hence,  $\delta' = \sqrt{\delta_d'^2 + \delta_p'^2 + \delta_h'^2} = 16.46 \text{ MPa}^{1/2}$  and  $\delta_4 = \delta' / 2.049 \approx 8.0$ .

**Table 5.1.** Solubility parameter of solvent, polymer, and ligands (oleic acid and oleylamine).

Molecule	$\delta'_i$ (MPa <sup>1/2</sup> )	$\delta_i$ (cal <sup>1/2</sup> cm <sup>-3/2</sup> )*	MW (g mol <sup>-1</sup> )	$\rho$ (g cm <sup>-3</sup> )	$V_i$ (cm <sup>3</sup> mol <sup>-1</sup> )	$r_i$ (-)
Toluene	18.24	8.9	92.14	0.870	105.9	1
MDMO-PPV	21.52	10.5	10,000-40,000*	0.910	10,881.4-43525.6*	102-410*
Oleic acid	16.39	7.9	282.47	0.895	315.6	3
Oleylamine	16.19	8.0	267.49	0.813	329.0	3

\* This parameter was used as a variable for the Flory-Huggins model.

**Table 5.2.** Solubility-parameter component group contributions (Hoftyzer-Van Krevelen method [217]) for oleic acid and oleylamine.

Molecule	Structural group	Number of group	$F_{di}$ (MJ m <sup>-3</sup> ) <sup>1/2</sup> mol <sup>-1</sup>	$F_{pi}$ (MJ m <sup>-3</sup> ) <sup>1/2</sup> mol <sup>-1</sup>	$E_{hi}$ J mol <sup>-1</sup>
Oleic acid	HOOC-	1	530	0	0
	CH <sub>2</sub>	14	270	0	0
	=C -H 	2	200	0	0
	-CH <sub>3</sub>	1	420	0	0
Oleylamine	NH <sub>2</sub>	1	280	0	8400
	CH <sub>2</sub>	15	270	0	0
	=C -H 	2	200	0	0
	-CH <sub>3</sub>	1	420	0	0

Now the Flory-Huggins interaction parameter could be calculated based on the solubility parameter information and the relative molar volume (see Tables 5.1 (5.2 to 5.3). For example, the MDMO-PPV–toluene system has  $\chi_{12} = \hat{V}_1 (\delta_1 - \delta_2)^2 / RT = 105.9 \cdot (10.5 - 8.9)^2 / (1.987 \cdot T) = 136.4 \text{ K/T}$ . The MDMO-PPV and oleic acid system has  $\chi_{23} = \hat{V}_1 (\delta_2 - \delta_3)^2 / RT = 105.9 \cdot (10.5 - 7.9)^2 / (1.987 \cdot T) = 360.3 \text{ K/T}$ . The MDMO-PPV and oleylamine system has  $\chi_{24} = \hat{V}_1 (\delta_2 - \delta_4)^2 / RT = 105.9 \cdot (10.5 - 8.0)^2 / (1.987 \cdot T) = 333.1 \text{ K/T}$ . The oleic acid and toluene system has  $\chi_{13} = \hat{V}_1 (\delta_1 - \delta_3)^2 / RT = 105.9 \cdot (8.9 - 7.9)^2 / (1.987 \cdot T) = 53.3 \text{ K/T}$ .

Finally, the oleylamine and toluene system has  $\chi_{14} = \hat{V}_1 (\delta_1 - \delta_4)^2 / RT = 105.9 \cdot (8.9 - 8.0)^2 / (1.987 \cdot T) = 43.2 \text{ K/T}$ . Here, there are two assumptions. First, we defined the lattice size based on the molar volume of toluene solvent. Second, we set  $M_n$  of MDMO-PPV to 10,000  $\text{g} \cdot \text{mol}^{-1}$  when calculating  $\chi_{12}$ ,  $\chi_{23}$ , and  $\chi_{24}$ . However, we separately studied the effect of  $M_n$  (10,000 to 40,000  $\text{g} \cdot \text{mol}^{-1}$ ) on the phase behavior of the MDMO-PPV–toluene system.

**Table 5.3.** Flory-Huggins interaction parameter for the binary system. Here, the components 1, 2, 3, and 4 correspond to toluene, MDMO-PPV ( $M_n = 10,000 \text{ g} \cdot \text{mol}^{-1}$ ), oleic acid, and oleylamine, respectively,

MDMO-PPV:		MDMO-PPV:		MDMO-PPV:		Oleic acid:	Oleylamine:
Toluene		Oleic acid		Oleylamine		Toluene	Toluene
$\chi_{12} = 136.4 \text{ K/T}$		$\chi_{23} = 360.3 \text{ K/T}$		$\chi_{24} = 333.1 \text{ K/T}$		$\chi_{13} = 53.3 \text{ K/T}$	$\chi_{14} = 43.2 \text{ K/T}$
$r_2 = 104, * r_1 = 1$		$r_2 = 104, r_3 = 3$		$r_2 = 104, r_4 = 3$		$r_3 = 3, r_1 = 1$	$r_4 = 3, r_1 = 1$

\* If MDMO-PPV has  $M_n$  of 20000, 30000, and 40000  $\text{g} \cdot \text{mol}^{-1}$ ,  $r_2$  will be 208, 311 and 415, respectively.

Table 5.3 shows the two essential parameter lists for calculating the phase diagrams of the binary polymer-solvent and oligomer-solvent systems. According to the Flory-Huggins theory[212–214], the Gibbs free energy of mixing ( $\Delta G_{mix}$ ) is given by

$$\frac{\Delta G_{mix}}{RT} = \frac{\phi_i}{r_i} \ln \phi_1 + \frac{\phi_j}{r_j} \ln \phi_2 + \chi_{ij} \phi_i \phi_j \quad (5.1)$$

where  $\phi_i$ ,  $\phi_j$ ,  $r_i$  ( $i=1$ , solvent), and  $r_j$  are the volume fraction and relatively molar volume of components  $i$  and  $j$ , respectively.

Then through the equilibrium between polymer-lean ( $\alpha$ ) and polymer-rich ( $\beta$ ) phases according to the below equations, we can calculate the temperature-composition binodal curve for the binary systems.

$$\Delta\mu_i^\alpha = \Delta\mu_i^\beta \quad (5.2)$$

$$\Delta\mu_j^\alpha = \Delta\mu_j^\beta \quad (5.3)$$

where  $\Delta\mu_i = \partial\Delta G_{mix}/\partial n_i$  and  $\Delta\mu_j = \partial\Delta G_{mix}/\partial n_j$  are the chemical potentials of component of  $i$  and  $j$ , respectively. Here, it is notable that the original Flory-Huggins theory can capture the phase behavior of polymer solutions *qualitatively*, indicating that we may understand the calculation results from relativistic point of view, *i.e.*, comparatively.

At 298 K (= 25 °C), the interaction parameters are  $\chi_{12}=0.46$  for MDMO-PPV–toluene,  $\chi_{23}=1.21$  for MDMO-PPV–oleic acid,  $\chi_{24}=1.12$  for MDMO-PPV–oleylamine,  $\chi_{13}=0.18$  for oleic acid–toluene,  $\chi_{14}=0.15$  for oleylamine–toluene. Hence, the results indicate that (1) both oleic acid–toluene and oleylamine–toluene systems are highly miscible at 298 K because  $\chi_{13}<0.5$  and  $\chi_{14}<0.5$ , (2) both MDMO-PPV–oleic acid and MDMO-PPV–oleylamine are immiscible at 298 K because  $\chi_{23}>0.5$  and  $\chi_{24}>0.5$ , indicating that the ligands cannot act as a compatibilizer for the MDMO-PPV–CsPbBr<sub>3</sub> system, (3) MDMO-PPV–oleic acid is more immiscible than MDMO-PPV–oleylamine because  $\chi_{23}>\chi_{24}>0.5$ , and finally, (4) MDMO-PPV–toluene is partially miscible because  $\chi_{12}\sim 0.5$ , indicating that MDMO-PPV can be soluble by increasing temperature more than 298 K where  $\chi_{12}<0.5$ .

Figure 5.3a shows the binodal curve for the binary MDMO-PPV–toluene system as a function of  $M_n$ . As shown in Figures 5.3a and b, if  $M_n$  increases, the critical temperature ( $T_c$ ) is shifted up, indicating that the two-phase region becomes large, *i.e.*, easy phase separation comparatively. Figure 5.3c displays the MDMO-PPV–ligand systems with the critical point larger than 1,000 K, indicating that MDMO-PPV is immiscible with the two ligands (oleic acid and oleylamine). However, it is notable that, of course, the binary system cannot reach a stable one-phase because the decomposition temperatures of two ligands are less than  $\sim 573$  K [223,224]. On the other hand, Figure 5.3d shows that oleic acid–toluene

and oleylamine-toluene exhibits the critical point at  $(\phi_{3,c}, T) = (0.37, 42.8\text{ K})$  and  $(0.37, 42.8\text{ K})$   $(0.37, 34.7\text{ K})$ , respectively, indicating that the ligand molecules are easily miscible with a solvent because they have similar solubility parameter, i.e., ‘*like dissolves like*’ (see Table 5.1).

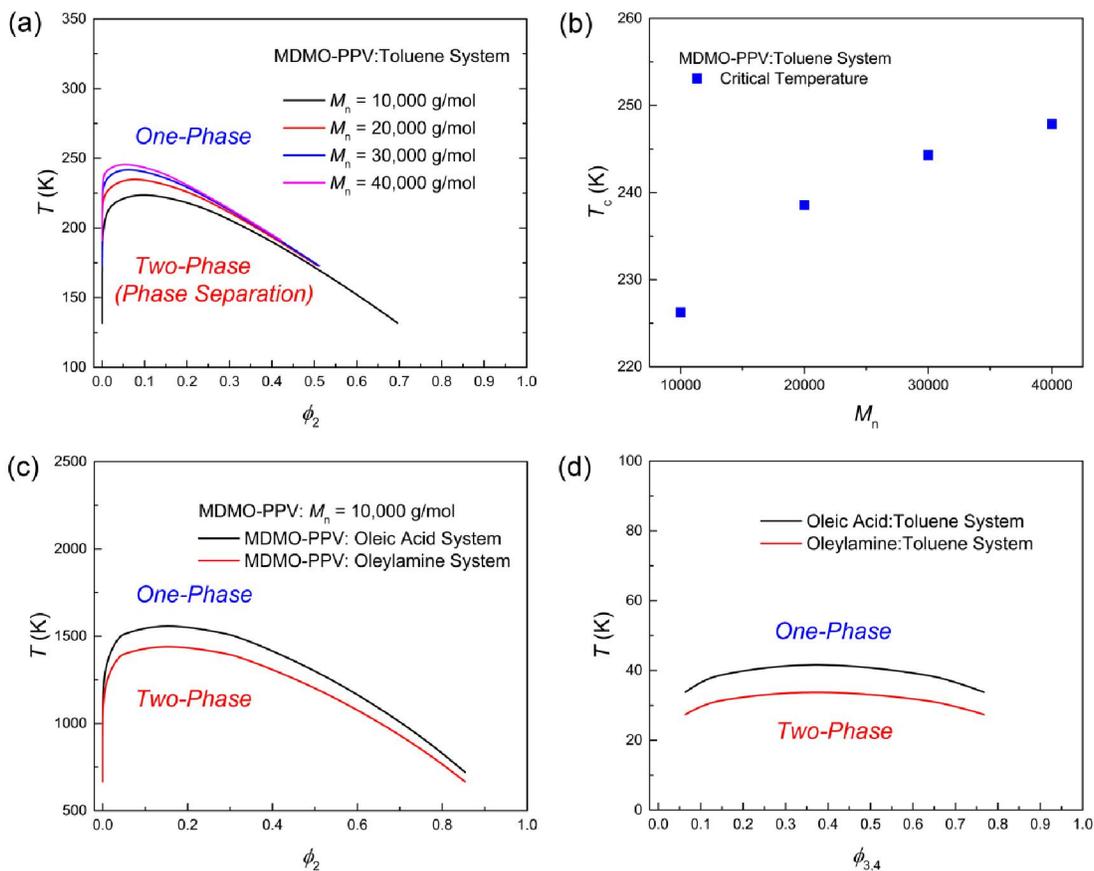


**Figure 5.3.** (a) Phase diagrams of the binary MDMO-PPV–toluene system as a function of molecular weight of MDMO-PPV. (b) The plot of the critical temperature vs. the number average molecular weight of MDMO-PPV. (c) Phase diagrams of the binary MDMO-PPV–oleic acid (black solid line) and MDMO-PPV–oleylamine (red solid line) system. (d) Phase diagrams of the binary oleic acid–toluene (black solid line) and oleylamine-toluene (red solid line) systems.

From the phase behavior, we come to know that MDMO-PPV is immiscible with the oleic acid and oleylamine ligand molecules. This theoretical prediction suggests that when

CsPbBr<sub>3</sub>-ligand complexes are mixed with MDMO-PPV, CsPbBr<sub>3</sub> nanocrystals could be easily aggregated because of the repulsion interaction between MDMO-PPV and the ligand molecules (oleic acid and oleylamine). With this information, the XRD patterns of the MDMO-PPV–CsPbBr<sub>3</sub> composite films were investigated. Figure 5.4a and b shows the XRD patterns of MDMO-PPV and CsPbBr<sub>3</sub> nanocrystals, respectively.

Figure 5.4 shows the XRD patterns of MDMO-PPV, CsPbBr<sub>3</sub> QD nanocrystals, and the MDMO-PPV–CsPbBr<sub>3</sub> composites. For this purpose, the drop-cast samples on a glass substrate were used. Figure 1a exhibits that MDMO-PPV is an amorphous material displaying a typical amorphous halo at  $2\theta \approx 26^\circ$  which may originate from the distributed  $\pi$ - $\pi$  stacking distance among MDMO-PPV chain molecules [225]. On the other hand, CsPbBr<sub>3</sub> nanocrystals show a well-organized cubic structure with (100) and (200) peaks at  $2\theta = 16.2^\circ$  and  $31.6^\circ$ , respectively. Here, the crystallite size (D) could be estimated using Scherrer's equation,  $t = 0.9\lambda/(\beta \cdot \cos \theta)$ , in which  $\lambda$  is the wavelength of x-ray,  $\beta$  is full width at half maximum (FWHM) at the angle  $\theta$  [44,226]. Accordingly, D is about 38 nm =  $0.9 \times 0.154 / [0.003672 \times \cos(15.8)]$ . However, when we made MDMO-PPV–CsPbBr<sub>3</sub> composites with the ratios of 90:10, 80:20, 70:30, 60:40, and 50:50, the corresponding D data were 33 nm, 42 nm, 48 nm, 52 nm, and 52 nm, respectively (see Table 5.4 for the detail). Hence, except for CsPbBr<sub>3</sub> 10% sample, the other samples exhibit the aggregation effect of nano-crystallite when the MDMO-PPV–CsPbBr<sub>3</sub> composites were formed. Recall that the oleic acid and oleylamine ligands are immiscible with MDMO-PPV polymeric chains (Figure 5.3c), indicating that CsPbBr<sub>3</sub> could be aggregated during the drying process of the drop-cast films. However, the 10% sample was the exception, which might be related to typical thermodynamic phenomena: small amounts could be at least partially miscible within a solid matrix ( $\Delta G_{mix} < 0$  in many binary systems).

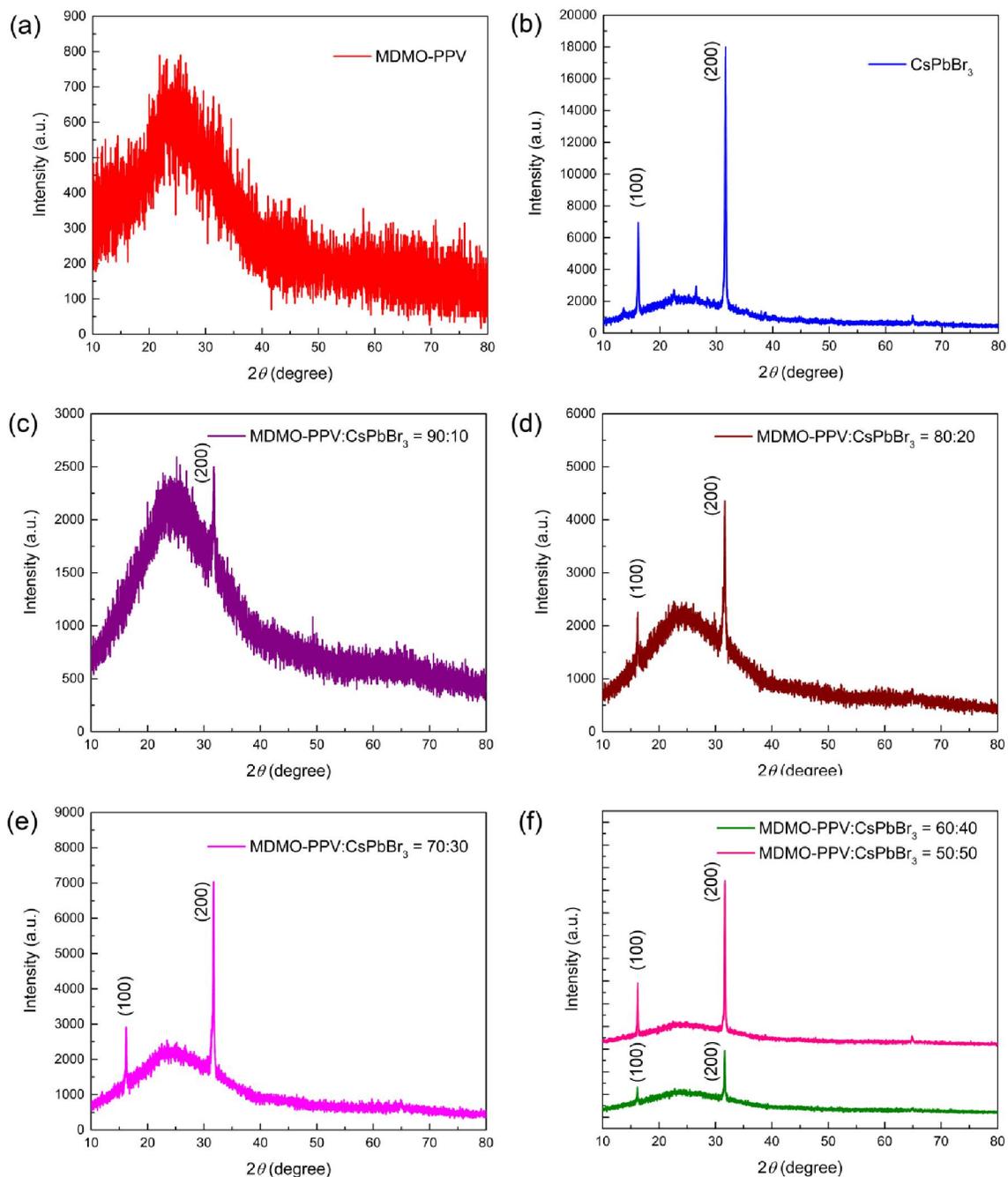
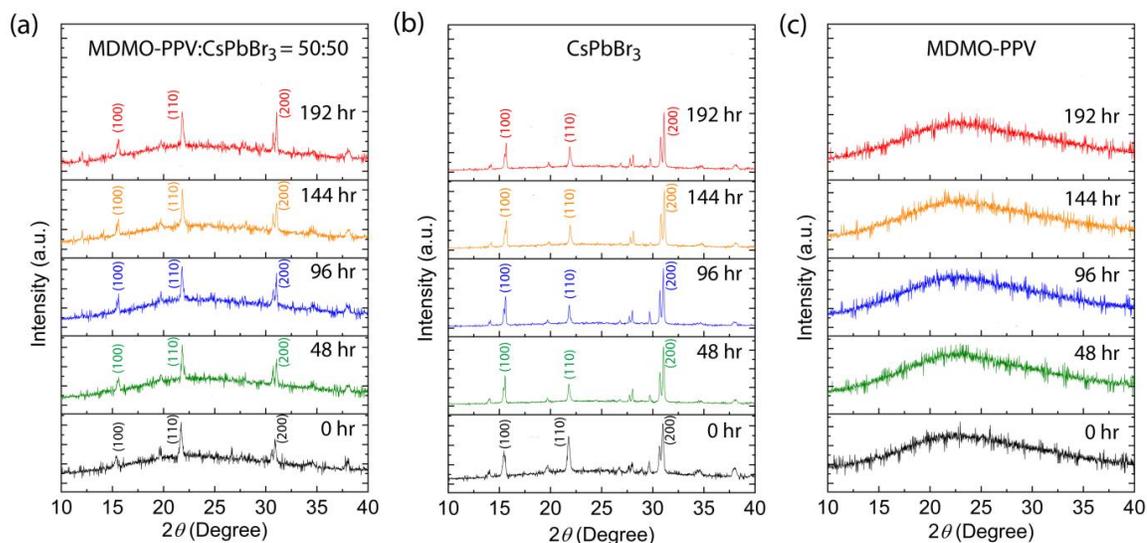


**Figure 5.4.** XRD patterns of drop-cast films on the glass substrate: (a) MDMO-PPV; (b) CsPbBr<sub>3</sub> QD nanocrystals; (c) MDMO-PPV: CsPbBr<sub>3</sub> = 90:10; (d) MDMO-PPV: CsPbBr<sub>3</sub> = 80:20; (e) MDMO-PPV: CsPbBr<sub>3</sub> = 70:30; and (f) MDMO-PPV: CsPbBr<sub>3</sub> = 60:40 and MDMO-PPV: CsPbBr<sub>3</sub> = 50:50.

**Table 5.4.** Crystallite size ( $D$ ) of CsPbBr<sub>3</sub> nanocrystals at the (200) crystallographic plane as a function of the composition of the MDMO-PPV:CsPbBr<sub>3</sub> composites. Here, MDMO-PPV has  $M_n$  of 120,000 g · mol<sup>-1</sup>.

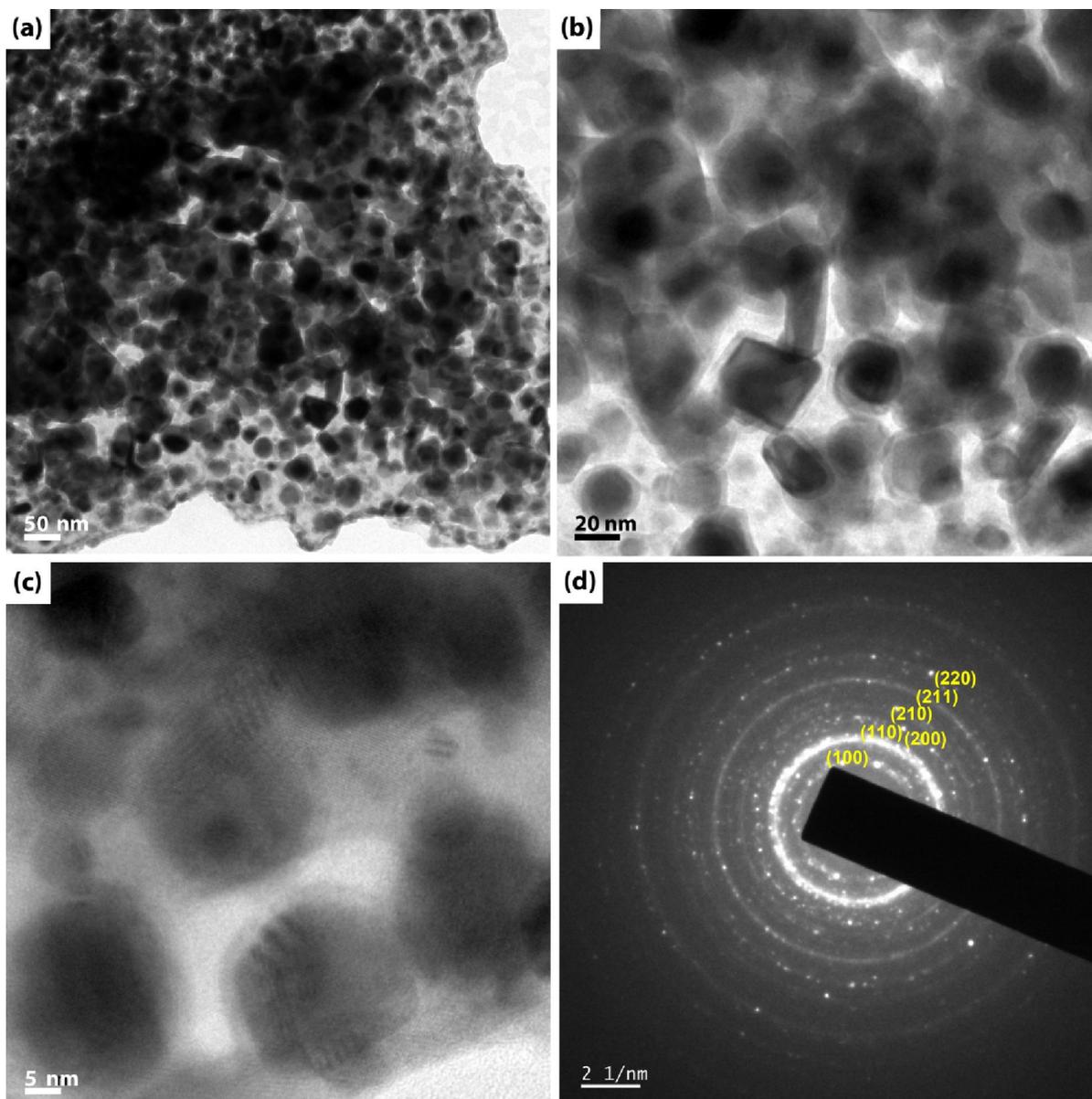
MDMO-PPV:CsPbBr <sub>3</sub>	$2\theta$ (°)	$\theta$ (°)	$\beta$ (radian)	$D$ (nm)
90:10	31.8	15.90	0.004363	33
80:20	31.7	15.85	0.003461	42
70:30	31.7	15.85	0.003054	48
60:40	31.7	15.85	0.002793	52
50:50	31.7	15.85	0.002793	52

Figure 5.5 shows the XRD patterns of the drop-cast film as a function of time under ambient condition. Here, not only (100) and (200) crystallographic peaks, but also (110) peak are clearly observed, indicating the orientation order is partially diminished compared to that in the previous batch samples (Figure 5.4). As shown in Figure 5.5a, the composite film (MDMO-PPV:CsPbBr<sub>3</sub> = 50:50) shows a structural stability by exhibiting the similar XRD patterns in spite of the significant time change up to ~192 hours. This structural stability is based on the stable CsPbBr<sub>3</sub> structure (Figure 5.5b) in the stereo-irregular MDMO-PPV polymer (Figure 5.5c). Note that the wide bandgap CsPbBr<sub>3</sub> semiconductor has the Goldsmith tolerance factor ( $\tau$ ) of 0.816, falling in the stability regime,  $0.813 \leq \tau \leq 1.107$  [219]. Furthermore, CsPbBr<sub>3</sub> has a high thermal stability (decomposition temperature onset ~580 °C) [155] and undergoes single-crystallization in water [227], demonstrating its superior stability compared to organic-inorganic hybrid CH<sub>3</sub>NH<sub>3</sub>PbI<sub>3</sub> perovskite [102,155,228].



**Figure 5.5.** XRD patterns of drop-cast films as a function of time: **(a)** MDMO-PPV: CsPbBr<sub>3</sub> = 50:50; **(b)** CsPbBr<sub>3</sub> QD nanocrystals; and **(c)** amorphous MDMO-PPV. Here, ‘0 hr’ indicates the *as-prepared* sample.

Figures 5.6a-c show TEM image of CsPbBr<sub>3</sub> QD nanocrystals when oleic acid and oleylamine were used as the ligand system. Here, the particle size is distributed in the nanoscale (e.g., ~33-52 nm or even more in the case of aggregation) whereas the particle shape is not exactly cubic. This indicates that the cubic crystals might be roughly organized with partial disorder, specifically at the surface. Notably, a spherical surface is the most stable because it allows the lowest interfacial surface energy. Interestingly, when we checked the selected area electron diffraction (SAED) patterns (Figure 5.6d) of the drop cast CsPbBr<sub>3</sub> nanocrystals, the circular patterns were clearly observed, indicating they are polycrystalline. Furthermore, the most intense pattern was observed at (110) crystallographic plane instead of (200) plane [226]. This observation indicates that the drop-cast CsPbBr<sub>3</sub> QDs have an orientational order with [110] direction on the surface of the TEM copper grid and/or the electron beams might affect the morphology of a composite film during this measurement.



**Figure 5.6.** TEM image of the drop cast CsPbBr<sub>3</sub> nanocrystals on the copper grid: (a) scale bar = 50 nm, (b) scale bar = 20 nm and (c) scale bar = 5 nm. (d) SAED patterns of the drop cast CsPbBr<sub>3</sub> nanocrystals.

Figure 5.7 shows the SEM image of (a) MDMO-PPV, (b) MDMO-PPV:CsPbBr<sub>3</sub> = 80:20 and (c) MDMO-PPV:CsPbBr<sub>3</sub> = 50:50, for which the samples were drop-cast on top of the

glass substrate. Figure 5.7b exhibits the additional sub-microscale domains compared to Figure 5.7a.

However, in the case of Figure 5.7c, it displays microscale aggregations of CsPbBr<sub>3</sub> crystals as expected from the phase behavior study in Figure 3c, i.e., the ligands are immiscible with MDMO-PPV and thus CsPbBr<sub>3</sub>-ligand (oleic acid and oleylamine) complexes can form nano-/micro-scale domains in the MDMO-PPV matrix polymer.

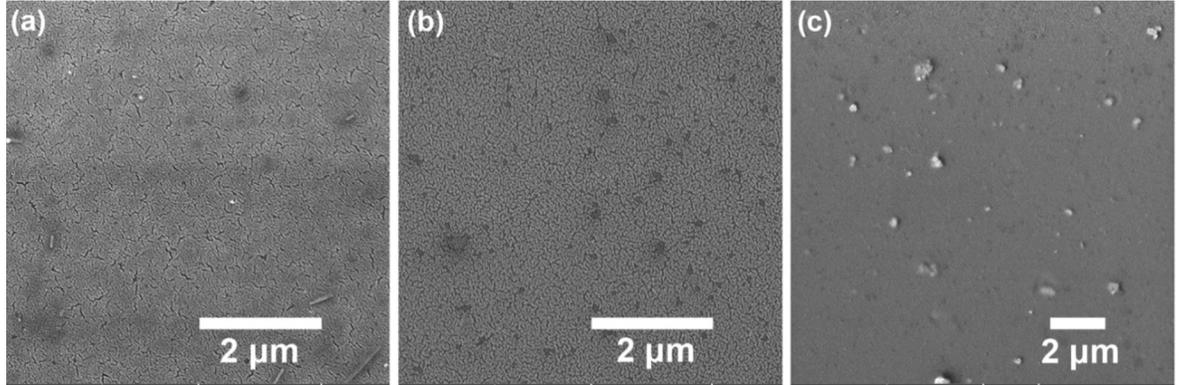
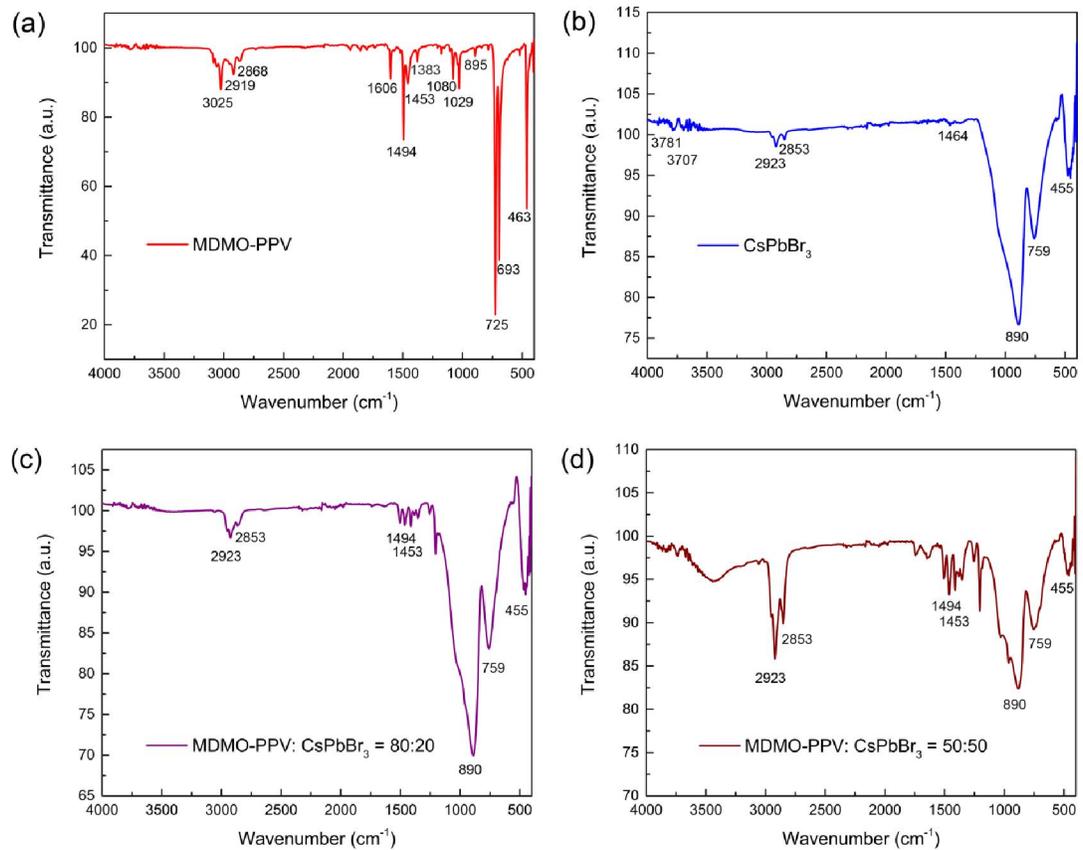


**Figure 5.7.** SEM images of the drop-cast films: (a) MDMO-PPV; (b) MDMO-PPV:CsPbBr<sub>3</sub>= 80:20; and (c) MDMO-PPV:CsPbBr<sub>3</sub>= 50:50.

Figure 5.8 shows the FT-IR spectra of (a) MDMO-PPV, (b) CsPbBr<sub>3</sub> nanocrystals, (c) MDMO-PPV:CsPbBr<sub>3</sub> = 80:20 and (d) MDMO-PPV:CsPbBr<sub>3</sub> = 50:50 composites. First, Figure 5.8a shows the FT-IR data of MDMO-PPV. The vibrational modes at 3025 cm<sup>-1</sup>, 2919 cm<sup>-1</sup>, and 2868 cm<sup>-1</sup> correspond to the CH, CH<sub>2</sub> and CH<sub>3</sub> stretching, respectively [198]. The peaks at 1606 cm<sup>-1</sup> and 1494 cm<sup>-1</sup> are related to the aromatic phenyl ring mode, and asymmetric C-H bending, respectively [52,229]. The peaks at 1453 cm<sup>-1</sup> and 1383 cm<sup>-1</sup> corresponds to anti-symmetric and anti-symmetric alkyl CH<sub>2</sub>, respectively [52,229]. The peak at 1029 cm<sup>-1</sup> is associated with the symmetric C-O-C stretching vibration mode. The peak at 895 cm<sup>-1</sup> is related to the phenyl CH-wagging signifying the dipole normal to phenyl vinyl plane, whereas the peaks at 725 cm<sup>-1</sup>, 693 cm<sup>-1</sup>, and 463 cm<sup>-1</sup> correspond to the out-of-plane ring bend of phenyl ring [230]. Second, Figure 8b shows the FT-IR data of CsPbBr<sub>3</sub>-ligand (oleic acid and oleylamine) complexes. The weak peaks at 3781 cm<sup>-1</sup>, and 3707 cm<sup>-1</sup> are ascribed to N-H vibration from the oleylamine ligand [178]. The peaks at 2923 cm<sup>-1</sup> and 2853 cm<sup>-1</sup> correspond to the C-H stretching vibration [231].

The peak at  $1464\text{ cm}^{-1}$  is known to be associated with the  $\text{CsPbBr}_3$ -ligand interactions [116,199], whereas the three peaks at  $890\text{ cm}^{-1}$ ,  $759\text{ cm}^{-1}$ , and  $455\text{ cm}^{-1}$  are typical ones observed in cesium lead halide compounds [196,232].

Third, in the case of  $\text{MDMO-PPV-CsPbBr}_3$  composites, the peaks in Figure 5.8c and d are the combination of Figure 8a and b because  $\text{MDMO-PPV}$  and  $\text{CsPbBr}_3$ -ligand complex are immiscible.



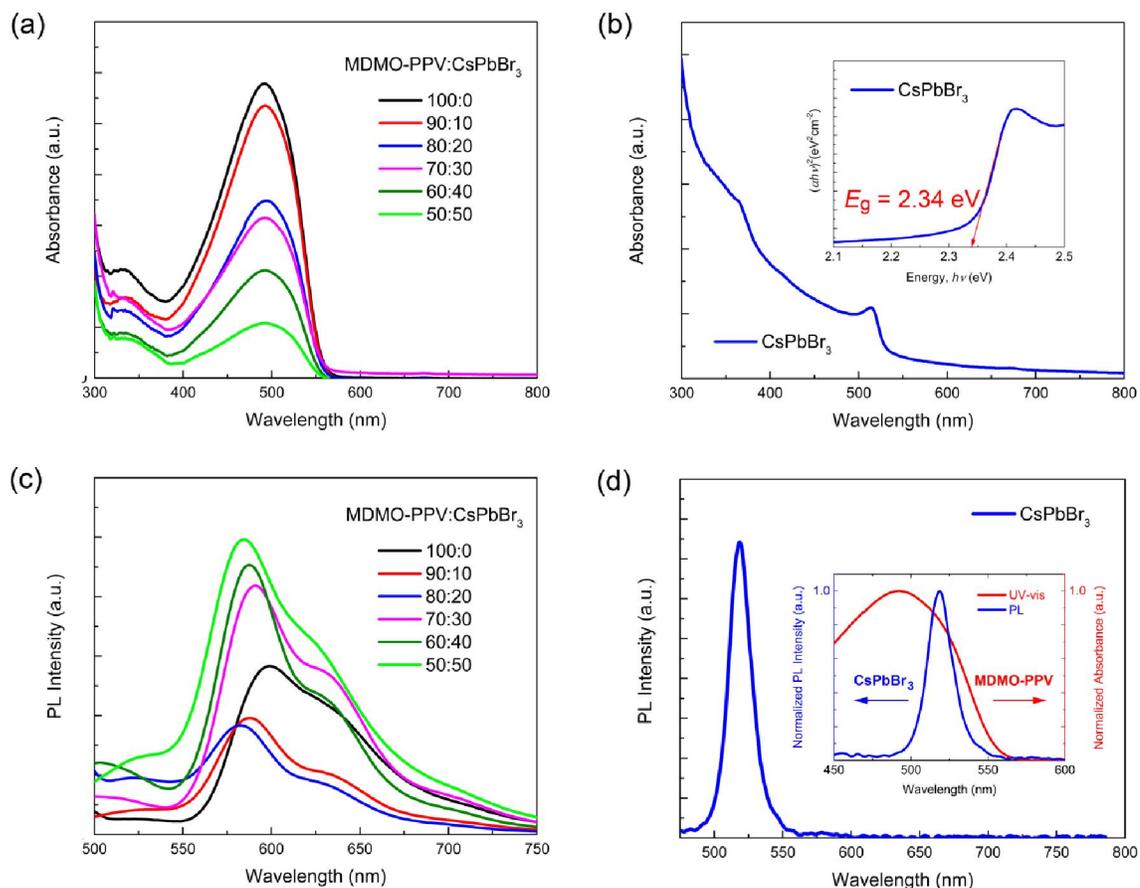
**Figure 5.8.** FT-IR spectra at ATR mode: (a)  $\text{MDMO-PPV}$ ; (b)  $\text{CsPbBr}_3$  nanocrystals; (c)  $\text{MDMO-PPV}:\text{CsPbBr}_3 = 80:20$ ; and (d)  $\text{MDMO-PPV}:\text{CsPbBr}_3 = 50:50$ .

Figure 5.9 shows UV-vis absorption and PL emission spectra for the spin-coated films (at total  $3\text{ mg mL}^{-1}$  solution; spinning speed of 3000 rpm). Figure 5.9a demonstrates that when  $\text{CsPbBr}_3$  was added into the  $\text{MDMO-PPV}$  matrix, the absorption decreases with increasing the portion of  $\text{CsPbBr}_3$  [205,225]. Figure 5.9b shows the absorption spectra of  $\text{CsPbBr}_3$  films. On the other hand, Figure 5.9c shows the PL emission spectra as a function of

composite composition. As shown in Figure 9c, when MDMO-PPV:CsPbBr<sub>3</sub> = 90:10 and 80:20, the PL emission decreases, which might be due to a partial quenching effect (probably through defect sites and/or energetic difference in electron affinity in the specific arrangement CsPbBr<sub>3</sub> QDs and MDMO-PPV) in these morphologies with ~10-20wt% CsPbBr<sub>3</sub>. However, when MDMO-PPV:CsPbBr<sub>3</sub> = 70:30, 60:40, and 50:50 (i.e., more than 30 wt.% CsPbBr<sub>3</sub>; here, CsPbBr<sub>3</sub> QDs might be more aggregated resulting in less surface defects; recall Table 5.4), the PL emissions were enhanced compared with the pure MDMO-PPV film. Importantly, the partial blue shift in the PL emission should be related to the disturbed  $\pi$ - $\pi$  inter-/intra-molecular interactions among MDMO-PPV chain molecules by incorporating CsPbBr<sub>3</sub> QDs in the composite films. In other words, MDMO-PPV matrix was diluted by the presence of CsPbBr<sub>3</sub> QDs. Figure 9d shows the PL emission spectrum of CsPbBr<sub>3</sub> film, which is overlapped with the absorption spectrum of MDMO-PPV film (see the inset of Figure 5.9d). Hence, when the donor chromophore CsPbBr<sub>3</sub> QDs were excited, the energy in its electronic excite state could be transferred to the acceptor chromophore MDMO-PPV chain molecules through non-radiative dipole coupling, which is so called Förster resonance energy transfer (FRET) [233]. Here, the energy transfer rate ( $k_{ET}$ ) is defined as follows[233,234]:

$$k_{ET} = \frac{1}{\tau_D^0} \left( \frac{R_0}{R_{DA}} \right)^6 \quad (5.4)$$

where  $\tau_D^0$  is donor life time,  $R_0$  is Förster radius (the critical distance, typically ~ 5 nm), and  $R_{DA}$  is the donor-acceptor distance. Hence, the aforementioned FRET should be the origin of the enhanced PL when the compositions of the composite were MDMO-PPV:CsPbBr<sub>3</sub> = 70:30, 60:40 and 50:50, respectively. Note that based on the UV-Vis absorption in Fig. 9a, when the absorption of MDMO-PPV was somewhat reduced by incorporating CsPbBr<sub>3</sub> (e.g., ~30-50 wt.%), the PL emission was enhanced compared to the pure MDMO-PPV film, indicating the importance of the partial reduction of MDMO-PPV portion in the composite films. Note that  $k_{ET}$  is inversely proportional to the sixth power of  $R_{DA}$ , suggesting the significance of the donor-acceptor molecular configuration in the composite films.



**Figure 5.9.** Absorption and emission spectra of the spin-coated films: **(a)** UV-vis absorption spectra of MDMO-PPV–CsPbBr<sub>3</sub> composites as a function of composition; **(b)** UV-vis absorption spectra of CsPbBr<sub>3</sub> nanocrystals. Inset: Tauc plot,  $(\alpha hv)^2$  vs.  $hv$  for determining the optical bandgap ( $E_g \approx 2.34$  eV) of CsPbBr<sub>3</sub> nanocrystals, in which  $\alpha$  is absorption coefficient,  $h$  is Planck constant and  $\nu$  is frequency of light. **(c)** PL emission spectra of MDMO-PPV–CsPbBr<sub>3</sub> composites as a function of composition; and **(d)** PL emission spectra of CsPbBr<sub>3</sub> nanocrystals. Inset: Comparison of UV-vis absorption of MDMO-PPV and PL emission of CsPbBr<sub>3</sub> nanocrystals.

Herein, the energy of the excited donor CsPbBr<sub>3</sub> nanocrystals (CBM $\approx$  -3.3 eV and VBM $\approx$  -5.6 eV) might be well transferred to the acceptor MDMO-PPV macromolecules (LUMO $\approx$  -3.2 eV and HOMO $\approx$  -5.4 eV) according to the scheme in Figure 5.10 [208–210].

Importantly, it should be notable that (1) the nanoscale particle size of CsPbBr<sub>3</sub> QDs should be distributed, indicating a partial distribution of the energy levels such as CBM and VBM, and that (2) the aggregation should be affected by the concentration of CsPbBr<sub>3</sub> QDs in MDMO-PPV, resulting in the composition dependency of optical properties. The phase transformation (here, the aggregation of QDs) is for reducing the Gibbs free energy to be stabilized (recall the phase behavior part in Figure 3c).

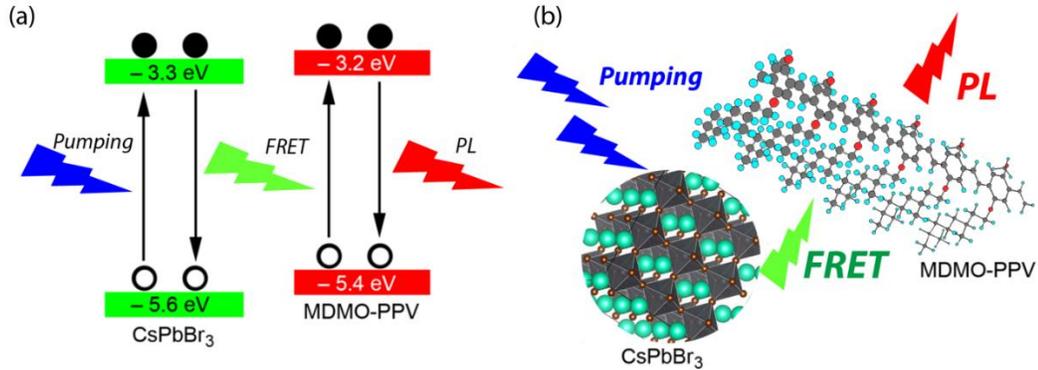


**Figure 5.10.** (a) Schematic energy diagram and (b) PL emission through the FRET between CsPbBr<sub>3</sub> and MDMO-PPV.

Figure 5.11 shows the electrochemical impedance spectroscopy (EIS) data for MDMO-PPV and MDMO-PPV:CsPbBr<sub>3</sub> with 50:50 wt.% composition. Here, the working electrode was a glassy carbon electrode with 3 mm in diameter on which about 120  $\mu\text{m}$  thick film was deposited. EIS was measured at 0 V Vs. Ag/AgCl as the reference electrode and platinum wire as the counter electrode. As shown in Figure 5.11, when the MDMO-PPV film incorporated with 50% CsPbBr<sub>3</sub>, the bulk resistance (i.e., a half-circle size of the EIS curve) considerably decreased from  $\sim 1.4 \times 10^7 \Omega$  to  $\sim 3.2 \times 10^4 \Omega$ . This observation indicates that the hybrid MDMO-PPV–CsPbBr<sub>3</sub> QD composite is beneficial for boosting the charge transport in the thin film. Here, the smaller charge transfer resistance ( $\sim 3.2 \times 10^4 \Omega$ ) in the composite film should be related to the crystalline perovskite component (CsPbBr<sub>3</sub> QDs) displaying superior properties in terms of charge mobility [235], dielectric constant [236], electron-hole diffusion length [237], and ionic transport [238]. On the other hand, the amorphous MDMO-PPV polymer has inferior charge mobility due to its disordered structure [239], resulting in high charge transfer resistance  $\sim 1.4 \times 10^7 \Omega$  in this study.

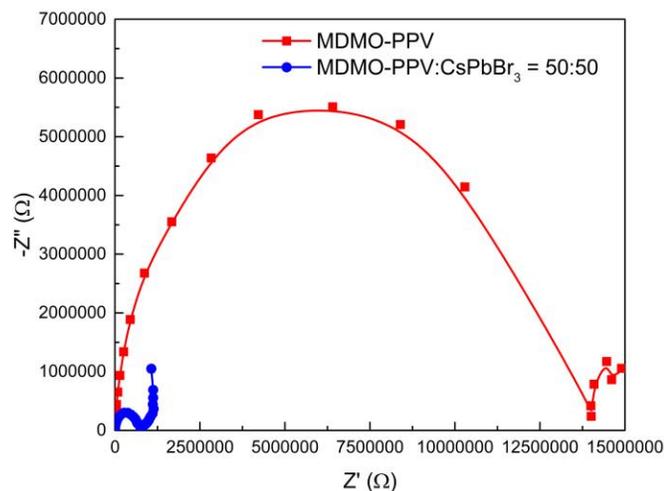


**Figure 5.11.** Electrochemical impedance spectroscopy (EIS) data of the pure MDMO-PPV and MDMO-PPV: CsPbBr<sub>3</sub> = 50:50 wt.% composition.

#### 5.4. Conclusions

In this work, we studied the light-emitting MDMO-PPV–CsPbBr<sub>3</sub> composite systems as a function of composition. First, through the phase behavior study, we identified that MDMO-PPV–oleic acid and MDMO-PPV–oleylamine systems are immiscible, indicating that the ligands for CsPbBr<sub>3</sub> cannot act as a compatibilizer but promote self-aggregation, i.e., phase separation. On the other hand, the two ligand molecules are easily soluble in the toluene solvent. More importantly, MDMO-PPV–toluene is partially miscible ( $\chi_{12} \sim 0.5$ ), suggesting that by increasing temperature, the solution could be well miscible. Second, through the XRD study, we identified the sharp (100) and (200) crystallite peaks from all the MDMO-PPV–CsPbBr<sub>3</sub> composite films, indicating that MDMO-PPV and CsPbBr<sub>3</sub> are clearly phase-separated. Here, the CsPbBr<sub>3</sub> domains with 33-52 nm crystallite size were embedded in the amorphous MDMO-PPV matrix. Third, it is interesting to see that CsPbBr<sub>3</sub> QD nanocrystals show a (110) orientational order on top of the TEM copper grid. Fourth, through the SEM images, we identified the microscale aggregation of CsPbBr<sub>3</sub> nanocrystals from the MDMO-PPV:CsPbBr<sub>3</sub>= 50:50 composite film which is in line with the prediction of Flory-Huggins theory. Fifth, the UV-vis absorption and PL emission results indicate that the MDMO-PPV–CsPbBr<sub>3</sub> composite films show less absorption but more emission when CsPbBr<sub>3</sub>  $\geq$  30 wt.%.

Finally, EIS spectra demonstrated that the MDMO-PPV:CsPbBr<sub>3</sub>= 50:50 composite has smaller resistance than the pure MDMO-PPV film, indicating that the composite approach is useful for enhancing the charge transport in an electrochemical cell.

As a future work, it is a topic of interest to study the polymer–perovskite composite when the ligand molecules can act as a compatibilizer, i.e., the polymer and ligands are miscible to each other. Furthermore, if the ligand can transfer charge, it could be beneficial for the effective electrical contact between conjugated polymer and perovskite complexed with  $\pi$ -bonded ligands. Therefore, this study shows improvement in structural, optical and electrochemical properties so we suggest that this approach is promising for electrochemical and optoelectronic applications.

## Chapter Six

### 6. Facile Synthesis and Characterization of Polymer-Mixed Halide Perovskite Composites

#### 6.1. Introduction

Metal halide perovskite semiconductors have excellent optoelectronic characteristics includes tunable band gap, narrow emission widths, high color purity, low exciton binding energy, defect tolerance, high light absorption coefficient, easily processed in solution, and high PL. These characteristics makes them suitable for versatile optoelectronic applications like solar cells, LED, photodetectors, lasers, etc [102,240,241]. The perovskite materials have the same structure as calcium titanate ( $\text{CaTiO}_3$ ), which was first founded by a Russian mineralogist in 1839. The generalized chemical formula for perovskite is  $\text{ABX}_3$ , where A and B are cations where as X is a halide [3,82,242].

Because of its photophysical characteristics and potential applications in lighting and display, researchers are now interested in all-inorganic lead halide perovskites. This is mostly because of their highly adjustable emission band, narrow FWHM, high PLQYs, and superb color purity [243]. Here, the perovskite materials have been synthesized by a typical hot-injection and ligand-assisted precipitation procedure, and there has been a significant improvement in both properties and performances over the past decades. However, in spite of these advancements, some technical issues needs improvement. For example, further research should be done on the poor efficiency of blue perovskite LEDs (PeLEDs), the trapping defects that create the charge-carrier injection barrier, and the significant nonradioactive recombination from surface defects [244]. In addition a mixed halide perovskite may suffer with stability issue due to phase segregation in spite of the available various colors through changing composition [245,246]. Accordingly, some strategies such as encapsulations, doping, and polymer mixing were designed to solve the remaining technical problems [247,248]. Furthermore, a facile room temperature (RT) processing technique have been developed with potential merits such as low cost and facile preparation, leading to an improved PL efficiency [206,241,249]. Some examples are as follows: the effects of mixing a blue emitting, poly (9,9-dioctylfluorene) (PFO) and green perovskite,

CsPbBr<sub>3</sub> or red emitting perovskite, CsPbBr<sub>1.5</sub>I<sub>1.5</sub> NCs and a yellow emitting poly(9,9-dioctylfluorene-co-benzothiadiazole) (F8BT) with the red NCs, in different amounts.

According to the findings, one of the most pertinent strategies for the development of optoelectronic devices is the interaction between polymer and perovskite NCs [250]. The preparation of blue-emitting lead mixed halide perovskite, CsPbX<sub>3</sub> (X= Br, Cl) NCs requires a complicated process to control composition and purification [240,241]. In the case of polymer/perovskite composites, the resulting mechanical, chemical and thermal stability with solution processibility demonstrates that the mixing strategy with conjugated polymer is good for optoelectronic devices, for example solar cells and LEDs [251,252]. Noticeably, a blue emitting perovskite still shows a low efficiency and limited stability contrast to green and/or red emitting perovskites, indicating a further study is needed for solving this technical issue. For example, a commercially available organic polymer and/or inorganic nanoparticles were composited with perovskites for tuning the PL properties of perovskites [251].

In this work, we aim to prepare a pure blue emitting mixed halide perovskite/polymer composite. Here we used poly[2-methoxy-5-(3,7-dimethyloxy)-1,4-phenylenevinylene] (MDMO-PPV) as a light-emitting polymer. In addition, a cesium lead mixed halide blue emitting perovskite, namely, CsPb(Br<sub>1-x</sub>Cl<sub>x</sub>)<sub>3</sub> was synthesized at RT condition and then it was incorporated into the MDMO-PPV polymer with various concentrations. Importantly, the optical bandgap, crystallinity and PL emission could be affected by changing the amount of chlorine content.

## 6.2. Materials and Methods

### 6.2.1. Chemicals

Cesium bromide CsBr (99.9%,Sigma-Aldrich), lead bromide (PbBr<sub>2</sub>, 99.0%, Delhi India ), lead chloride ( PbCl<sub>2</sub>,99.0%, Delhi India), Oleic acid (OA, 98%,Sigma-Aldrich), oleylamine (OAm,70%,Sigma-Aldrich), *N,N*-dimethylformamide (DMF,99.5%,AR chemicals, Delhi, India), toluene(≥ 99.5%, AR chemicals, Delhi, India),ethyl acetate (≥ 99.8% ,Sigma-Aldrich), Acetone (≥99%,Sigma-Aldrich), Isopropanol(IPA,99.5%,Delhi India), and MDMO-PPV with molecular weight of 120 kg.mol<sup>-1</sup> were purchased from Sigma-Aldrich and are used without further purifications.

### 6.2.2. Synthesis of CsPb(Br<sub>1-x</sub>Cl<sub>x</sub>)<sub>3</sub> (X= 0.33, 0.50)

The perovskite was synthesized according to the literature report [251]. Here, CsBr (0.2 mmol, 43 mg), PbBr<sub>2</sub> (0.134mmol, 49mg or 0.1mmol, 37mg) and PbCl<sub>2</sub> (0.066 mmol, 18 mg or 0.1mmol, 28mg) were used to prepared CsPb(Br<sub>1-x</sub>Cl<sub>x</sub>)<sub>3</sub> (X= 0.33 or 0.50) with a mole ratio of 3:2:1 and 2:1:1 respectively, using 5 mL DMF and OA/OAm (=1:1 volume ratio) ligands. Next, for three hours at 30°C, the solutions were vigorously stirred [252]. Then, 15 mL of ethyl acetate was incorporated in perovskite precursor solution and then centrifuged at 8000 rpm for 10 min. After that, the precipitate was once again dispersed in toluene for characterizations after the supernatant was extracted. The resulting perovskite in toluene exhibited a blue emission under 365 nm UV light illuminations.

### 6.2.3. Preparation of MDMO-PPV :CsPb(Br<sub>1-x</sub>Cl<sub>x</sub>)<sub>3</sub> (X= 0.33, 0.50) Composites

The MDMO-PPV /CsPb(Br<sub>1-x</sub>Cl<sub>x</sub>)<sub>3</sub> composites were prepared according to the literature report [205,253]. Here, MDMO-PPV (3mg/mL toluene) and CsPb(Br<sub>1-x</sub>Cl<sub>x</sub>)<sub>3</sub> (~36-37mg/mL toluene) (MDMO-PPV:perovskite solutions= 1:1; 1:2 volume ratio) were prepared. In addition, the pure MDMO-PPV polymer and CsPb(Br<sub>1-x</sub>Cl<sub>x</sub>)<sub>3</sub> were deposited onto a glass substrate as a reference.

#### 6.2.4. Characterizations

The structural characteristics of the samples were determined using X-ray diffraction (XRD) measurements measured by the Rigaku mini flex-300/600 diffractometer (Rigaku, Tokyo, Japan). The irradiation used  $\text{CuK}\alpha, \lambda=1.5406\text{\AA}$  at 40KV and 15mA used in the XRD characterization measurement. The change of scanning angle ( $2\theta$ ) between  $10^\circ$ - $80^\circ$  the step sizes of  $0.01^\circ$  at  $5^\circ \text{ min}^{-1}$ . FTIR spectra were obtained by a FTIR Spectrometer (PerkinElmer Spectrum Two FTIR Spectrometer) used to analyze functional groups and chemical interactions. Here, FT-IR spectra of the samples in the range  $4000$ – $400 \text{ cm}^{-1}$  were recorded with a resolution of  $4 \text{ cm}^{-1}$  using ATR as a sampling technique.

The optical characteristics of samples were measured by using ultraviolet-visible (UV–vis) absorption by UV–Vis Spectrophotometer fluorescence (SHIMADZU UV-2600, Kyoto, Japan). The PL spectra of the samples were characterized by a spectrophotometer (SHIMADZU RF-6000, Kyoto, Japan) at an excitation wavelength of 380nm and 460nm. All the characterization was carried out under RT.

#### 6.3. Results and Discussion

The structural characteristics of mixed halide perovskite  $\text{CsPb}(\text{Br}_{1-x}\text{Cl}_x)_3$  ( $x=0.33, 0.50$ ) and its composite with MDMO-PPV were characterized using XRD. The results were concluded in Table 6.1, showing that both the chlorine contents as well as blending ratio has been affected the properties of composite, e.g., crystallinity.

Table 6.1. Crystallite size (D) of  $\text{CsPb}(\text{Br}_{1-x}\text{Cl}_x)_3$  and its composite. Here,  $\beta$  denotes FWHM at angle  $\theta$ .

Polymer/perovskite Composite	$\theta$ ( $^\circ$ )	$\beta$ (radian)	D (nm)
$\text{CsPb}(\text{Br}_{1-x}\text{Cl}_x)_3$ ( $x=0.33$ )	16.23	0.002513	57.46
$\text{CsPb}(\text{Br}_{1-x}\text{Cl}_x)_3$ ( $x=0.50$ )	16.37	0.002513	57.49
MDMO-PPV	a)	a)	a)
MDMO-PPV: $\text{CsPb}(\text{Br}_{1-x}\text{Cl}_x)_3$ ( $x=0.33$ ) (1:1)	16.25	0.013400	10.77
MDMO-PPV: $\text{CsPb}(\text{Br}_{1-x}\text{Cl}_x)_3$ ( $x=0.50$ ) (1:1)	16.32	0.004020	34.49
MDMO-PPV: $\text{CsPb}(\text{Br}_{1-x}\text{Cl}_x)_3$ ( $x=0.33$ ) (1:2)	16.25	0.002932	49.25
MDMO-PPV: $\text{CsPb}(\text{Br}_{1-x}\text{Cl}_x)_3$ ( $x=0.50$ ) (1:2)	16.16	0.006702	21.54

a) Amorphous polymer

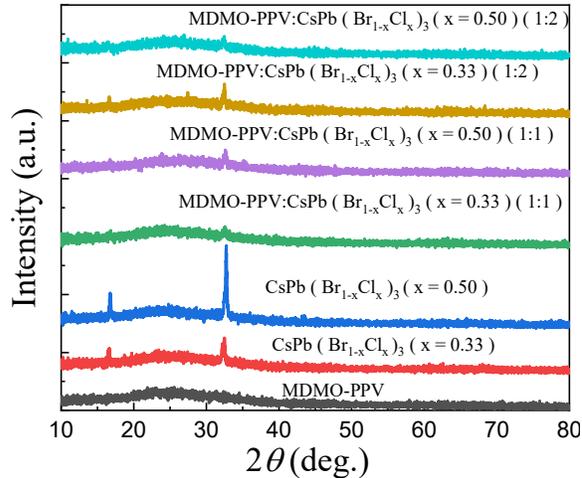


Figure 6.1. XRD patterns for  $\text{CsPb}(\text{Br}_{1-x}\text{Cl}_x)_3/\text{MDMO-PPV}$  composites drop cast films as well as its pure components (i.e., polymer and perovskite) and dried ambient condition. An amorphous polymer MDMO-PPV, shows an amorphous halo at  $2\theta \approx 25^\circ$  (see the black solid line).

According to UV-visible spectroscopy measurements, the absorption spectra of pure blue-emitting perovskites made from a chlorine and bromine mixture demonstrate more absorption (i.e., relatively smaller band gap) at lower chlorine contents and decreased absorption (i.e., relatively wider band gap) at higher chlorine contents as observed in Figure 6.2. Moreover, when mixed halide perovskite was composited with MDMO-PPV polymer, the overall shape follows the MDMO-PPV's absorption spectra but the range is partially diminished as reported in elsewhere [254].

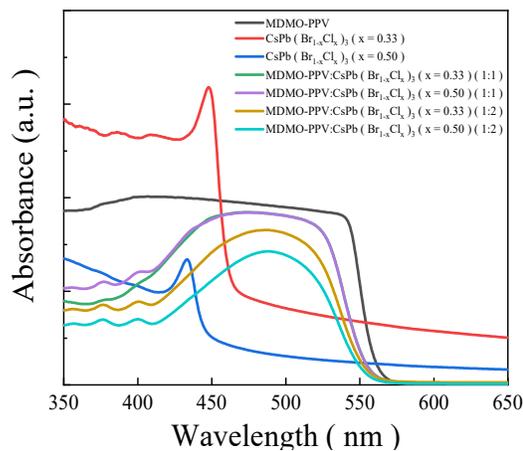


Figure 6.2. UV-Vis spectra the  $\text{CsPb}(\text{Br}_{1-x}\text{Cl}_x)_3/\text{MDMO-PPV}$  composites solutions as well as its pure component (polymer and perovskite).

The optical bandgap ( $E_g$ ) of pure blue emitting all inorganic perovskites and perovskite/polymer composites was clearly estimated based on a Tauc model according to the literature report [255]. As presented in Figure 6.3,  $\text{CsPb}(\text{Br}_{1-x}\text{Cl}_x)_3$  ( $x=0.33$ ) shows  $E_g \approx 2.69$  eV and  $\text{CsPb}(\text{Br}_{1-x}\text{Cl}_x)_3$  ( $x=0.50$ ) exhibits  $E_g \approx 2.78$  eV whereas MDMO-PPV displays  $E_g \approx 2.23$  eV. However, when MDMO-PPV were mixed with  $\text{CsPb}(\text{Br}_{1-x}\text{Cl}_x)_3$  perovskite, the optical bandgap is  $\sim 2.27$  eV, i.e., a wider bandgap compared with that of MDMO-PPV, it may indicating MDMO-PPV chain molecules are dispersed in  $\text{CsPb}(\text{Br}_{1-x}\text{Cl}_x)_3$ . Note that the amount of MDMO-PPV in perovskite-polymer composite is about  $\sim 10$  wt.% of  $\text{CsPb}(\text{Br}_{1-x}\text{Cl}_x)_3$ .

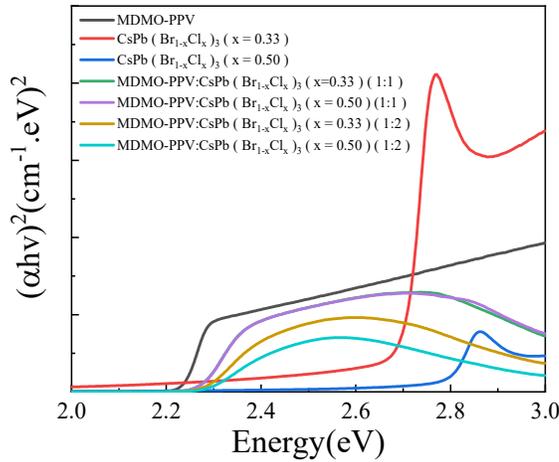


Figure 6.3. Determination of optical bandgap of samples  $(ahv)^2$  vs. energy

The PL emission spectra  $\text{CsPb}(\text{Br}_{1-x}\text{Cl}_x)_3$ /MDMO-PPV composites as well as its pure component (polymer and perovskite) are displayed in Figure 6.4.

The  $\text{CsPb}(\text{Br}_{1-x}\text{Cl}_x)_3$  ( $x=0.50$ ),  $\text{CsPb}(\text{Br}_{1-x}\text{Cl}_x)_3$  ( $x=0.33$ ), and MDMO-PPV PL emission peaks were measured at 450 nm, 463 nm, and 566 nm, respectively. However, when  $\text{CsPb}(\text{Br}_{1-x}\text{Cl}_x)_3$  and MDMO-PPV were mixed together to form a composite, the PL emission peak was seen at 558 nm. Thus, the finding indicates that the PL emission of perovskite could be adjusted by altering the amount of chlorine concentrations according to the previous report [249]. Typically, the creation of excitons in the polymer-perovskite composite is responsible for the rise in PL emission that follows an increase in dopant concentration [256].

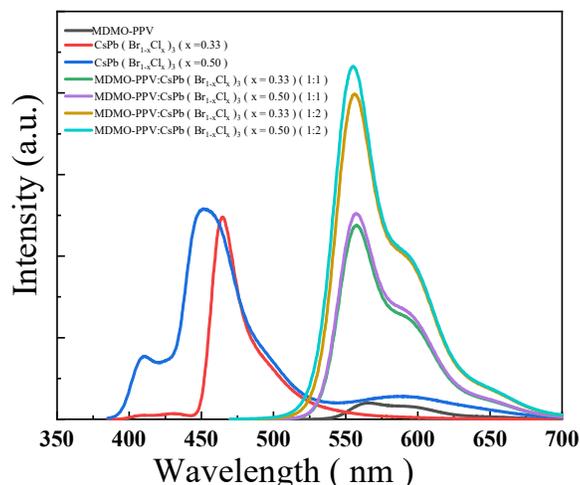


Figure 6.4. PL spectra of  $\text{CsPb}(\text{Br}_{1-x}\text{Cl}_x)_3/\text{MDMO-PPV}$  composites solutions as well as pure component (polymer and perovskite).

The FTIR spectroscopy has been used to identify a function group in the chemical systems, which was performed in the range  $4000\text{-}400\text{ cm}^{-1}$  in our study. From figure 6.5, the peak position of bands in the range  $2920\text{-}3026\text{ cm}^{-1}$  are categorized as C-H functional groups [198,257]. Accordingly, the peak position around at  $2920\text{ cm}^{-1}$  shows symmetric C-H stretching [116], and at peak  $1497\text{ cm}^{-1}$ , O-H and C-H bond stretching was observed [258,259]. IR peaks in  $1250\text{-}1000\text{ cm}^{-1}$  range reveal that C-O stretching vibrations [257]. On the other hands, the peaks round at  $1605\text{ cm}^{-1}$  and  $1497\text{ cm}^{-1}$  show the ring mode of vibration [259]. Aromatic out-of-plane C-H bends and ring blend were indicated at peak position of  $729\text{ cm}^{-1}$  and  $688\text{ cm}^{-1}$ , respectively [257,258].

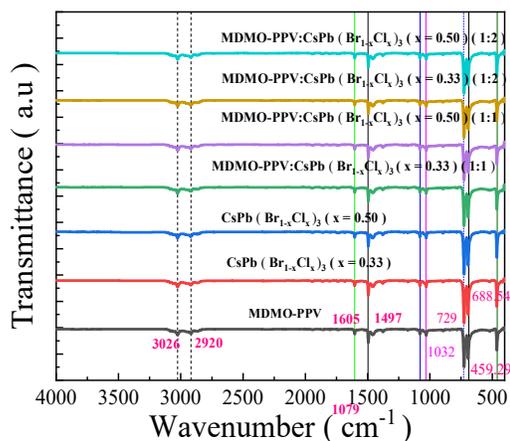


Figure 6.5. FTIR spectra of  $\text{CsPb}(\text{Br}_{1-x}\text{Cl}_x)_3/\text{MDMO-PPV}$  composites solutions as well as pure component (polymer and perovskite).

#### 6.4. Conclusions

In this paper, we illustrated the structure-composition-optical properties (e.g., XRD, UV-vis and FTIR spectra) relationship for the CsPb(Br<sub>1-x</sub>Cl<sub>x</sub>)<sub>3</sub>/MDMO-PPV composites. Resultantly, in the case of a pure CsPb(Br<sub>1-x</sub>Cl<sub>x</sub>)<sub>3</sub> perovskite, depending on the Cl doping amounts, the optical properties could be tuned. Furthermore, when we make a composite by mixing CsPb(Br<sub>1-x</sub>Cl<sub>x</sub>)<sub>3</sub> perovskite and MDMO-PPV polymer, the optical properties were modified although the optical bandgap was dominated the value of MDMO-PPV. Here, the slight difference in optical bandgap between MDMO-PPV and MDMO-PPV/CsPb(Br<sub>1-x</sub>Cl<sub>x</sub>)<sub>3</sub> composite might be from the morphological effects, i.e., MDMO-PPV polymeric chain should be dispersed in the CsPb(Br<sub>1-x</sub>Cl<sub>x</sub>)<sub>3</sub> matrix, resulting in energy levels of MDMO-PPV is more discrete compared to its compact film materials. However, this structure should be helpful from PL emission point of view, demonstrating higher intensity of PL when MDMO-PPV was composited with CsPb(Br<sub>1-x</sub>Cl<sub>x</sub>)<sub>3</sub> perovskite. Therefore, our results open further insight for the use of perovskite/polymer composite, by demonstrating an structural and optical tunability for optoelectronic devices including solar cells and LED display applications.

## Chapter Seven

### 7. Summary and Recommendations

#### 7.1. Summary

Our work in this dissertation was focused on the preparations and characterizations of metal halide perovskite semiconductor materials and their composites. Since metal halide perovskite's remarkable optoelectronic qualities such as its high absorption coefficient, good charge transporting ability, narrow emission line with high PLQY, and tunable optical band gap have drawn interest from the scientific community for study. The ligand systems (olive oil/oleylamine vs. oleic acid/oleylamine) used to synthesize CsPbBr<sub>3</sub> NCs at room temperature were examined for their surface chemistry in Chapter 4. In light of this, the following findings were made: i) both ligand systems showed crystallite sizes in the range of 40–42 nm; ii) both XRD and TEM results demonstrated cuboid shape and band gap of 2.3 eV; iii) FWHM of olive oil/oleylamine was 19 nm, while that of oleic acid/oleylamine was 21 nm, indicating that both were in the desired range for practical application (i.e., 12–42 nm). However, the average PL life time of olive oil/oleylamine is longer than that of oleic acid/oleylamine combined.

Conjugated polymer-perovskite nanocomposites were examined in chapter 5. The present study examines the composite system phase behavior and results of that the ligand-CsPbBr<sub>3</sub> perovskite NCs are not compatible but instead facilitate self-aggregation. This suggests that the MDMO-PPV/oleylamine combination is immiscible. On the other side, MDMO-PPV and two ligand molecules are all soluble in the antisolvent toluene individually, but only after increasing the temperature for MDMO-PPV. However, XRD data shows that crystallites with sizes between 33-52 nm have peaks at (100) and (200) for every composition of MDMO-PPV:CsPbBr<sub>3</sub>. On the other hand, CsPbBr<sub>3</sub>QDs exhibit (110) oriented order, according to TEM data. Moreover, the SEM image demonstrates that aggregation at a 50:50 composite is in line with Flory Huggins' idea as it is theoretically presented. In addition, an increase in PL emission was noted at CsPbBr<sub>3</sub> contents of 30wt% and higher. Finally, EIS measurement demonstrates that the charge transporting

characteristics of the composites (50:50) are enhanced, as evidenced by the decreased resistance of charge transfer in comparison to the pure polymer.

The links between structural-properties-composition were explored in chapter 6. In this, room temperature synthesis was used to produce  $\text{CsPb}(\text{Br}_{1-x}\text{Cl}_x)_3$  and MDMO-PPV, as well as their composites. Microscopy and spectroscopic techniques were then used to analyze the materials. The findings show that, when compared to pure polymer, the composite's crystallite size changes as the chlorine content increased. The optical property shows that when the composite's chlorine concentration rises, the band gap and emission shift accordingly. Lastly, our works demonstrates the usefulness of using olive oil, which is safer for the environment, instead of oleic acid for synthesizing  $\text{CsPbBr}_3$  NCs at RT. Additionally, thermodynamic analysis of miscibility gaps was conducted on the new polymer-ligand-perovskite nanocomposite, MDMO-PPV/toluene, MDMO-PPV with oleylamine, and MDMO-PPV with oleic acid. Future commercialization of  $\text{CsPbBr}_3$  synthesized using olive oil instead of oleic acid, appears promising for optoelectronic applications. Besides, polymer-perovskite composites explorations shows good insight for the improvemnets of properties. Finally the our findings shows that perovskites NCs and polymer-perovskites nanocomposites are promising for the electrochemical and optoelectronic applications.

## **7.2. Recommendations**

The scientific community is interested in metal halide perovskites because of their quick advancement in efficiency when compared to more established organic and inorganic materials, as demonstrated by their characterization and development. To obtain the desired materials for practical applications, the characteristics still need to be improved. In this study, the surface chemistry of  $\text{CsPbBr}_3$  was examined firstly. Next, the miscibility, structural, and some properties of conjugated polymer-perovskite nanocomposites were explored. Because there were no instruments for device fabrication, efficiency measurements and additional properties investigations, the study has been restricted to ascertain spectroscopy and microscopy and explored. Due to the limitations of the tools, we strongly reommeded researchers to carry out further study in the future based on the current explorations.

## References

1. De Almeida, A.; Santos, B.; Bertoldi, P.; Quicheron, M. Solid State Lighting Review - Potential and Challenges in Europe. *Renew. Sustain. Energy Rev.* **2014**, *34*, 30–48, doi:10.1016/j.rser.2014.02.029.
2. Adjokatse, S.; Fang, H.H.; Loi, M.A. Broadly Tunable Metal Halide Perovskites for Solid-State Light-Emission Applications. *Mater. Today* **2017**, *20*, 413–424.
3. Goel, P.; Sundriyal, S.; Shrivastav, V.; Mishra, S.; Dubal, D.P.; Kim, K.H.; Deep, A. Perovskite Materials as Superior and Powerful Platforms for Energy Conversion and Storage Applications. *Nano Energy* **2021**, *80*, 105552, doi:10.1016/j.nanoen.2020.105552.
4. Rogach, A.L. Towards next Generation White LEDs: Optics-Electronics Synergistic Effect in a Single-Layer Heterophase Halide Perovskite. *Light Sci. Appl.* **2021**, *10*, 46, doi:10.1038/s41377-021-00488-8.
5. Mohapatra, A.; Kar, M.R.; Bhaumik, S. Recent Progress and Prospects on Metal Halide Perovskite Nanocrystals as Color Converters in the Fabrication of White Light-Emitting Diodes. *Front. Electron. Mater.* **2022**, *2*, 891983, doi:10.3389/femat.2022.891983.
6. Han, T.H.; Jang, K.Y.; Dong, Y.; Friend, R.H.; Sargent, E.H.; Lee, T.W. A Roadmap for the Commercialization of Perovskite Light Emitters. *Nat. Rev. Mater.* **2022**, *7*, 757–777, doi:10.1038/s41578-022-00459-4.
7. Pode, R. Organic Light Emitting Diode Devices : An Energy Efficient Solid State Lighting for Applications. *Renew. Sustain. Energy Rev.* **2020**, *133*, 110043, doi:10.1016/j.rser.2020.110043.
8. Luo, D.; Chen, Q.; Liu, B.; Qiu, Y. Emergence of Flexible White Organic Light-Emitting Diodes. *Polymers (Basel)*. **2019**, *11*, 384, doi:10.3390/POLYM11020384.

9. Yu, Y.; Tang, Y.; Wang, B.; Zhang, K.; Tang, J.-X.; Li, Y.-Q. Red Perovskite Light Emitting Diode: Recent Advances and Perspectives. *Laser Photon. Rev.* **2023**, *17*, 2200608, doi:10.1002/lpor.202200608.
10. Kumar, S.A.; Shankar, J.S.; Periyasamy, B.K.; Nayak, S.K. Device Engineering Aspects of Organic Light- Emitting Diodes ( OLEDs ). *Polym. Technol. Mater.* **2019**, *58*, 1597–1624, doi:10.1080/25740881.2018.1563133.
11. Peng, H.; Sun, X.; Weng, W.; Fang, X. *Polymer Materials for Energy and Electronic Applications*; Academic press, 2016; ISBN 9780128110928.
12. Yee, J.; Merican, Z.; Merican, A.; Falalu, M. Polymer Light Emitting Diodes ( PLEDs ): An Update Review on Current Innovation and Performance of Material Properties. *Mater. Today Proc.* **2019**, *16*, 1909–1918, doi:10.1016/j.matpr.2019.06.068.
13. Babu, D.P.; Kumar, S.N.; Kumar, N.S.; Naidu, K.C.B.; Basha, D.B. Applications of Polymer Light-Emitting Devices and Displays. *Polym. Light. Devices Displays* **2020**, 1–28, doi:10.1002/9781119654643.ch1.
14. Liu, J.P.; Qu, S.C.; Zeng, X.B.; Xu, Y.; Gou, X.F.; Wang, Z.J.; Zhou, H.Y.; Wang, Z.G. Fabrication of ZnO and Its Enhancement of Charge Injection and Transport in Hybrid Organic / Inorganic Light Emitting Devices. *Appl. Surf. Sci.* **2007**, *253*, 7506–7509, doi:10.1016/j.apsusc.2007.03.043.
15. Cao, W.; Xiang, C.; Yang, Y.; Chen, Q.; Chen, L. Highly Stable QLEDs with Improved Hole Injection via Quantum Dot Structure Tailoring. *Nat. Commun.* **2018**, *9*, 2608, doi:10.1038/s41467-018-04986-z.
16. Lee, K.H.; Lee, J.H.; Song, W.S.; Ko, H.; Lee, C.; Lee, J.H.; Yang, H. Highly Efficient, Color-Pure, Color-Stable Blue Quantum Dot Light-Emitting Devices. *ACS Nano* **2013**, *7*, 7295–7302, doi:10.1021/nn402870e.
17. Yang, Y.; Zheng, Y.; Cao, W.; Titov, A.; Hyvonen, J.; Manders, J.R.; Xue, J.; Holloway, P.H.; Qian, L. High-Efficiency Light-Emitting Devices Based on Quantum Dots with Tailored Nanostructures. *Nat. Photonics* **2015**, *9*, 259–266, doi:10.1038/nphoton.2015.36.
18. Kovalenko, M. V; Protesescu, L.; Bodnarchuk, M.I. Properties and Potential Optoelectronic Applications of Lead Halide Perovskite Nanocrystals. *Science* **2017**, *358*, 745–750.

19. Lu, M.; Zhang, Y.; Wang, S.; Guo, J.; Yu, W.W.; Rogach, A.L. Metal Halide Perovskite Light-Emitting Devices: Promising Technology for Next-Generation Displays. *Adv. Funct. Mater.* **2019**, *29*, 1902008, doi:10.1002/adfm.201902008.
20. Sutherland, B.R.; Sargent, E.H. Perovskite Photonic Sources. *Nat. Photonics* **2016**, *10*, 295–302, doi:10.1038/nphoton.2016.62.
21. Zhao, Y.; Zhu, K. Organic-Inorganic Hybrid Lead Halide Perovskites for Optoelectronic and Electronic Applications. *Chem. Soc. Rev.* **2016**, *45*, 655–689, doi:10.1039/c4cs00458b.
22. Veldhuis, S.A.; Boix, P.P.; Yantara, N.; Li, M.; Sum, T.C.; Mathews, N.; Mhaisalkar, S.G. Perovskite Materials for Light-Emitting Diodes and Lasers. *Adv. Mater.* **2016**, *28*, 6804–6834, doi:10.1002/adma.201600669.
23. Zhou, Y.; Mora-Seró, I. *Halide Perovskite Semiconductors: Structures, Characterization, Properties, and Phenomena.*; John Wiley & Sons, 2016; ISBN 2013206534.
24. Van Le, Q.; Jang, H.W.; Kim, S.Y. Recent Advances toward High-Efficiency Halide Perovskite Light-Emitting Diodes: Review and Perspective. *Small Methods* **2018**, *2*, 1700419, doi:10.1002/smtd.201700419.
25. Lu, P.; Lu, M.; Wang, H.; Sui, N.; Shi, Z.; Yu, W.W. Metal Halide Perovskite Nanocrystals and Their Applications in Optoelectronic Devices. **2019**, 430–459, doi:10.1002/inf2.12031.
26. Wang, Y.; Ding, G.; Mao, J.Y.; Zhou, Y.; Han, S.T. Recent Advances in Synthesis and Application of Perovskite Quantum Dot Based Composites for Photonics, Electronics and Sensors. *Sci. Technol. Adv. Mater.* **2020**, *21*, 278–302, doi:10.1080/14686996.2020.1752115.
27. Guner, T.; Demir, M.M. A Review on Halide Perovskites as Color Conversion Layers in White Light Emitting Diode Applications. *Phys. Status Solidi Appl. Mater. Sci.* **2018**, *215*, 1800120, doi:10.1002/pssa.201800120.
28. He, X.; Qiu, Y.; Yang, S. Fully-Inorganic Trihalide Perovskite Nanocrystals: A New Research Frontier of Optoelectronic Materials. *Adv. Mater.* **2017**, *29*, 1700775, doi:10.1002/adma.201700775.

29. Chen, D.; Zhou, S.; Tian, F.; Ke, H.; Jiang, N.; Wang, S.; Peng, Y.; Liu, Y. Halogen-Hot-Injection Synthesis of Mn-Doped CsPb(Cl/Br)<sub>3</sub> Nanocrystals with Blue/Orange Dual-Color Luminescence and High Photoluminescence Quantum Yield. *Adv. Opt. Mater.* **2019**, *7*, 1901082, doi:10.1002/adom.201901082.
30. Liu, M.; Matuhina, A.; Zhang, H.; Vivo, P. Advances in the Stability of Halide Perovskite Nanocrystals. *Materials (Basel)*. **2019**, *12*, 3733, doi:10.3390/ma12223733.
31. Van Embden, J.; Chesman, A.S.R.; Jasieniak, J.J. The Heat-up Synthesis of Colloidal Nanocrystals. *Chem. Mater.* **2015**, *27*, 2246–2285, doi:10.1021/cm5028964.
32. Liu, Y.; Guo, M.; Dong, S.; Jiao, X.; Wang, T.; Chen, D. Room Temperature Colloidal Synthesis of CsPbBr<sub>3</sub> Nanowires with Tunable Length, Width and Composition. *J. Mater. Chem. C* **2018**, *6*, 7797–7802, doi:10.1039/c8tc02636j.
33. Ding, H.; Jiang, H.; Wang, X. How Organic Ligands Affect the Phase Transition and Fluorescent Stability of Perovskite Nanocrystals. *J. Mater. Chem. C* **2020**, *8*, 8999–9004, doi:10.1039/d0tc01028f.
34. Chouhan, L.; Ghimire, S.; Subrahmanyam, C.; Miyasaka, T.; Biju, V. Synthesis, Optoelectronic Properties and Applications of Halide Perovskites. *Chem. Soc. Rev.* **2020**, *49*, 2869–2885, doi:10.1039/c9cs00848a.
35. Wang, Z.; Shi, Z.; Li, T.; Chen, Y.; Huang, W. Stability of Perovskite Solar Cells: A Prospective on the Substitution of the A Cation and X Anion Angewandte. **2017**, 1190–1212, doi:10.1002/anie.201603694.
36. Kojima, A.; Teshima, K.; Shirai, Y.; Miyasaka, T. Organometal Halide Perovskites as Visible-Light Sensitizers for Photovoltaic Cells. *J. Am. Chem. Soc.* **2009**, *131*, 6050–6051, doi:10.1021/ja809598r.
37. Shamsi, J.; Urban, A.S.; Imran, M.; De Trizio, L.; Manna, L. Metal Halide Perovskite Nanocrystals: Synthesis, Post-Synthesis Modifications, and Their Optical Properties. *Chem. Rev.* **2019**, *119*, 3296–3348, doi:10.1021/acs.chemrev.8b00644.
38. Song, J.; Li, J.; Li, X.; Xu, L.; Dong, Y.; Zeng, H. Quantum Dot Light-Emitting Diodes Based on Inorganic Perovskite Cesium Lead Halides (CsPbX<sub>3</sub>). *Adv. Mater.* **2015**, *27*, 7162–7167, doi:10.1002/adma.201502567.

39. Zhang, L.; Yang, X.; Jiang, Q.; Wang, P.; Yin, Z.; Zhang, X.; Tan, H.; Yang, Y.M.; Wei, M.; Sutherland, B.R.; et al. Ultra-Bright and Highly Efficient Inorganic Based Perovskite Light-Emitting Diodes. *Nat. Commun.* **2017**, *8*, 15640, doi:10.1038/ncomms15640.
40. Protesescu, L.; Yakunin, S.; Bodnarchuk, M.I.; Krieg, F.; Caputo, R.; Hendon, C.H.; Yang, R.X.; Walsh, A.; Kovalenko, M. V. Nanocrystals of Cesium Lead Halide Perovskites (CsPbX<sub>3</sub>, X = Cl, Br, and I): Novel Optoelectronic Materials Showing Bright Emission with Wide Color Gamut. *Nano Lett.* **2015**, *15*, 3692–3696, doi:10.1021/nl5048779.
41. Fang, T.; Wang, T.; Li, X.; Dong, Y.; Bai, S.; Song, J. Perovskite QLED with an External Quantum Efficiency of over 21% by Modulating Electronic Transport. *Sci. Bull.* **2021**, *66*, 36–43, doi:10.1016/j.scib.2020.08.025.
42. Huang, C.Y.; Zou, C.; Mao, C.; Corp, K.L.; Yao, Y.C.; Lee, Y.J.; Schlenker, C.W.; Jen, A.K.Y.; Lin, L.Y. CsPbBr<sub>3</sub> Perovskite Quantum Dot Vertical Cavity Lasers with Low Threshold and High Stability. *ACS Photonics* **2017**, *4*, 2281–2289, doi:10.1021/acsp Photonics.7b00520.
43. Chen, C.; Lin, Y.; Yang, Y.; Chiang, Y.; Li, Z.; Yip, H.; Chen, W.; Chueh, C. Improving the Performance of All-Inorganic Perovskite Light-Emitting Diodes through Using Polymeric Interlayers with a Pendant Design. *Mater. Chem. Front.* **2021**, 7199–7207, doi:10.1039/d1qm01027a.
44. Qaid, S.M.H.; Al-asbahi, B.A.; Ghaithan, H.M.; Alsalhi, M.S.; Al, A.S. Optical and Structural Properties of CsPbBr<sub>3</sub> Perovskite Quantum Dots / PFO Polymer Composite Thin Films. *J. Colloid Interface Sci.* **2020**, *563*, 426–434, doi:10.1016/j.jcis.2019.12.094.
45. Aljaafreh, M.J.; Prasad, S.; Alsalhi, M.S.; Lemmer, U.; Alahmed, Z.A.; Ali, M. Emission Dynamics of Conjugated Oligomer ( BECV-DHF )/ Quantum Dot Perovskite ( CsPbBr<sub>3</sub> ) Composites in Solutions. *Colloids Surfaces A Physicochem. Eng. Asp.* **2021**, *610*, 125911, doi:10.1016/j.colsurfa.2020.125911.
46. Luo, D.; Chen, Q.; Qiu, Y.; Zhang, M.; Liu, B. Device Engineering for All-Inorganic Perovskite Light-Emitting Diodes. *Nanomaterials* **2019**, *9*, 1007.

47. Cao, M.; Xu, Y.; Li, P.; Zhong, Q.; Yang, D.; Zhang, Q. Recent Advances and Perspectives on Light Emitting Diodes Fabricated from Halide Metal Perovskite Nanocrystals. *J. Mater. Chem. C* **2019**, *7*, 14412–14440, doi:10.1039/c9tc03978c.
48. Kumawat, N.K.; Liu, X.K.; Kabra, D.; Gao, F. Blue Perovskite Light-Emitting Diodes: Progress, Challenges and Future Directions. *Nanoscale* **2019**, *11*, 2109–2120, doi:10.1039/c8nr09885a.
49. Chen, Z.; Li, Z.; Hopper, T.R.; Bakulin, A.A.; Yip, H. Materials, Photophysics and Device Engineering of Perovskite Light-Emitting Diodes. *Rep. Prog. Phys.* **2021**, *84*, 046401.
50. Fan, X.; Zhang, M.; Wang, X.; Yang, F.; Meng, X. Recent Progress in Organic-Inorganic Hybrid Solar Cells. *J. Mater. Chem. A* **2013**, *1*, 8694–8709, doi:10.1039/c3ta11200d.
51. Shin, M.J.; Gwon, D.O.; Lee, G.S.; Ahn, H.S.; Yi, S.N.; Ha, D.H. Fabrication of N-GaN/MDMO-PPV Hybrid Structures for Optoelectronic Devices. *J. Lumin.* **2014**, *147*, 1–4, doi:10.1016/j.jlumin.2013.10.042.
52. Shankar, J.S.; Kumar, S.A.; Periyasamy, B.K. Studies on Optical Characteristics of Multicolor Emitting MEH-PPV / ZnO Hybrid Nanocomposite. *Polym. Plast. Technol. Eng.* **2018**, *58*, 148–157, doi:10.1080/03602559.2018.1466171.
53. Salcedo-Reyes, J.-C.; Vásquez-Rojas, J.-R.; Jiménez-Borrego, L.-C.; Castañeda-Uribe, O.-A.; Méndez-Pinzón, H.-A. Improving Extraction Efficiency of OLEDs by a Luminescent Polymer Embedded in a Colloidal Crystal Matrix. *Semicond. Sci. Technol.* **2019**, *34*, 115016.
54. Al-Asbahi, B.A. Influence of Anatase Titania Nanoparticles Content on Optical and Structural Properties of Amorphous Silica. *Mater. Res. Bull.* **2017**, *89*, 286–291, doi:10.1016/j.materresbull.2017.01.004.
55. Al-Asbahi, B.A. Influence of SiO<sub>2</sub>/TiO<sub>2</sub> Nanocomposite on the Optoelectronic Properties of PFO/MEH-PPV-Based OLED Devices. *Polymers (Basel)*. **2018**, *10*, 800, doi:10.3390/polym10070800.
56. Ibrahim, I.M.; Sharhan, S.I. Enhancement of MEH-PPV by Introducing Anatase TiO<sub>2</sub> Nanoparticles for Oled Device. *Dig. J. Nanomater. Biostructures* **2019**, *14*, 93–100.

57. Shen, H.; Lin, Q.; Cao, W.; Yang, C.; Shewmon, N.T.; Wang, H.; Niu, J.; Li, L.S.; Xue, J. Efficient and Long-Lifetime Full-Color Light-Emitting Diodes Using High Luminescence Quantum Yield Thick-Shell Quantum Dots. *Nanoscale* **2017**, *9*, 13583–13591, doi:10.1039/c7nr04953f.
58. Tan, Z.; Moghaddam, R.S.; Lai, M.L.; Docampo, P.; Higler, R.; Price, M.; Sadhanala, A.; Pazos, L.M.; Credgington, D.; Hanusch, F.; et al. Bright Light - Emitting Diodes Based on Organometal Halide Perovskite. *Nat. Nanotechnol.* **2014**, *9*, 687–692.
59. Hu, Y.; Shu, J.; Zhang, X.; Zhao, A.; Liu, Y.; Li, R.; Di, Y.; Xu, H.; Gan, Z. Encapsulation of Colloid Perovskite Nanocrystals into Solid Polymer Matrices: Impact on Electronic Transition and Photoluminescence. *J. Lumin.* **2020**, *219*, 116938, doi:10.1016/j.jlumin.2019.116938.
60. Song, L.; Guo, X.; Hu, Y.; Lv, Y.; Lin, J.; Liu, Z.; Fan, Y.; Liu, X. Efficient Inorganic Perovskite Light-Emitting Diodes with Polyethylene Glycol Passivated Ultrathin CsPbBr<sub>3</sub> Films. *J. Phys. Chem. Lett.* **2017**, *8*, 4148–4154, doi:10.1021/acs.jpcclett.7b01733.
61. Huang, H.; Bodnarchuk, M.I.; Kershaw, S. V.; Kovalenko, M. V.; Rogach, A.L. Lead Halide Perovskite Nanocrystals in the Research Spotlight: Stability and Defect Tolerance. *ACS Energy Lett.* **2017**, *2*, 2071–2083, doi:10.1021/acsenerylett.7b00547.
62. Chen, L.C.; Tien, C.H.; Tseng, Z.L.; Dong, Y.S.; Yang, S. Influence of PMMA on All-Inorganic Halide Perovskite CsPbBr<sub>3</sub> Quantum Dots Combined with Polymer Matrix. *Materials (Basel)*. **2019**, *12*, 985, doi:10.3390/ma12060985.
63. Jiang, D.H.; Tsai, Y.H.; Veeramuthu, L.; Liang, F.C.; Chen, L.C.; Lin, C.C.; Satoh, T.; Tung, S.H.; Kuo, C.C. Novel Ultra-Stable and Highly Luminescent White Light-Emitting Diodes from Perovskite Quantum Dots - Polymer Nanofibers through Biaxial Electrospinning. *APL Mater.* **2019**, *7*, doi:10.1063/1.5124880.
64. Liang, S.; Zhang, M.; Biesold, G.M.; Choi, W.; He, Y.; Li, Z.; Shen, D.; Lin, Z. Recent Advances in Synthesis, Properties, and Applications of Metal Halide Perovskite Nanocrystals/Polymer Nanocomposites. *Adv. Mater.* **2021**, *33*, 2005888, doi:10.1002/adma.202005888.

65. Ferrell, W.H.; Kushner, D.I.; Hickner, M.A. Investigation of Polymer–Solvent Interactions in Poly(Styrene Sulfonate) Thin Films. *J. Polym. Sci. Part B Polym. Phys.* **2017**, *55*, 1365–1372, doi:10.1002/polb.24383.
66. Walsh, D.J.; Rostami, S. The Miscibility of High Polymers: The Role of Specific Interactions. **1985**, 119–169, doi:10.1007/3-540-15481-7\_9.
67. Zeman, L.; Patterson, D. Effect of the Solvent on Polymer Incompatibility in Solution. *Macromolecules* **1972**, *5*, 513–516, doi:10.1021/ma60028a030.
68. Prakash, A.; Katiyar, M. Correlation between Electroluminescence, Charge Transport and Photophysical Properties of Polymer Blends. *Synth. Met.* **2017**, *223*, 184–191, doi:10.1016/j.synthmet.2016.11.019.
69. Bajpai, M.; Srivastava, R.; Kamalasanan, M.N.; Tiwari, R.S.; Chand, S. Charge Transport and Microstructure in PFO:MEH-PPV Polymer Blend Thin Films. *Synth. Met.* **2010**, *160*, 1740–1744, doi:10.1016/j.synthmet.2010.06.010.
70. Brahmi, C.; Benlifa, M.; Vaultot, C.; Michelin, L.; Dumur, F.; Airoudj, A.; Morlet-Savary, F.; Raveau, B.; Bousselmi, L.; Lalevée, J. New Hybrid Perovskites/Polymer Composites for the Photodegradation of Organic Dyes. *Eur. Polym. J.* **2021**, *157*, 110641, doi:10.1016/j.eurpolymj.2021.110641.
71. Privitera, A.; Righetto, M.; De Bastiani, M.; Carraro, F.; Rancan, M.; Armelao, L.; Granozzi, G.; Bozio, R.; Franco, L. Hybrid Organic/Inorganic Perovskite-Polymer Nanocomposites: Toward the Enhancement of Structural and Electrical Properties. *J. Phys. Chem. Lett.* **2017**, *8*, 5981–5986, doi:10.1021/acs.jpcclett.7b03077.2017.
72. Sun, X.; Zhang, F.; Zhang, L.; Liu, G.; Wang, Y.; Wang, Y.; Deng, Y. Enhanced Electromechanical Conversion via in Situ Grown CsPbBr<sub>3</sub> Nanoparticle/Poly(Vinylidene Fluoride) Fiber Composites for Physiological Signal Monitoring. *Soft Sci.* **2022**, *2*, 21, doi:10.20517/ss.2021.21.
73. Purabgola, A.; Kandasubramanian, B. *Hybrid Perovskite Composite Materials: Design to Applications*; Elsevier Ltd., **2020**; ISBN 9780128199770.

74. Perulli, A.; Balena, A.; Fernandez, M.; Nedelcu, G.; Cretu, A.; Kovalenko, M. V.; Lomascolo, M.; Anni, M. Full-Color Tuning in Binary Polymer : Perovskite Nanocrystals Organic- Inorganic Hybrid Blends. *Appl. Phys. Lett.* **2018**, *112*, 171904, doi:10.1063/1.5020201.
75. Wu, Y.; Wei, H.; Xu, L.; Cao, B.; Zeng, H. Progress and Perspective on CsPbX<sub>3</sub>nanocrystals for Light Emitting Diodes and Solar Cells. *J. Appl. Phys.* 2020, *128*, 050903.
76. Peng, S.; Wang, S.; Zhao, D.; Li, X.; Liang, C.; Xia, J. Pure Bromide-Based Perovskite Nanoplatelets for Blue Light-Emitting Diodes. *Small Methods* **2019**, *3*, 1900196, doi:10.1002/smtd.201900196.
77. Cheng, M.; Jiang, J.; Yan, C.; Lin, Y.; Mortazavi, M.; Kaul, A.B.; Jiang, Q. Progress and Application of Halide Perovskite Materials for Solar Cells and Light Emitting Devices. *Nanomaterials* **2024**, *14*, 391.
78. Wei, Z.; Xing, J. The Rise of Perovskite Light-Emitting Diodes. *J. Phys. Chem. Phys. Chem. Lett.* **2019**, 3035–3042, doi:10.1021/acs.jpcclett.9b00277.
79. Li, D.; Chen, C.S.; Wu, Y.H.; Zhu, Z.G.; Shih, W.Y.; Shih, W.H. Improving Stability of Cesium Lead Iodide Perovskite Nanocrystals by Solution Surface Treatments. *ACS Omega* **2020**, *5*, 18013–18020, doi:10.1021/acsomega.0c01403.
80. Rudd, P.N.; Huang, J. Metal Ions in Halide Perovskite Materials and Devices. *Trends Chem.* **2019**, *1*, 394–409.
81. Schileo, G.; Grancini, G. Halide Perovskites: Current Issues and New Strategies to Push Material and Device Stability. *JPhys Energy* **2020**, *2*, 021005, doi:10.1088/2515-7655/ab6cc4.
82. Li, Y.; Zhang, X.; Huang, H.; Kershaw, S. V; Rogach, A.L. Advances in Metal Halide Perovskite Nanocrystals : Synthetic Strategies , Growth Mechanisms , and Optoelectronic Applications. *Mater. Today* **2019**, 007, doi:10.1016/j.mattod.2019.06.007.
83. Era, M.; Morimoto, S.; Tsutsui, T.; Saito, S. Organic-Inorganic Heterostructure Electroluminescent Device Using a Layered Perovskite Semiconductor (C<sub>6</sub>H<sub>5</sub>C<sub>2</sub>H<sub>4</sub>NH<sub>3</sub>)<sub>2</sub>PbI<sub>4</sub>. *Appl. Phys. Lett.* **1994**, *65*, 676–678, doi:10.1063/1.112265.

84. Sun, Q.; Yin, W. Thermodynamic Stability Trend of Cubic Perovskites. *J. Am. Chem. Soc.* **2017**, *139*, 14905–14908, doi:10.1021/jacs.7b09379.
85. Zou, Y.; Yuan, Z.; Bai, S.; Gao, F.; Sun, B. Recent Progress toward Perovskite Light-Emitting Diodes with Enhanced Spectral and Operational Stability. *Mater. Today Nano* **2019**, *5*, 100028, doi:10.1016/j.mtnano.2019.100028.
86. Yong, Z.J.; Guo, S.Q.; Ma, J.P.; Zhang, J.Y.; Li, Z.Y.; Chen, Y.M.; Zhang, B. Bin; Zhou, Y.; Shu, J.; Gu, J.L.; et al. Doping-Enhanced Short-Range Order of Perovskite Nanocrystals for Near-Unity Violet Luminescence Quantum Yield. *J. Am. Chem. Soc.* **2018**, *140*, 9942–9951, doi:10.1021/jacs.8b04763.
87. Yao, E.; Yang, Z.; Meng, L.; Sun, P.; Dong, S.; Yang, Y.; Yang, Y. High-Brightness Blue and White LEDs Based on Inorganic Perovskite Nanocrystals and Their Composites. *Adv. Mater.* **2017**, *29*, 1606859, doi:10.1002/adma.201606859.
88. Sim, K.; Jun, T.; Bang, J.; Kamioka, H.; Kim, J.; Hiramatsu, H.; Hosono, H. Performance Boosting Strategy for Perovskite Light-Emitting Diodes. *Appl. Phys. Rev.* **2019**, *6*, 031402, doi:10.1063/1.5098871.
89. Chiba, T.; Hoshi, K.; Pu, Y.J.; Takeda, Y.; Hayashi, Y.; Ohisa, S.; Kawata, S.; Kido, J. High-Efficiency Perovskite Quantum-Dot Light-Emitting Devices by Effective Washing Process and Interfacial Energy Level Alignment. *ACS Appl. Mater. Interfaces* **2017**, *9*, 18054–18060, doi:10.1021/acsami.7b03382.
90. Quarta, D.; Imran, M.; Capodilupo, A.L.; Petralanda, U.; Van Beek, B.; De Angelis, F.; Manna, L.; Infante, I.; De Trizio, L.; Giansante, C. Stable Ligand Coordination at the Surface of Colloidal CsPbBr<sub>3</sub> Nanocrystals. *J. Phys. Chem. Lett.* **2019**, *10*, 3715–3726, doi:10.1021/acs.jpcclett.9b01634.
91. De Trizio, L.; Infante, I.; Manna, L. Surface Chemistry of Lead Halide Perovskite Colloidal Nanocrystals. *Acc. Chem. Res.* **2023**, *56*, 1815–1825, doi:10.1021/acs.accounts.3c00174.
92. Dutt, V.G.V.; Akhil, S.; Mishra, N. Surface Passivation Strategies for Improving Photoluminescence and Stability of Cesium Lead Halide Perovskite Nanocrystals. *ChemNanoMat* **2020**, *6*, 1730–1742, doi:10.1002/cnma.202000495.

93. Wang, Y.P.; Li, H.C.; Huang, Y.C.; Tan, C.S. Synthesis and Applications of Halide Perovskite Nanocrystals in Optoelectronics. *Inorganics* **2023**, *11*, 39, doi:10.3390/inorganics11010039.
94. Li, G.; Huang, J.; Zhu, H.; Li, Y.; Tang, J.X.; Jiang, Y. Surface Ligand Engineering for Near-Unity Quantum Yield Inorganic Halide Perovskite QDs and High-Performance QLEDs. *Chem. Mater.* **2018**, *30*, 6099–6107, doi:10.1021/acs.chemmater.8b02544.
95. Fanizza, E.; Cascella, F.; Altamura, D.; Giannini, C.; Panniello, A.; Triggiani, L.; Panzarea, F.; Depalo, N.; Grisorio, R.; Suranna, G.P.; et al. Post-Synthesis Phase and Shape Evolution of CsPbBr<sub>3</sub> Colloidal Nanocrystals: The Role of Ligands. *Nano Res.* **2019**, *12*, 1155–1166, doi:10.1007/s12274-019-2371-2.
96. Chen, K.; Wang, C.; Peng, Z.; Qi, K.; Guo, Z.; Zhang, Y.; Zhang, H. The Chemistry of Colloidal Semiconductor Nanocrystals: From Metal-Chalcogenides to Emerging Perovskite. *Coord. Chem. Rev.* **2020**, *418*, 213333, doi:10.1016/j.ccr.2020.213333.
97. Fiuza-Maneiro, N.; Sun, K.; López-Fernández, I.; Gómez-Graña, S.; Müller-Buschbaum, P.; Polavarapu, L. Ligand Chemistry of Inorganic Lead Halide Perovskite Nanocrystals. *ACS Energy Lett.* **2023**, *8*, 1152–1191, doi:10.1021/acsenergylett.2c02363.
98. Zhang, B.; Goldoni, L.; Zito, J.; Dang, Z.; Almeida, G.; Zaccaria, F.; De Wit, J.; Infante, I.; De Trizio, L.; Manna, L. Alkyl Phosphonic Acids Deliver CsPbBr<sub>3</sub> Nanocrystals with High Photoluminescence Quantum Yield and Truncated Octahedron Shape. *Chem. Mater.* **2019**, *31*, 9140–9147, doi:10.1021/acs.chemmater.9b03529.
99. Jenkins, S. *Hansen Solubility Parameters: Auser's Handbook*; 2007; ISBN 9780849372483.
100. Iwao, T. *Polymer Solutions: An Introduction to Physical Properties*; Wiley-Interscience: Interscience, 2002; ISBN 2013206534.
101. Caddeo, C.; Ackermann, J.; Mattoni, A. A Theoretical Perspective on the Thermodynamic Stability of Polymer Blends for Solar Cells: From Experiments to Predictive Modeling. *Sol. RRL* **2022**, *6*, 2200172, doi:10.1002/solr.202200172.

102. Awol, N.; Amente, C.; Verma, G.; Kim, J.Y. Morphology and Surface Analyses for CH<sub>3</sub>NH<sub>3</sub>PbI<sub>3</sub>perovskite Thin Films Treated with Versatile Solvent-Antisolvent Vapors. *RSC Adv.* **2021**, *11*, 17789–17799, doi:10.1039/d1ra02645c.
103. Awol, N.; Amente, C.; Verma, G.; Kim, J.Y. A Versatile Lead Iodide Particle Synthesis and Film Surface Analysis for Optoelectronics. *J. Alloys Compd.* **2020**, *829*, 154486, doi:10.1016/j.jallcom.2020.154486.
104. Qaid, S.M.H.; Ghaithan, H.M.; Al-asbahi, B.A.; Aldwayyan, A.S. Ultra-Stable Polycrystalline CsPbBr<sub>3</sub> Perovskite – Polymer Composite Thin Disk for Light-Emitting Applications. *nanomaterials* **2020**, *10*, 2382, doi:10.3390/nano10122382.
105. Wang, Z.; Fu, R.; Li, F.; Xie, H.; He, P.; Sha, Q.; Tang, Z.; Wang, N.; Zhong, H. One-Step Polymeric Melt Encapsulation Method to Prepare CsPbBr<sub>3</sub> Perovskite Quantum Dots/Polymethyl Methacrylate Composite with High Performance. *Adv. Funct. Mater.* **2021**, *31*, 2010009, doi:10.1002/adfm.202010009.
106. Yang, L.; Fu, B.; Li, X.; Chen, H.; Li, L. Poly(Vinylidene Fluoride)-Passivated CsPbBr<sub>3</sub>perovskite Quantum Dots with near-Unity Photoluminescence Quantum Yield and Superior Stability. *J. Mater. Chem. C* **2021**, *9*, 1983–1991, doi:10.1039/d0tc05103a.
107. Li, Y.T.; Prakoso, S.P.; Hsu, L.C.; Xu, X.N.; Hung, C.C.; Chen, Y.L.; Wu, Y.H.; Chen, W.C.; Lin, B.H.; Chiu, Y.C. Controlled Growth of Highly Oriented Perovskite Crystals in Polymer Solutions via Selective Solvent Vapor Diffusion. *Macromol. Rapid Commun.* **2023**, *44*, 2300382, doi:10.1002/marc.202300382.
108. Veeramuthu, L.; Liang, F.; Zhang, Z.; Cho, C.; Ercan, E. Improving the Performance and Stability of Perovskite Light- Emitting Diodes by a Polymeric Nanothick Interlayer-Assisted Grain Control Process. **2020**, *5*, 8972–898, doi:10.1021/acsomega.0c00758.
109. Masi, S.; Colella, S.; Listorti, A.; Roiati, V.; Liscio, A.; Palermo, V.; Rizzo, A.; Gigli, G. Growing Perovskite into Polymers for Easy-Processable Optoelectronic Devices. *Sci. Rep.* **2015**, *5*, 7725, doi:10.1038/srep07725.

110. Chikalova-Luzina, O.P.; Aleshin, A.N.; Shcherbakov, I.P.; Vyatkin, V.M.; Matyushkin, L.B. Energy Transfer in Hybrid Optoelectronic Structures between Perovskite Nanocrystals and an Organic Matrix. *Synth. Met.* **2018**, *246*, 230–235, doi:10.1016/j.synthmet.2018.11.001.
111. Lin, C.; Chen, P.; Xiong, Z.; Liu, D. Interfacial Engineering with Ultrathin Poly for High Efficient Perovskite Light-Emitting Diodes. *Nanotechnology* **2018**, *29*, 075203.
112. Qaid, S.M.H.; Al-Asbahi, B.A.; Ghaithan, H.M.; Aldwayyan, A.S. Tuning the Optical Properties of MeH–Ppv/Pfo Hybrid Thin Films via the Incorporation of Cspbbr3 Quantum Dots. *Coatings* **2021**, *11*, 154, doi:10.3390/coatings11020154.
113. Galindo, L.A.; Gozzi, G.; Fugikawa-Santos, L.; Faria, R.M.; Lavarda, F.C.; Batagin-Neto, A. Investigation of the Polymer-Salt Interactions in Polymeric Light Emitting Electrochemical Cells: Electronic Structure Calculations and Experimental Studies. *Org. Electron.* **2020**, *79*, 105629, doi:10.1016/j.orgel.2020.105629.
114. Xin, Y.; Zhao, H.; Zhang, J. Highly Stable and Luminescent Perovskite-Polymer Composites from a Convenient and Universal Strategy. *ACS Appl. Mater. Interfaces* **2018**, *10*, 4971–4980, doi:10.1021/acsami.7b16442.
115. Tan, Y.; Zou, Y.; Wu, L.; Huang, Q.; Yang, D.; Chen, M.; Ban, M.; Wu, C.; Wu, T.; Bai, S.; et al. Highly Luminescent and Stable Perovskite Nanocrystals with Octylphosphonic Acid as a Ligand for Efficient Light-Emitting Diodes. *ACS Appl. Mater. Interfaces* **2018**, *10*, 3784–3792, doi:10.1021/acsami.7b17166.
116. Xu, H.; Wang, J.; Xuan, T.; Lv, C.; Hou, J.; Zhang, L.; Dong, Y.; Shi, J. Convenient and Large-Scale Synthesis of High-Quality, All-Inorganic Lead Halide Perovskite Nanocrystals for White Light-Emitting Diodes. *Chem. Eng. J.* **2019**, *364*, 20–27, doi:10.1016/j.cej.2019.01.152.
117. Al-Asbahi, B.A.; Saif M. H. Qaid; Aldwayyan, A.S. Triplet Energy Transfer Mechanism of Ternary Organic Hybrid Thin Films PFO-MEH-PPV-CsPbBr3 Perovskite Quantum Dots. *Nanomaterials* **2020**, *10*, 2094, doi:doi:10.3390/nano10112094.
118. Naik, I.; Bhajantri, R. Drastic Reduction in the Band Gap – A Novel Material for Plastic Electronics. *Mater. Today Proc.* **2018**, *5*, 21523–21528, doi:10.1016/j.matpr.2018.06.564.

119. Naik, I.; Bhajantri, R.; Tandel, R. The Band Gap Tuned, LEP Doped Polymer Films for Plastic Electronic Devices. *AIP Conf. Proc.* **2019**, *2057*, 020031, doi:10.1063/1.5085602.
120. Khalifeh, S. *Polymers in Organic Electronics: Polymer Selection for Electronic, Mechatronic & Optoelectronic Systems*; Elsevier, 2020; ISBN 9781927885673.
121. Zhao, Y.; Li, J.; Dong, Y.; Song, J. Synthesis of Colloidal Halide Perovskite Quantum Dots/Nanocrystals: Progresses and Advances. *Isr. J. Chem.* **2019**, *59*, 649–660, doi:10.1002/ijch.201900009.
122. Leng, Y. *Materials Characterization: Introduction to Microscopic and Spectroscopic Methods*; John Wiley & Sons, 2013; ISBN 9783527317608.
123. Mourdikoudis, S.; Pallares, R.M.; Thanh, N.T.K. Characterization Techniques for Nanoparticles: Comparison and Complementarity upon Studying Nanoparticle Properties. *Nanoscale* **2018**, *10*, 12871–12934, doi:10.1039/c8nr02278j.
124. Kumar, C.S.S.R. *UV-VIS Spectroscopy and Photoluminescence for Characterization*; Springer, 2013; ISBN 9783642275944.
125. Lakowicz, J.R. *Principles of Fluorescence Spectroscopy*; Springer, 2011; ISBN 0387312781.
126. Connor, D.V.O. *Time-Correlated Single Photon Counting*; Academic press, 1984; ISBN 0125241402.
127. Thomas, S.; Thomas, R.; Zachariah, A.K.; Mishra, R.K. *Spectroscopic Methods for Nanomaterials Characterization*; Elsevier, 2017; Vol. 2; ISBN 9780323461467.
128. Kwok, D.Y.; Neumann, A.W. Contact Angle Measurement and Contact Angle Interpretation. *Adv. Colloid Interface Sci.* **1999**, *81*, 167–249, doi:10.1016/S0001-8686(98)00087-6.
129. Brett, C.M.A. Electrochemical Impedance Spectroscopy in the Characterisation and Application of Modified Electrodes for Electrochemical Sensors and Biosensors. *Molecules* **2022**, *27*, 1497, doi:10.3390/molecules27051497.

130. Lee, M.M. Efficient Hybrid Solar Cells Based on Meso-Superstructured Organometal Halide Perovskites. *Science* (80-. ). **2012**, 338, 643, doi:10.1126/science.1228604.
131. Stranks, A.S.D.; Eperon, G.E.; Grancini, G.; Menelaou, C.; Alcocer, M.; Leijtens, T.; Herz, L.M.; Petrozza, A.; Henry, J. Electron-Hole Diffusion Lengths Exceeding Micron in an Organometal Trihalide Perovskite Absorber. *Science* (80-. ). **2013**, 342, 341–344.
132. Min, H.; Kim, M.; Lee, S.U.; Kim, H.; Kim, G.; Choi, K.; Lee, J.H.; Seok, S. II Efficient, Stable Solar Cells by Using Inherent Bandgap of a-Phase Formamidinium Lead Iodide. *Science* (80-. ). **2019**, 366, 749–753, doi:10.1126/science.aay7044.
133. Zhou, Y.; Herz, L.M.; Jen, A.K.Y.; Saliba, M. Advances and Challenges in Understanding the Microscopic Structure–Property–Performance Relationship in Perovskite Solar Cells. *Nat. Energy* **2022**, 7, 794–807, doi:10.1038/s41560-022-01096-5.
134. Mączka, M.; Ptak, M.; Gağor, A.; Stefańska, D.; Zaręba, J.K.; Sieradzki, A. Methylhydrazinium Lead Bromide: Noncentrosymmetric Three-Dimensional Perovskite with Exceptionally Large Framework Distortion and Green Photoluminescence. *Chem. Mater.* **2020**, 32, 1667–1673, doi:10.1021/acs.chemmater.9b05273.
135. Stefańska, D.; Ptak, M.; Mączka, M. Synthesis, Photoluminescence and Vibrational Properties of Aziridinium Lead Halide Perovskites. *Molecules* **2022**, 27, 7949, doi:10.3390/molecules27227949.
136. Brivio, F.; Walker, A.B.; Walsh, A. Structural and Electronic Properties of Hybrid Perovskites for High-Efficiency Thin-Film Photovoltaics from First-Principles. *APL Mater.* **2013**, 1, 042111, doi:10.1063/1.4824147.
137. Stoumpos, C.C.; Malliakas, C.D.; Kanatzidis, M.G. Semiconducting Tin and Lead Iodide Perovskites with Organic Cations: Phase Transitions, High Mobilities, and Near-Infrared Photoluminescent Properties. *Inorg. Chem.* **2013**, 52, 9019–9038, doi:10.1021/ic401215x.
138. Haug, F.; Yum, J.; Ballif, C. Organometallic Halide Perovskites: Sharp Optical Absorption Edge and Its Relation to Photovoltaic Performance. *J. Phys. Chem. Lett.* **2014**, 5, 1035–1039.

139. Manser, J.S.; Christians, J.A.; Kamat, P. V. Intriguing Optoelectronic Properties of Metal Halide Perovskites. *Chem. Rev.* **2016**, *116*, 12956–13008, doi:10.1021/acs.chemrev.6b00136.
140. Herz, L.M. Charge-Carrier Mobilities in Metal Halide Perovskites: Fundamental Mechanisms and Limits. *ACS Energy Lett.* **2017**, *2*, 1539–1548, doi:10.1021/acsenergylett.7b00276.
141. Huang, J.; Yuan, Y.; Shao, Y.; Yan, Y. Understanding the Physical Properties of Hybrid Perovskites for Photovoltaic Applications. *Nat. Rev. Mater.* **2017**, *2*, 17042, doi:10.1038/natrevmats.2017.42.
142. Zhao, B.; Bai, S.; Kim, V.; Lamboll, R.; Shivanna, R.; Auras, F.; Richter, J.M.; Yang, L.; Dai, L.; Alsari, M.; et al. High-Efficiency Perovskite–Polymer Bulk Heterostructure Light-Emitting Diodes. *Nat. Photonics* **2018**, *12*, 783–789, doi:10.1038/s41566-018-0283-4.
143. Mathews, I.; Sofia, S.; Ma, E.; Jean, J.; Laine, H.S.; Siah, S.C.; Buonassisi, T.; Peters, I.M. Economically Sustainable Growth of Perovskite Photovoltaics Manufacturing. *Joule* **2020**, *4*, 822–839, doi:10.1016/j.joule.2020.01.006.
144. Sun, C.; Jiang, Y.; Cui, M.; Qiao, L.; Wei, J.; Huang, Y.; Zhang, L.; He, T.; Li, S.; Hsu, H.; et al. High-Performance Large-Area Quasi-2D Perovskite Light-Emitting Diodes. *Nat. Commun.* **2021**, *12*, 2207, doi:10.1038/s41467-021-22529-x.
145. Park, J.; Kim, J.; Yun, H.S.; Paik, M.J.; Noh, E.; Mun, H.J.; Kim, M.G.; Shin, T.J.; Seok, S. II Controlled Growth of Perovskite Layers with Volatile Alkylammonium Chlorides. *Nature* **2023**, *616*, 724–730, doi:10.1038/s41586-023-05825-y.
146. Zhang, C.; Kuang, D. Bin; Wu, W.Q. A Review of Diverse Halide Perovskite Morphologies for Efficient Optoelectronic Applications. *Small Methods* **2020**, *4*, 1900662, doi:10.1002/smt.201900662.
147. Pan, L.; Pandey, I.R.; Miceli, A.; Klepov, V. V.; Chung, D.Y.; Kanatzidis, M.G. Perovskite CsPbBr<sub>3</sub> Single-Crystal Detector Operating at 1010 Photons S<sup>-1</sup> Mm<sup>-2</sup> for Ultra-High Flux X-Ray Detection. *Adv. Opt. Mater.* **2023**, *11*, 2202946, doi:10.1002/adom.202202946.

148. Jeong, B.; Veith, L.; Smolders, T.J.A.M.; Wolf, M.J.; Asadi, K. Room-Temperature Halide Perovskite Field-Effect Transistors by Ion Transport Mitigation. *Adv. Mater.* **2021**, *33*, 2100486, doi:10.1002/adma.202100486.
149. Zhang, Q.; Shang, Q.; Su, R.; Do, T.T.H.; Xiong, Q. Halide Perovskite Semiconductor Lasers: Materials, Cavity Design, and Low Threshold. *Nano Lett.* **2021**, *21*, 1903–1914, doi:10.1021/acs.nanolett.0c03593.
150. Zhao, L.; Zhou, Y.; Shi, Z.; Ni, Z.; Wang, M.; Liu, Y.; Huang, J. High-Yield Growth of FACsPbBr<sub>3</sub> Single Crystals with Low Defect Density from Mixed Solvents for Gamma-Ray Spectroscopy. *Nat. Photonics* **2023**, *17*, 315–323, doi:10.1038/s41566-023-01154-8.
151. Spanopoulos, I.; Lin, W.; Chung, D.Y.; Wessels, B.W.; He, Z. CsPbBr<sub>3</sub> Perovskite Detectors with 1.4% Energy Resolution for High Energy  $\gamma$ -Rays. *Nat. Photonics* **2021**, *15*, 36–42.
152. Zhang, X.; Peng, H.; Liu, J.; Yuan, Y. Highly Sensitive Plasmonic Biosensor Enhanced by Perovskite-Graphene Hybrid Configuration. *J. Opt.* **2023**, *25*, 075002, doi:10.1088/2040-8986/acd463.
153. Huang, H.; Pradhan, B.; Hofkens, J.; Roeffaers, M.B.J.; Steele, J.A. Solar-Driven Metal Halide Perovskite Photocatalysis: Design, Stability, and Performance. *ACS Energy Lett.* **2020**, *5*, 1107–1123, doi:10.1021/acsenergylett.0c00058.
154. Zhang, D.; Li, D.; Hu, Y.; Mei, A.; Han, H. Degradation Pathways in Perovskite Solar Cells and How to Meet International Standards. *Commun. Mater.* **2022**, *3*, 58, doi:10.1038/s43246-022-00281-z.
155. Kulbak, M.; Gupta, S.; Kedem, N.; Levine, I.; Bendikov, T.; Hodes, G.; Cahen, D. Cesium Enhances Long-Term Stability of Lead Bromide Perovskite-Based Solar Cells. *J. Phys. Chem. Lett.* **2016**, *7*, 167–172, doi:10.1021/acs.jpcllett.5b02597.
156. Møller, C.K. Crystal Structure and Photoconductivity of Caesium Plumbahalides. *Nature* **1958**, *182*, 1436.
157. Ten Brinck, S.; Infante, I. Surface Termination, Morphology, and Bright Photoluminescence of Cesium Lead Halide Perovskite Nanocrystals. *ACS Energy Lett.* **2016**, *1*, 1266–1272, doi:10.1021/acsenergylett.6b00595.

158. Rakitaa, Y.; Nir, K.; Satyajit, G.; Sadhanalab, A.; Vyacheslav, Kalchenkoc Marcus L., B.; Kulbaka, M.; Richard H., F.; David, C.; Gary, H. Low-Temperature Solution-Grown CsPbBr<sub>3</sub> Single Crystals and Their Characterization. *Cryst. Growth Des.* **2016**, *16*, 5715–5725.
159. Fang, F.; Chen, W.; Li, Y.; Liu, H.; Mei, M.; Zhang, R.; Hao, J.; Mikita, M.; Cao, W.; Pan, R.; et al. Employing Polar Solvent Controlled Ionization in Precursors for Synthesis of High-Quality Inorganic Perovskite Nanocrystals at Room Temperature. *Adv. Funct. Mater.* **2018**, *28*, 1706000, doi:10.1002/adfm.201706000.
160. Tenailleau, C.; Aharon, S.; Cohen, B. El; Etgar, L. Cell Refinement of CsPbBr<sub>3</sub> Perovskite Nanoparticles and Thin Films. *Nanoscale Adv.* **2019**, *1*, 147–153, doi:10.1039/c8na00122g.
161. Grisorio, R.; Fanizza, E.; Allegretta, I.; Altamura, D.; Striccoli, M.; Terzano, R.; Giannini, C.; Vergaro, V.; Ciccarella, G.; Margiotta, N.; et al. Insights into the Role of the Lead/Surfactant Ratio in the Formation and Passivation of Cesium Lead Bromide Perovskite Nanocrystals. *Nanoscale* **2020**, *12*, 623–637, doi:10.1039/c9nr08079a.
162. Xu, F.; Zhang, M.; Li, Z.; Yang, X.; Zhu, R. Challenges and Perspectives toward Future Wide-Bandgap Mixed-Halide Perovskite Photovoltaics. *Adv. Energy Mater.* **2023**, *13*, 2203911, doi:10.1002/aenm.202203911.
163. Yan, F.; Demir, H.V. LEDs Using Halide Perovskite Nanocrystal Emitters. *Nanoscale* **2019**, *11*, 11402–11412, doi:10.1039/c9nr03533h.
164. Zhu, X.; Ge, L.; Wang, Y.; Li, M.; Zhang, R.; Xu, M.; Zhao, Z.; Lv, W.; Chen, R. Recent Advances in Enhancing and Enriching the Optical Properties of Cl-Based CsPbX<sub>3</sub> Nanocrystals. *Adv. Opt. Mater.* **2021**, *9*, 2100058, doi:10.1002/adom.202100058.
165. Xiang, W.; Liu, S.; Tress, W. A Review on the Stability of Inorganic Metal Halide Perovskites: Challenges and Opportunities for Stable Solar Cells. *Energy Environ. Sci.* **2021**, *14*, 2090–2113, doi:10.1039/d1ee00157d.
166. Alaei, A.; Circelli, A.; Yuan, Y.; Yang, Y.; Lee, S.S. Polymorphism in Metal Halide Perovskites. *Mater. Adv.* **2021**, *2*, 47–63, doi:10.1039/d0ma00643b.

167. Calistru, D.M.; Mihut, L.; Lefrant, S.; Baltog, I. Identification of the Symmetry of Phonon Modes in CsPbCl<sub>3</sub> in Phase IV by Raman and Resonance-Raman Scattering. *J. Appl. Phys.* **1997**, *82*, 5391–5395, doi:10.1063/1.366307.
168. Trots, D.M.; Myagkota, S. V. High-Temperature Structural Evolution of Caesium and Rubidium Triiodoplumbates. *J. Phys. Chem. Solids* **2008**, *69*, 2520–2526, doi:10.1016/j.jpcs.2008.05.007.
169. Lai, M.; Kong, Q.; Bischak, C.G.; Yu, Y.; Dou, L.; Eaton, S.W.; Ginsberg, N.S.; Yang, P. Structural, Optical, and Electrical Properties of Phase-Controlled Cesium Lead Iodide Nanowires. *Nano Res.* **2017**, *10*, 1107–1114, doi:10.1007/s12274-016-1415-0.
170. Maqbool, M.; Rehman, G.; Ali, L.; Shafiq, M.; Iqbal, R.; Ahmad, R.; Khan, T.; Jalali-Asadabadi, S.; Maqbool, M.; Ahmad, I. Structural, Electronic and Optical Properties of CsPbX<sub>3</sub>(X=Cl, Br, I) for Energy Storage and Hybrid Solar Cell Applications. *J. Alloys Compd.* **2017**, *705*, 828–839, doi:10.1016/j.jallcom.2017.02.147.
171. He, Y.; Stoumpos, C.C.; Hadar, I.; Luo, Z.; McCall, K.M.; Liu, Z.; Chung, D.Y.; Wessels, B.W.; Kanatzidis, M.G. Demonstration of Energy-Resolved  $\gamma$ -Ray Detection at Room Temperature by the CsPbCl<sub>3</sub> Perovskite Semiconductor. *J. Am. Chem. Soc.* **2021**, *143*, 2068–2077, doi:10.1021/jacs.0c12254.
172. Eperon, G.E.; Paternò, G.M.; Sutton, R.J.; Zampetti, A.; Haghghirad, A.A.; Cacialli, F.; Snaith, H.J. Inorganic Caesium Lead Iodide Perovskite Solar Cells. *J. Mater. Chem. A* **2015**, *3*, 19688–19695, doi:10.1039/c5ta06398a.
173. Liao, M.; Shan, B.; Li, M. In Situ Raman Spectroscopic Studies of Thermal Stability of All-Inorganic Cesium Lead Halide. *J. Phys. Chem. Lett.* **2019**, *10*, 1217–1225.
174. Boote, B.W.; Andaraarachchi, H.P.; Rosales, B.A.; Blome-Fernández, R.; Zhu, F.; Reichert, M.D.; Santra, K.; Li, J.; Petrich, J.W.; Vela, J.; et al. Unveiling the Photo- and Thermal-Stability of Cesium Lead Halide Perovskite Nanocrystals. *ChemPhysChem* **2019**, *20*, 2647–2656, doi:10.1002/cphc.201900432.

175. Stoumpos, C.C.; Malliakas, C.D.; Peters, J.A.; Liu, Z.; Sebastian, M.; Im, J.; Chasapis, T.C.; Wibowo, A.C.; Chung, D.Y.; Freeman, A.J.; et al. Crystal Growth of the Perovskite Semiconductor CsPbBr<sub>3</sub>: A New Material for High-Energy Radiation Detection. *Cryst. Growth Des.* **2013**, *13*, 2722–2727, doi:10.1021/cg400645t.
176. Kobayashi, M.; Omata, K.; Sugimoto, S.; Tamagawa, Y.; Kuroiwa, T.; Asada, H.; Takeuchi, H.; Kondo, S. Scintillation Characteristics of CsPbCl<sub>3</sub> Single Crystals. *Nucl. Instruments Methods Phys. Res. Sect. A Accel. Spectrometers, Detect. Assoc. Equip.* **2008**, *592*, 369–373, doi:10.1016/j.nima.2008.04.079.
177. Li, X.; Wu, Y.; Zhang, S.; Cai, B.; Gu, Y.; Song, J.; Zeng, H. CsPbX<sub>3</sub> Quantum Dots for Lighting and Displays: Room Temperature Synthesis, Photoluminescence Superiorities, Underlying Origins and White Light-Emitting Diodes. *Adv. Funct. Mater.* **2016**, *26*, 2435–2445, doi:10.1002/adfm.201600109.
178. Zhang, Y.; Li, G.; She, C.; Liu, S.; Yue, F.; Jing, C.; Cheng, Y.; Chu, J. Room Temperature Preparation of Highly Stable Cesium Lead Halide Perovskite Nanocrystals by Ligand Modification for White Light-Emitting Diodes. *Nano Res.* **2021**, *14*, 2770–2775, doi:10.1007/s12274-021-3283-5.
179. Ghorai, A.; Mahato, S.; Srivastava, S.K.; Ray, S.K. Atomic Insights of Stable, Monodispersed CsPbI<sub>3</sub>–xBr<sub>x</sub> (x = 0, 1, 2, 3) Nanocrystals Synthesized by Modified Ligand Cell. *Adv. Funct. Mater.* **2022**, *32*, 2202087, doi:10.1002/adfm.202202087.
180. Mer, V.K. La Nucleation in Phase Transitions. *Ind. Eng. Chem.* **1952**, *44*, 1270–1277, doi:10.1021/ie50510a027.
181. Jung, M.; Ji, S.G.; Kim, G.; Seok, S. II Perovskite Precursor Solution Chemistry: From Fundamentals to Photovoltaic Applications. *Chem. Soc. Rev.* **2019**, *48*, 2011–2038, doi:10.1039/c8cs00656c.
182. Jeon, N.J.; Noh, J.H.; Kim, Y.C.; Yang, W.S.; Ryu, S.; Seok, S. II Solvent Engineering for High-Performance Inorganic-Organic Hybrid Perovskite Solar Cells. *Nat. Mater.* **2014**, *13*, 897–903, doi:10.1038/nmat4014.

183. Xiao, M.; Huang, F.; Huang, W.; Dkhissi, Y.; Zhu, Y.; Etheridge, J.; Gray-Weale, A.; Bach, U.; Cheng, Y.B.; Spiccia, L. A Fast Deposition-Crystallization Procedure for Highly Efficient Lead Iodide Perovskite Thin-Film Solar Cells. *Angew. Chemie - Int. Ed.* **2014**, *53*, 9898–9903, doi:10.1002/anie.201405334.
184. Rodová, M.; Brožek, J.; Knížek, K.; Nitsch, K. Phase Transitions in Ternary Caesium Lead Bromide. *J. Therm. Anal. Calorim.* **2003**, *71*, 667–673.
185. Malyshkin, D.; Sereda, V.; Ivanov, I.; Mazurin, M.; Sednev-Lugovets, A.; Tsvetkov, D.; Zuev, A. New Phase Transition in CsPbBr<sub>3</sub>. *Mater. Lett.* **2020**, *278*, doi:10.1016/j.matlet.2020.128458.
186. Nikou, T.; Witt, M.; Stathopoulos, P.; Barsch, A.; Halabalaki, M. Olive Oil Quality and Authenticity Assessment Aspects Employing FIA-MRMS and LC-Orbitrap MS Metabolomic Approaches. *Front. Public Heal.* **2020**, *8*, 558226, doi:10.3389/fpubh.2020.558226.
187. Noh, J.H.; Im, S.H.; Heo, J.H.; Mandal, T.N.; Seok, S. II Chemical Management for Colorful, Efficient, and Stable Inorganic-Organic Hybrid Nanostructured Solar Cells. *Nano Lett.* **2013**, *13*, 1764–1769, doi:10.1021/nl400349b.
188. Jeon, N.J.; Noh, J.H.; Yang, W.S.; Kim, Y.C.; Ryu, S.; Seo, J.; Seok, S. II Compositional Engineering of Perovskite Materials for High-Performance Solar Cells. *Nature* **2015**, *517*, 476–480, doi:10.1038/nature14133.
189. Jang, Y.W.; Lee, S.; Yeom, K.M.; Jeong, K.; Choi, K.; Choi, M.; Noh, J.H. Intact 2D/3D Halide Junction Perovskite Solar Cells via Solid-Phase in-Plane Growth. *Nat. Energy* **2021**, *6*, 63–71, doi:10.1038/s41560-020-00749-7.
190. Zhou, Y.Q.; Xu, J.; Liu, J.B.; Liu, B.X. Alloy Engineering in Mixed Sn-Ge Perovskites for Photovoltaic Application. *J. Mater. Chem. A* **2021**, *9*, 6955–6961, doi:10.1039/d0ta11107d.
191. Gutmann, V. Solvent Effects on the Reactivities of Organometallic Compounds. *Coord. Chem. Rev.* **1976**, *18*, 225–255, doi:10.1016/S0010-8545(00)82045-7.

192. Belmares, M.; Blanco, M.; Goddard, W.A.; Ross, R.B.; Caldwell, G.; Chou, S.H.; Pham, J.; Olofson, P.M.; Thomas, C. Hildebrand and Hansen Solubility Parameters from Molecular Dynamics with Applications to Electronic Nose Polymer Sensors. *J. Comput. Chem.* **2004**, *25*, 1814–1826, doi:10.1002/jcc.20098.
193. Yan, K.; Long, M.; Zhang, T.; Wei, Z.; Chen, H.; Yang, S.; Xu, J. Hybrid Halide Perovskite Solar Cell Precursors: Colloidal Chemistry and Coordination Engineering behind Device Processing for High Efficiency. *J. Am. Chem. Soc.* **2015**, *137*, 4460–4468, doi:10.1021/jacs.5b00321.
194. Petrov, A.A.; Ordinartsev, A.A.; Fateev, S.A.; Goodilin, E.A.; Tarasov, A.B. Solubility of Hybrid Halide Perovskites in Dmf and Dmso. *Molecules* **2021**, *26*, 7541, doi:10.3390/molecules26247541.
195. Huangfu, C.; Feng, L. High-Performance Fluorescent Sensor Based on CsPbBr<sub>3</sub> Quantum Dots for Rapid Analysis of Total Polar Materials in Edible Oils. *Sensors Actuators, B Chem.* **2021**, *344*, 130193, doi:10.1016/j.snb.2021.130193.
196. Chen, H.; Wang, Y.; Wang, J.; Liu, W. Thermal Stability of CsPbBr<sub>3</sub> Perovskite Quantum Dots Assembled with SBA-15. *Coatings* **2021**, *11*, 953, doi:https://doi.org/10.3390/coatings11080953.
197. Mott, S.N. The Mobility Edge since 1967. *J. Phys. C Solid State Phys.* **1987**, *20*, 3075–3102, doi:10.1142/9789812794086\_0042.
198. Smith, B.C. *Infrared Spectral Interpretation: A Systematic Approach*; CRC Press, 1999; ISBN 0849324637.
199. Akhil, S.; Dutt, V.G.V.; Mishra, N. Surface Modification for Improving the Photoredox Activity of CsPbBr<sub>3</sub> Nanocrystals. *Nanoscale Adv.* **2021**, *3*, 2547–2553, doi:10.1039/d1na00091h.
200. Heeger, A.J. Semiconducting and Metallic Polymers. *J. Phys. Chem.* **2001**, *105*, 8476, doi:10.1177/074193258901000304.
201. Chiang, C.K.; Fincher, C.B.; Jr., Y.W.P.; Heeger, A.J. Electrical Conductivity in Doped Polyacetylene. *Phys. Rev. Lett.* **1977**, *39*, 1098, doi:10.1103/PhysRevB.24.7380.

202. Forrest, S.R. *Organic Electronics: Foundations to Applications*; Oxford University Press, 2020; ISBN 9780198529729.
203. OLABISI, O.; ROBESON M., L.; SHAW, M.T. Polymer-Polymer Miscibility. *Acad. Press New York, USA* **1979**, *58*, 1553–1560, doi:10.1351/pac198658121553.
204. Aleshin, A.N.; Shcherbakov, I.P.; Gushchina, E. V.; Matyushkin, L.B.; Moshnikov, V.A. Solution-Processed Field-Effect Transistors Based on Polyfluorene –Cesium Lead Halide Nanocrystals Composite Films with Small Hysteresis of Output and Transfer Characteristics. *Org. Electron.* **2017**, *50*, 213–219, doi:10.1016/j.orgel.2017.08.004.
205. Aleshin, A.N.; Shcherbakov, I.P.; Chikalova-Luzina, O.P.; Matyushkin, L.B.; Ovezov, M.K.; Ershova, A.M.; Trapeznikova, I.N.; Petrov, V.N. Photo- and Electroluminescence Features of Films and Field Effect Transistors Based on Inorganic Perovskite Nanocrystals Embedded in a Polymer Matrix. *Synth. Met.* **2020**, *260*, 116291, doi:10.1016/j.synthmet.2020.116291.
206. Balena, A.; Cretí, A.; Lomascolo, M.; Anni, M. Investigation of the Exciton Relaxation Processes in Poly(9,9-Dioctylfluorene-Co -Benzothiadiazole):CsPbI<sub>1.5</sub>Br<sub>1.5</sub>nanocrystal Hybrid Polymer-Perovskite Nanocrystal Blend. *RSC Adv.* **2021**, *11*, 33531–33539, doi:10.1039/d1ra06821k.
207. Wu, R.; Wang, X.; Luo, J.; Liu, X.; Guo, F.; Li, B.; Wang, S.; Han, P.; Miao, X. Photon-Energy-Dependent Reversible Charge Transfer Dynamics of Double Perovskite Nanocrystal-Polymer Nanocomposites. *Nanomaterials* **2022**, *12*, 4300, doi:10.3390/nano12234300.
208. Al-Asbahi, B.A.; AlSalhi, M.S.; Jumali, A.F.M.H.H.; Qaid, S.M.H.; Mujamammi, W.M.; Ghaithan, H.M. Controlling the Emission Spectrum of Binary Emitting Polymer Hybrids by a Systematic Doping Strategy via Förster Resonance Energy Transfer for White Emission. *Micromachines* **2021**, *12*, 1371, doi:https://doi.org/ 10.3390/mi12111371.
209. Al-bati, S.; Hafizuddin, M.; Jumali, H.; Al-asbahi, B.A.; Khatatbeh, I.; Chi Chin, Y.; Qaid, S.M.H.; Hamid M., G.; Farooq, W.A. Improving Photophysical Properties of White Emitting Ternary Conjugated Polymer Blend Thin via Additions of TiO<sub>2</sub> Nanoparticles. *Polymers (Basel)*. **2020**, *12*, 2154, doi:doi:10.3390/polym12092154.

210. Thompson, B.C.; Fréchet, J.M.J. Polymer-Fullerene Composite Solar Cells. *Angew. Chemie - Int. Ed.* **2008**, *47*, 58–77, doi:10.1002/anie.200702506.
211. Li, F.; Wei, J.; Liao, G.; Guo, C.; Huang, Y.; Zhang, Q.; Jin, X.; Jiang, S.; Tang, Q.; Li, Q. Quaternary Quantum Dots with Gradient Valence Band for All-Inorganic Perovskite Solar Cells. *J. Colloid Interface Sci.* **2019**, *549*, 33–41, doi:10.1016/j.jcis.2019.04.052.
212. Flory, P.J. Thermodynamics of High Polymer Solutions. *J. Chem. Phys.* **1942**, *10*, 51–61, doi:10.1063/1.1723621.
213. Flory, P.J. *Principles of Polymer Chemistry*; Cornell University Press, 1953;
214. Kim, J.Y. Order-Disorder Phase Equilibria of Regioregular Poly(3-Hexylthiophene-2,5-Diyl)Solution. *Macromolecules* **2018**, *51*, 9026–9034, doi:10.1021/acs.macromol.8b01498.
215. Kim, J.Y. Phase Diagrams of Binary Low Bandgap Conjugated Polymer Solutions and Blends. *Macromolecules* **2019**, *52*, 4317–4328, doi:10.1021/acs.macromol.9b00477.
216. Kim, J.Y. Phase Diagrams of Ternary  $\pi$ -Conjugated Polymer Solutions for Organic Photovoltaics. *Polymers (Basel)*. **2021**, *13*, 983, doi:10.3390/polym13060983.
217. Van Krevelen, D.W. *Properties of Polymers: Their Correlation with Chemical Structure; Their Numerical Estimation and Prediction from Additive Group Contributions: Fourth Edition*; Elsevier, 2009; ISBN 9780080548197.
218. Kim, J.Y. Phase Behavior of Binary and Ternary Fluoropolymer (PVDF-HFP) Solutions for Single-Ion Conductors. *RSC Adv.* **2022**, *12*, 21160–21171, doi:10.1039/d2ra04158h.
219. Welyab, G.; Abebe, M.; Mani, D.; Thankappan, A.; Thomas, S.; Aga, F.G.; Kim, J.Y. All-Inorganic CsPbBr<sub>3</sub> Perovskite Nanocrystals Synthesized with Olive Oil and Oleylamine at Room Temperature. *micromachines* **2023**, *14*, 1332.
220. Idosa, D.A.; Abebe, M.; Mani, D.; Thankappan, A.; Thomas, S.; Aga, F.G.; Kim, J.Y. A Blue-Light-Emitting 3 Nm-Sized CsPbBr<sub>3</sub> Perovskite Quantum Dot with ZnBr<sub>2</sub> Synthesized by Room-Temperature Supersaturated Recrystallization. *In photonics* **2023**, *10*, 802.
221. Li, D.; Neumann, A.W. A Reformulation of the Equation of State for Interfacial Tensions. *J. Colloid Interface Sci.* **1990**, *137*, 304–307, doi:10.1016/0021-9797(90)90067-X.

222. Nilsson, S.; Bernasik, A.; Budkowski, A.; Moons, E. Morphology and Phase Segregation of Spin-Casted Films of Polyfluorene/PCBM Blends. *Macromolecules* **2007**, *40*, 8291–8301, doi:10.1021/ma070712a.
223. Jadhav, N. V.; Prasad, A.I.; Kumar, A.; Mishra, R.; Dhara, S.; Babu, K.R.; Prajapat, C.L.; Misra, N.L.; Ningthoujam, R.S.; Pandey, B.N.; et al. Synthesis of Oleic Acid Functionalized Fe<sub>3</sub>O<sub>4</sub> Magnetic Nanoparticles and Studying Their Interaction with Tumor Cells for Potential Hyperthermia Applications. *Colloids Surfaces B Biointerfaces* **2013**, *108*, 158–168, doi:10.1016/j.colsurfb.2013.02.035.
224. Lan, F.; Bai, J.; Wang, H. The Preparation of Oleylamine Modified Micro-Size Sphere Silver Particles and Its Application in Crystalline Silicon Solar Cells. *RSC Adv.* **2018**, *8*, 16866–16872, doi:10.1039/c8ra02620c.
225. Abdelaziz, B. Ben; Mustapha, N.; Bedja, I.M.; Aldaghri, O.; Idriss, H.; Ibrahem, M.; Ibnaouf, K.H. Spectral Behavior of a Conjugated Polymer MDMO-PPV Doped with ZnO Nanoparticles: Thin Films. *Nanomaterials* **2023**, *13*, 2405, doi:10.3390/nano13172405.
226. Li, Y.; Ma, F.; Zhao, D.; Lu, F.; Wang, J.; Cao, S.; Qian, J. Convenient Synthesis of High-Quality , All-Inorganic Lead Halide Perovskite Nanocrystals for High Purity Monochrome QLED. *Mater. Technol.* **2020**, *36*, 637–646, doi:10.1080/10667857.2020.1786782.
227. Peng, J.; Xia, C.Q.; Xu, Y.; Li, R.; Cui, L.; Clegg, J.K.; Herz, L.M.; Johnston, M.B.; Lin, Q. Crystallization of CsPbBr<sub>3</sub> Single Crystals in Water for X-Ray Detection. *Nat. Commun.* **2021**, *12*, 1531, doi:10.1038/s41467-021-21805-0.
228. Gidey, A.T.; Assayehegn, E.; Kim, J.Y. Hydrophilic Surface-Driven Crystalline Grain Growth of Perovskites on Metal Oxides. *ACS Appl. Energy Mater.* **2021**, *4*, 6923–6932, doi:10.1021/acsaem.1c01020.
229. Madhugiri, S.; Dalton, A.; Gutierrez, J.; Ferraris, J.P.; Balkus, K.J. Electrospun MEH-PPV/SBA-15 Composite Nanofibers Using a Dual Syringe Method. *J. Am. Chem. Soc.* **2003**, *125*, 14531–14538, doi:10.1021/ja030326i.

230. Salem, A.M.S.; Harraz, F.A.; El-Sheikh, S.M.; Hafez, H.S.; Ibrahima, I.A.; Mottaleb, and M.S.A.A. Enhanced Electrical and Luminescent Performance of Porous Silicon/MEH-PPV Nanohybrid Synthesized by Anodization and Repeated Spin Coating. *RSC Adv.* **2013**, *5*, 99892–99898, doi:10.1039/x0xx00000x.
231. Yan, D.; Shi, T.; Zang, Z.; Zhou, T.; Liu, Z.; Zhang, Z.; Du, J.; Leng, Y.; Tang, X. Ultrastable CsPbBr<sub>3</sub> Perovskite Quantum Dot and Their Enhanced Amplified Spontaneous Emission by Surface Ligand Modification. *Small* **2019**, *15*, 1901173, doi:10.1002/sml.201901173.
232. Kebede, T.; Abebe, M.; Mani, D.; Paduvilan, J.K.; Thottathi, L.; Thankappan, A.; Thomas, S.; Kamangar, S.; Shaik, A.S.; Badruddin, I.A.; et al. Phase Behavior and Role of Organic Additives for Self-Doped CsPbI<sub>3</sub> Perovskite Semiconductor Thin Films. *Micromachines* **2023**, *14*, 1601, doi:10.3390/mi14081601.
233. Schneckenburger, H. Förster Resonance Energy Transfer-What Can We Learn and How Can We Use It? *Methods Appl. Fluoresc.* **2020**, *8*, 013001, doi:10.1088/2050-6120/ab56e1.
234. Förster, T. Zwischenmolekulare Energiewanderung Und Fluoreszenz. *Ann. Phys.* **1948**, *437*, 55–75, doi:10.1002/andp.19484370105.
235. Zhang, Z.; Saparov, B. Charge Carrier Mobility of Halide Perovskite Single Crystals for Ionizing Radiation Detection. *Appl. Phys. Lett.* **2021**, *119*, 030502, doi:10.1063/5.0057411.
236. Shcherbakov-Wu, W.; Sercel, P.C.; Krieg, F.; Kovalenko, M. V.; Tisdale, W.A. Temperature-Independent Dielectric Constant in CsPbBr<sub>3</sub> Nanocrystals Revealed by Linear Absorption Spectroscopy. *J. Phys. Chem. Lett.* **2021**, *12*, 8088–8095, doi:10.1021/acs.jpcclett.1c01822.
237. Yao, E.P.; Bohn, B.J.; Tong, Y.; Huang, H.; Polavarapu, L.; Feldmann, J. Exciton Diffusion Lengths and Dissociation Rates in CsPbBr<sub>3</sub> Nanocrystal–Fullerene Composites: Layer-by-Layer versus Blend Structures. *Adv. Opt. Mater.* **2019**, *7*, 1801776, doi:10.1002/adom.201801776.
238. Cai, J.; Zhao, T.; Chen, M.; Su, J.; Shen, X.; Liu, Y.; Cao, D. Ion Migration in the All-Inorganic Perovskite CsPbBr<sub>3</sub> and Its Impacts on Photodetection. *J. Phys. Chem. C* **2022**, *126*, 10007–10013, doi:10.1021/acs.jpcc.2c03175.

239. Kim, J.Y.; Frisbie, C.D. Correlation of Phase Behavior and Charge Transport in Conjugated Polymer/Fullerene Blends. *J. Phys. Chem. C* **2008**, *112*, 17726–17736, doi:10.1021/jp8061493.
240. Cho, S.B.; Jung, J.W.; Kim, Y.S.; Cho, C.H.; Park, I.K. Emission Wavelength Control of CsPb(Br<sub>1-x</sub>Cl<sub>x</sub>)<sub>3</sub>nanocrystals for Blue Light-Emitting Diode Applications. *CrystEngComm* **2021**, *23*, 2746–2755, doi:10.1039/d1ce00132a.
241. Bi, C.; Wang, S.; Wen, W.; Yuan, J.; Cao, G.; Tian, J. Room-temperature Construction of Mixed-Halide Perovskite Quantum Dots with High Photoluminescence Quantum Yield. *J. Phys. Chem. C* **2018**, *122*, 5151–5160, doi:10.1021/acs.jpcc.7b12607.
242. Faridi, A.W.; Imran, M.; Tariq, G.H.; Ullah, S.; Noor, S.F.; Ansar, S.; Sher, F. Synthesis and Characterization of High-Efficiency Halide Perovskite Nanomaterials for Light-Absorbing Applications. *Ind. Eng. Chem. Res.* **2023**, *62*, 4494–4502, doi:10.1021/acs.iecr.2c00416.
243. Hu, Y.; Cao, S.; Qiu, P.; Yu, M. All – Inorganic Perovskite Quantum Dot – Based Blue Light – Emitting Diodes : Recent Advances and Strategies. *Nanomater.* **2022**, *12*, 4372. <https://doi.org/10.3390/nano12244372> **2022**.
244. Xu, L.; Yuan, S.; Zeng, H.; Song, J. A Comprehensive Review of Doping in Perovskite Nanocrystals/Quantum Dots: Evolution of Structure, Electronics, Optics, and Light-Emitting Diodes. *Mater. Today Nano* **2019**, *6*, 100036, doi:10.1016/j.mtnano.2019.100036.
245. Luo, M.; Jiang, Y.; He, T.; Yuan, M. Metal Halide Perovskites for Blue Light Emitting Materials. *APL Mater.* **2020**, *8*, 040907, doi:10.1063/1.5144101.
246. Pushkarev, A.P.; Korolev, V.I.; Anoshkin, S.S.; Komissarenko, F.E.; Makarov, S. V.; Zakhidov, A.A. Cesium Lead Mixed-Halide Perovskites in Polymer Matrix. *J. Phys. Conf. Ser.* **2018**, *1092*, 012122, doi:10.1088/1742-6596/1092/1/012122.
247. Din, U.K.N.; Salleh, M.M.; Aziz, T.H.T.; Umar, A.A. Composition Dependence of Photoluminescence Properties of Poly(9,9-Di-n-Hexylfluorenyl-2,7-Diyl) with Perovskite-Structured SrTiO<sub>3</sub> Nanocomposites. *Superlattices Microstruct.* **2016**, *93*, 153–156, doi:10.1016/j.spmi.2016.03.011.

248. Din, U.K.N.; Salleh, M.M.; Aziz, T.H.T.; Md Zain, A.R.; Mohamed, M.A.; Umar, A.A. On the Performance of Polymer-Inorganic Perovskite Oxide Composite Light-Emitting Diodes: The Effect of Perovskite SrTiO<sub>3</sub> Additives. *Nanomater. Nanotechnol.* **2021**, *11*, 1–9, doi:10.1177/1847980420987774.
249. Kirakosyan, A.; Kim, Y.; Sihn, M.R.; Jeon, M.G.; Jeong, J.R.; Choi, J. Solubility-Controlled Room-Temperature Synthesis of Cesium Lead Halide Perovskite Nanocrystals. *ChemNanoMat* **2020**, *6*, 1863–1869, doi:10.1002/cnma.202000471.
250. Economopoulos, S.P.; Govaris, G.K.; Chochos, C.L.; Tzanetos, N.P.; Andreopoulou, A.K.; Kallitsis, J.K.; Yianoulis, P.; Gregoriou, V.G. Synthesis and Characterization of Conjugated Polymers and Their Blends for Optoelectronic Applications. *Macromol. Symp.* **2004**, *205*, 19–31, doi:10.1002/masy.200450103.
251. Yu, H.; Wang, H.; Zhang, T.; Yi, C.; Zheng, G.; Yin, C.; Karlsson, M.; Qin, J.; Wang, J.; Liu, X.K.; et al. Color-Stable Blue Light-Emitting Diodes Enabled by Effective Passivation of Mixed Halide Perovskites. *J. Phys. Chem. Lett.* **2021**, *12*, 6041–6047, doi:10.1021/acs.jpcclett.1c01547.
252. Yandri, V.R.; Wulandari, P.; Hidayat, R. Photoluminescence Properties of CsPbCl<sub>3</sub> and CsPbBr<sub>3</sub> Nanocrystals Synthesized by LARP Method with Various Ligands and Anti-Solvents. *J. Phys. Conf. Ser.* **2022**, *2243*, 012120, doi:10.1088/1742-6596/2243/1/012120.
253. Sharaf, I.M.; Shurukhina, A. V.; Emeline, A. V. Structural and Optical Properties of Pristine and Doped CsPbBr<sub>3</sub> Perovskite Structural and Optical Properties of Pristine and Doped. *IOP Conf. Ser. Earth Environ. Sci.* **2021**, *706*, 012044, doi:10.1088/1755-1315/706/1/012044.
254. Madhavan, J.; Alsalhi, M.S. Mixed Perovskite ( MAPbI<sub>3-x</sub> Cl<sub>x</sub> ) Solar Cells Using Light-Emitting Conjugated Polymer DMP End-Capped MDMO-PPV as a Hole. *J. King Saud Univ. - Sci.* **2022**, 102262, doi:10.1016/j.jksus.2022.102262.
255. Al-Asbahi, B.A.; Alanezi, A.A.; Alsalhi, M.S. Photophysical Characteristics of Multicolor Emitting MDMO-PPV–DMP/ZnO Hybrid Nanocomposites. *Molecules* **2022**, *27*, 843, doi:10.3390/molecules27030843.

256. Kumar, S.A.; Shankar, J.S.; Periyasamy, B.K. Study on Interfacial Interactions and Optoelectronic Properties of MEH-PPV / SnO<sub>2</sub> Hetero-Structure. *IOP Conf. Ser. Earth Environ. Sci.* **2021**, *706*, 012044.
257. Shamim, S.; Abir, H.; Gupta, S.K.; Ibrahim, A.; Srivastava, B.B.; Lozano, K. Tunable CsPb(Br/Cl)<sub>3</sub> Perovskite Nanocrystals and Further Advancement in Designing Light Emitting Fiber Membranes. *Mater. Adv.* **2021**, 2700–2710, doi:10.1039/d1ma00183c.2021,2700-2710.
258. Yerezhap, D.; Omarova, Z.; Aldiyarov, A.; Shinbayeva, A.; Tokmoldin, N. IR Spectroscopic Degradation Study of Thin Organometal Halide Perovskite Films. *Mol.* **2023**, *28*, 1288, doi:10.3390/molecules28031288.
259. Gan, Z.; Yu, Z.; Meng, M.; Xia, W.; Zhang, X. Hydration of Mixed Halide Perovskites Investigated by Fourier Transform Infrared Spectroscopy Hydration of Mixed Halide Perovskites Investigated by Fourier Transform Infrared Spectroscopy. *APL Mater.* **2019**, *7*, 031107, doi:10.1063/1.5087914.

## Appendix

### Curriculum vitae

#### A. PERSONAL INFORMATION

Name: **Getachew Welyab Tsoni**

Sex: **Male** Date of Birth: **March 13, 1980 E.C**



Place of Birth: **Maji ( Gobi)**, South West Regional State, West Omo Zone

Nationality: **Ethiopian** Address: Mobile- **+251912867034** E-mail:- [gwelyabt@gmail.com](mailto:gwelyabt@gmail.com)

#### B. Current status

- ✚ Ph.D. Candidate, **Department of Materials science and engineering** at Jimma institute of technology, Jimma University, Jimma, Ethiopia.
- ✚ Project: **Conjugated Polymer-Perovskite Nanocomposites for Optoelectronics**

#### C. Education

- ✚ Undergraduate: B.Ed in mathematics (Major: **Mathematics** and Minor: **Physics**) from Mizan- Tepi University, July 17, 2010 G.C.
- ✚ Post graduate: **Msc in solid state Physics** from Dilla University June 3, 2016 G.C.

#### D. Work experiences

- Mathematics teacher at Maji Lewt fre secondary school (Aug .14,2003-June30 ,2004 E.C)
- Diizin language expert at Summer institute of linguist at Mizan-Teferi (Jul 1,2004-Oct 30,2006 E.C)
- Head of education office at Maji Werda (Nov1,2006-Feb 30,2006 E.C)
- Lecturer at Mizan-Tepi University (Sep 7,2016- Feb 9,2019 G.C )
- Head of physics department and lecture at Mizan-Tepi University(Feb 9,2019G.C-Sep 20,2019G.C)

#### E. Publications

1. Getachew Welyab ,Muluaem Abebe , Dhakshnamoorthy Mani , Aparna Thankappan , Sabu Thomas , Fekadu Gochole Aga and Jung Yong Kim .All-Inorganic CsPbBr<sub>3</sub> Perovskite Nanocrystals Synthesized with Olive Oil and Oleylamine at Room Temperature. *Micromachines*, **2023**.  
<https://doi.org/10.3390/mi14071332>.
2. Getachew Welyab , Muluaem Abebe , Dhakshnamoorthy Mani , Jibin Keloth Paduvilan, Lishin Thottathi, Aparna Thankappan, Sabu Thomas, Tadele Hunde Wondimu and Jung Yong Kim. Conjugated Polymer–Perovskite Quantum Dot (MDMO-PPV:CsPbBr<sub>3</sub>) Nanocomposites: Miscibility, Nano-Structures and Properties. *Next Nanotechnology* 5 (2024) 100053.  
<https://doi.org/10.1016/j.nxnano.2024.100053>.

#### F. List of Presentations

1. Room temperature synthesis of CsPbBr<sub>3</sub> Perovskite nanocrystals with olive oil and oleylamine. Oral presentation (**III. International architectural sciences and applications symposium**,Sep.14-15, 2023, Nepals–Italy in collaborations with University of Nepals Federico-II)
2. Facile synthesis and characterization of polymer/mixed halide perovskite composites. Oral presentation (**8<sup>th</sup> International Eduction and Innovative congress**, Nov 24-26, 2023, Ankara, Turkey)